Learning to Visually Predict Terrain Properties for Planetary Rovers

by

Christopher A. Brooks

Bachelor of Science in Engineering and Applied Science
California Institute of Technology, 2000

Master of Science in Mechanical Engineering
Massachusetts Institute of Technology, 2004

Submitted to the Department of Mechanical Engineering in Partial Fulfillment of the Requirements for the Degree of

Doctor of Philosophy in Mechanical Engineering

at the

Massachusetts Institute of Technology

June 2009

Signature of Author: _____
Department of Mechanical Engineering
May 7, 2009

Certified by: _____
Karl Iagnemma
Principal Research Scientist
Thesis Supervisor

Accepted by: _____
David Hardt
Professor of Mechanical Engineering
Graduate Officer, Department of Mechanical Engineering

Learning to Visually Predict Terrain Properties for Planetary Rovers

by

Christopher A. Brooks

Submitted to the Department of Mechanical Engineering
on May 7, 2009, in partial fulfillment of the requirements for the degree of
Doctor of Philosophy in Mechanical Engineering

Abstract

For future planetary exploration missions, improvements in autonomous rover mobility have the potential to increase scientific data return by providing safe access to geologically interesting sites that lie in rugged terrain, far from landing areas. This thesis presents an algorithmic framework designed to improve rover-based terrain sensing, a critical component of any autonomous mobility system operating in rough terrain. Specifically, this thesis addresses the problem of predicting the mechanical properties of distant terrain. A self-supervised learning framework is proposed that enables a robotic system to learn predictions of mechanical properties of distant terrain, based on measurements of mechanical properties of similar terrain that has been previously traversed.

The proposed framework relies on three distinct algorithms. A mechanical terrain characterization algorithm is proposed that computes upper and lower bounds on the net traction force available at a patch of terrain, via a constrained optimization framework. Both model-based and sensor-based constraints are employed. A terrain classification method is proposed that exploits features from proprioceptive sensor data, and employs either a supervised support vector machine (SVM) or unsupervised *k*-means classifier to assign class labels to terrain patches that the rover has traversed. A second terrain classification method is proposed that exploits features from exteroceptive sensor data (e.g. color and texture), and is automatically trained in a self-supervised manner, based on the outputs of the proprioceptive terrain classifier. The algorithm includes a method for distinguishing novel terrain from previously observed terrain. The outputs of these three algorithms are merged to yield a map of the surrounding terrain that is annotated with the expected achievable net traction force. Such a map would be useful for path planning purposes.

The algorithms proposed in this thesis have been experimentally validated in an outdoor, Mars-analog environment. The proprioceptive terrain classifier demonstrated 92% accuracy in labeling three distinct terrain classes. The exteroceptive terrain classifier that relies on self-supervised training was shown to be approximately as accurate as a similar, human-supervised classifier, with both achieving 94% correct classification rates on identical data sets. The algorithm for detection of novel terrain demonstrated 89% accuracy in detecting novel terrain in this same environment. In laboratory tests, the mechanical terrain characterization algorithm predicted the lower bound of the net available traction force with an average margin of 21% of the wheel load.

Thesis Supervisor: Karl Iagnemma
Principal Research Scientist

Acknowledgements

I would like to thank my adviser and the rest of my Ph.D. committee for their guidance and support of my research and this thesis. Their advice has greatly improved the quality of this work.

I would like to thank all of the people who helped me with my experiments with the TORTOISE rover. Maria Tanner, Matt Carvey, Shingo Shimoda, Ibrahim Halatci, and Marcos Berrios all contributed to the construction and assembly of the rover. I gratefully appreciate everyone who helped me in taking the rover to test sites around MIT and Gloucester, including Shingo Shimoda, Ibrahim Halatci, Chris Ward, Steve Peters, Sterling Anderson, Jon Brooks, and Artie Moffa. I hope you don't hold it against me that "a day at the beach" always seemed to coincide with frigid temperatures. Except one gorgeous day in January.

For the experiments with the FSRL Wheel-Terrain Testbed, I have Shinwoo Kang to thank.

I would also like to thank all of the other members of the Field and Space Robotics Laboratory for making all of my hours in the lab more enjoyable, and my family and friends who made my time outside the lab something to look forward to. Most especially, I would like to thank my wife, Corinne, for her unending support and encouragement.

This work was supported by the National Aeronautics and Space Administration through the Mars Technology Program, and by the US Army Research Office.

Table of Contents

List of Figures

List of Tables

Chapter 1

Introduction

1.1 Problem Statement and Motivation

The ability for humans to explore the surface of other planets using mobile robots ("rovers") is fundamentally dependent on the autonomous mobility capabilities of these robots. Because targets of scientific interest such as craters, ravines, and cliffs present dangers to landing, planetary rovers must land at safe locations and travel long distances to reach these targets (NASA/JPL, 2007). Close teleoperational supervision of robots is not desirable because limited communication with operators on Earth places significant restrictions on the distance a rover can travel during a mission lifetime—for each downlink/uplink cycle of roughly 24 hours (Mishkin & Laubach, 2006), the rover cannot safely travel beyond the distance it can image with its cameras, which has been as little as 15 meters or less in dune fields observed by the Mars Exploration Rovers (NASA/JPL, 2005). Thus, advances in robot autonomy will lead to payoffs in terms of scientific data return from locations that were previously unreachable, since it will allow rovers to travel longer distances with limited human supervision.

One current limitation to autonomous mobility is the rover's inability to autonomously identify terrain regions that can be safely traversed. Existing path planning

algorithms can generate a route to a target that avoids known obstacles only if they are given an accurate map of the ease of traversability of the surrounding terrain (Nilsson, 1982; Stentz, 1994; Goldberg, Maimone, & Matthies, 2002). Unknown hazards have the potential to immobilize the rover, delaying or permanently preventing completion of the mission. Thus, autonomous navigation is generally restricted to environments which operators have previously determined to be relatively benign. The ability to autonomously detect possible hazards from a safe distance would enable safe autonomous travel in previously unexplored rough terrain.

While geometric[1] hazards, such as large rocks or cliffs, can be sensed remotely using range sensing techniques (Talukder et al., 2002), little research has addressed remote sensing of non-geometric hazards, such as loosely packed soil or sandy slopes. The importance of sensing non-geometric hazards was highlighted in April 2005, when the Mars Exploration Rover (MER) Opportunity became entrenched in a dune composed of loosely packed drift material (Cowen, 2005). Figure 1-1 shows the deep tracks left in the dune after Opportunity extricated itself. The terrain geometry was not hazardous, as the rover could have easily traversed the dune if it were made of a material with more favorable terrain properties, such as rock or packed soil. On the contrary, it was the mechanical properties of the terrain surface which made it a hazard—the high compactability of the loose drift material caused the wheels to sink deeply into the surface, and the combination the drift's low internal friction and the motion resistance due to sinkage prevented the rover from producing sufficient thrust to travel up the slope.

[1] Here, geometric hazards are considered to be obstacles which prevent safe travel of a rover due primarily to their shape, and not to loss of traction between a wheel and the terrain. In contrast, non-geometric hazards are regions of terrain which are impassible due to their limited traction properties (or a combination of the limited traction and terrain geometry) which could lead to rover immobilization.

Opportunity's progress was delayed for more than a month while engineers worked to extricate it.

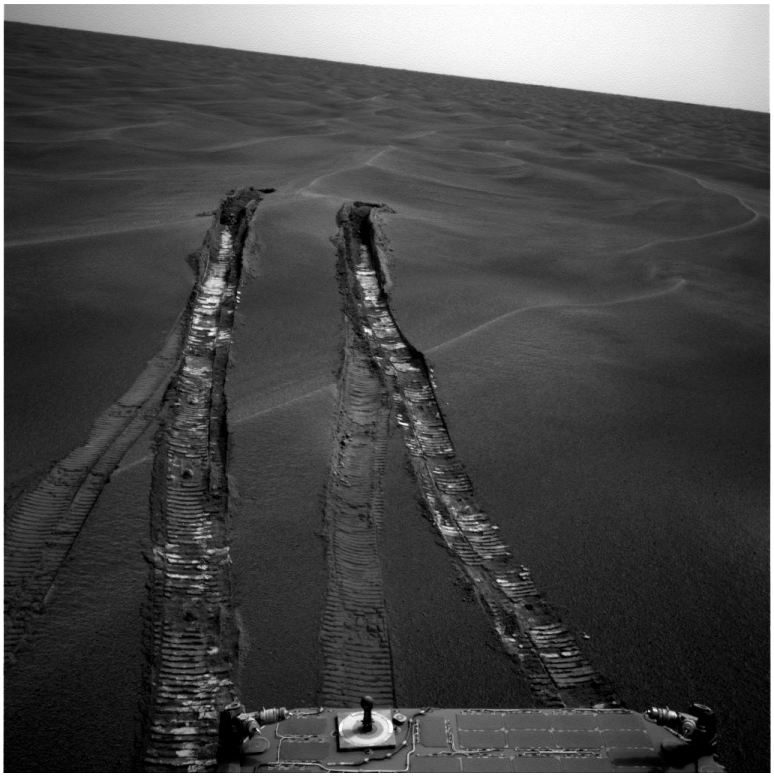

Figure 1-1. Deep tracks in Purgatory Dune left by MER Opportunity (Image courtesy NASA/JPL-Caltech)

Since non-geometric hazards are highly dependent on wheel-terrain interaction properties, methods for characterizing such hazards have focused on measuring aspects of that interaction. Examples include wheel sinkage measurement (Brooks, Iagnemma, & Dubowsky, 2006; Wilcox, 1994), parametric soil characterization (Iagnemma, Kang, Shibly, & Dubowsky, 2004), wheel slip detection (Reina, Ojeda, Milella, & Borenstein, 2006), and explicit traversability estimation (Kang, 2003). These methods rely on

proprioceptive[2] terrain sensing, which characterizes only the terrain immediately under the rover wheel, so it is of limited use for predictive hazard avoidance.

Where researchers have addressed terrain sensing using exteroceptive sensors, such as cameras or LIDAR sensors, it has typically been assumed that the visual appearances of terrain classes of interest are known a priori (Angelova, Matthies, Helmick, & Perona, 2007a; Wellington, Courville, & Stentz, 2005). Although (Kim, Sun, Oh, Rehg, & Bobick, 2006) describes an approach for distinguishing traversable from non-traversable terrain where the terrain class appearances are learned, their work focuses on the detection of geometric hazards. No research has addressed the detection of non-geometric hazards using exteroceptive sensors, where the visual appearance of the terrain classes is not known a priori.

In summary, autonomous planetary rover mobility is significantly affected by the mechanical properties of terrain, which to date have been identified only for terrain physically contacted by the rover or for terrain classes known a priori. In environments where the visual appearances of terrain classes are not known a priori, no framework exists for autonomously predicting the mechanical properties of distant terrain, such that these properties can be used for autonomous navigation and hazard avoidance. Such an approach would greatly increase a rover's ability to autonomously navigate to distant sites of scientific interest.

[2] Proprioceptive sensors measure the internal state of the rover, and therefore sense terrain through its interaction with the rover. In this work, wheel torque, wheel speed, and wheel sinkage are considered to be measured by proprioceptive sensors.

1.2 Purpose of this Thesis and Scenario Description

The purpose of this thesis is to develop a framework and the underlying algorithmic components to enable a planetary rover to accurately predict mechanical properties of distant terrain, by learning from its experience in traversing similar terrain. In particular, this work is concerned with 1) the estimation of mechanical properties relevant to robotic mobility prediction, and with 2) associating these mechanical properties with visual features, such that the mechanical properties can be reliably identified from a distance of several meters. To minimize the time between terrain sensing and terrain property prediction, emphasis will be placed on using algorithms that are computationally inexpensive, such that they can be executed in seconds or minutes on COTS hardware.

The scenario assumed for this work is one of planetary exploration, loosely modeled on the sensing, mobility, and predicted environment of the Mars Science Laboratory (MSL) mission, a large, six-wheeled rover scheduled for launch to Mars in 2011 (J. Johnson, 2008; NASA/JPL, 2008b). (Figure 1-2 shows an artist's concept of the MSL on Mars.) In this scenario, communication delays of 8 to 40 minutes (round-trip) and a communication bandwidth of approximately 7.5 MB per day necessitate the use of autonomous navigation to reach targets of interest at least 20 km away[3]. (For comparison, Opportunity and Spirit, which have been on Mars for nearly 5 years, are only now on the verge of having traveled 20 km combined (NASA/JPL, 2008a).) The challenge of terrain sensing is eased by the fact that the environment can be considered as static—any obstacles will remain stationary—and the robot is slow-moving, traveling at a speed of 5

[3] Twenty kilometers is the predicted length of the landing ellipse for MSL.

to 15 cm per second. However computation is limited,[4] and a very high cost of failure requires that any approach tend to minimize risk of failure.

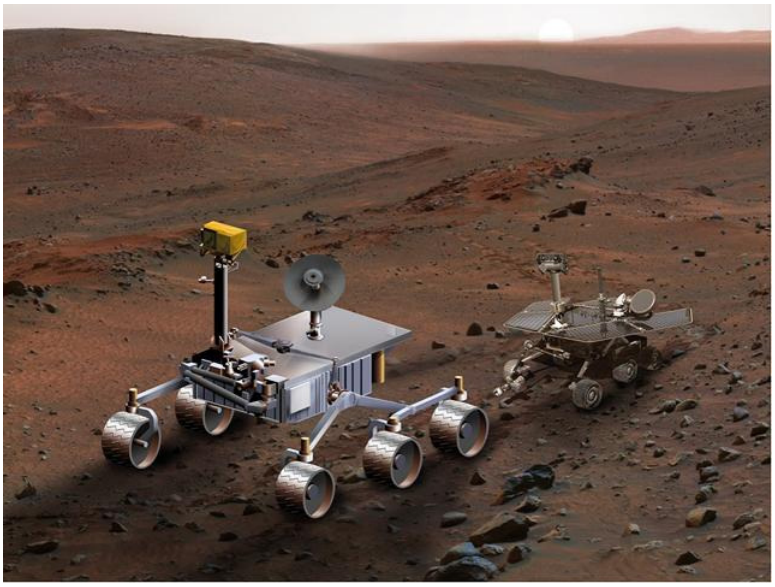

Figure 1-2. Artist concept of Mars Science Laboratory, left, compared to Mars Exploration Rover, right (Image courtesy NASA/JPL-Caltech)

In this thesis it is assumed that the rover will be able to measure wheel torque, sinkage of a rigid wheel into deformable terrain, and vibrations in the rover suspension arising from wheel-terrain interaction. Wheel torque can either be measured with a dedicated torque sensor, or estimated from motor current and wheel speed using a Kalman filter. Wheel sinkage can be measured visually based on images containing the rover wheels as in (Brooks et al., 2006), or the relative wheel sinkage between two positions on the rover path can be calculated as in (Wilcox, 1994). It should be noted that wheel torque and sinkage measurement can be implemented with no additional hardware beyond that planned for MSL. Rover suspension vibration can be sensed using an inexpensive contact microphone or accelerometer.

[4] MSL has a radiation-hardened version of IBM's PowerPC 750 running at 200 MHz (Bajracharya, Maimone, & Helmick, 2008). For reference, the PowerPC G3 line of Macintosh desktop computers based around the PowerPC 750 were sold between November, 1997 and July, 2001.

It is also assumed that the rover will be equipped with a stereo pair of mast-mounted cameras to sense the color and geometry of terrains from 1 meter to 20 meters away. This sensing is currently planned for inclusion on MSL as a pair of monochrome cameras with filter wheels. The last assumption is that the rover will be able to measure its speed relative to the terrain. This is currently implemented on the Mars Exploration Rovers via a visual odometry algorithm (Maimone, A. Johnson, Cheng, Willson, & Matthies, 2006).

1.3 Background and Literature Review

This thesis draws on techniques from the machine learning and machine vision fields, as well as research in terrain parameter estimation and mobility prediction. While most previous works in robotic terrain estimation have addressed only a subset of these research areas, some recent works have presented coherent approaches to mobility-related terrain sensing. These works will be described in the first subsection. Other subsections address previous work related to the algorithmic components of this thesis, including terrain recognition, machine learning, and mobility prediction.

1.3.1 Mobility-related Terrain Sensing

Terrain sensing is a broad field addressing the interpretation of sensor data to yield information about a terrain region. Here, mobility-related terrain sensing refers to approaches for associating sensor data with vehicle mobility. Some approaches operate on data from only proprioceptive sensors (e.g. vibration or wheel sinkage data), and thus address the rover's mobility on the terrain immediately beneath the rover's wheels. Other

approaches operate on data from exteroceptive sensors (e.g. vision or LIDAR data), and are used to predict the mobility properties of terrain several rover lengths away.

1.3.1.1 Binary Hazard Detection

Historically, mobility-related terrain sensing has focused on binary hazard detection (Bellutta, Manduchi, Matthies, Owens, & Rankin, 2000; Henriksen & Krotkov, 1997). In this paradigm, regions of terrain are deemed either traversable (i.e. non-hazards) or non-traversable (i.e. hazards), with no quantitative measure of traverse difficulty or uncertainty. Most research has assumed that these hazards are physical obstacles geometrically distinct from the surrounding terrain, and thus addresses the extraction of obstacles from a 2½-D or 3-D representation of the scene. A fully 3-D obstacle detection scheme is presented in (Talukder, Manduchi, Rankin, & Matthies, 2002). It relies on detecting abrupt changes in the terrain height. An extension to this work, presented in (Talukder et al., 2002), includes the visual appearance of terrain in the obstacle detection process, where the visual appearance is used to determine which of the geometrically detected obstacles are likely to be traversable despite their geometry (e.g. tall grass). It assigns a traversability metric in the form of a maximum safe driving speed, however this is based solely on analysis of 3-D geometry. Thus, the work does not address the detection of non-geometric obstacles, which is the primary focus of this thesis.

Other work in binary hazard detection relies on color and LIDAR data to estimate the geometry of a load-bearing surface in the presence of thick vegetation (Wellington et al., 2005). A hidden semi-Markov model is used as a framework to filter the sensor data and distinguish vegetation from solid ground. While this approach includes a component

of terrain sensing relevant to mobility, the surface type (i.e. vegetation or solid ground) is not used for traversability estimation. It therefore does not attempt to detect non-geometric hazards.

More recently, researchers have attempted to learn to distinguish traversable terrain from non-traversable terrain using a combination of color, visual texture, and geometry (Kim et al., 2006). Their approach is conceptually similar to the one presented in this thesis, in that the rover learns from its experiences. The rover initially plans a path assuming that all terrain is traversable, then learns to recognize the visual appearance of obstacles when it contacts terrain that impedes its motion. Their approach differs from the one presented in this thesis in that they assume a strict dichotomy between traversable and nontraversable terrain, as opposed to the gradations of traversability considered in this thesis. In addition, their approach is designed for an environment in which none of the terrain would be treacherous to attempt to traverse, because its only method for identifying non-traversable terrain is physical contact with an object impeding its motion. In contrast, the approach presented in this thesis could be used to predict robot mobility on impassable slopes composed of a given terrain, even if a rover's only experiences with the terrain were on marginally traversable flat ground. Also, as with (Talukder et al., 2002), the work focuses on identifying terrain which is likely to be traversable despite its geometry, such as tall grass.

1.3.1.2 Proprioceptive Terrain Sensing

Other work has addressed the issue of distinguishing non-geometric hazards using proprioceptive sensors. (Wilcox, 1994) describes a method for wheel sinkage detection using suspension configuration sensors. Another method measures wheel sinkage using

images from a camera with a view of the wheel, by detecting the intensity difference between the wheel and the terrain (Brooks et al., 2006). These approaches are useful for identifying when a rover is in danger of becoming entrenched, but they cannot be used to predict the traversability of distant terrain, since they can only be used to sense terrain immediately under the rover's wheels.

Since excessive wheel slip is the failure mode for non-geometric hazards, terrain sensing approaches that estimate wheel slip are also useful in the context of rover mobility. For this reason, several researchers have focused on using proprioceptive sensors to detect wheel slip (Ojeda & Borenstein, 2002; Ojeda, Cruz, Reina, & Borenstein, 2006; Reina et al., 2006; Ward & Iagnemma, 2007). Again, however, the reliance on proprioceptive sensor data prevents easy generalization to the prediction of properties of distant terrain.

1.3.1.3 Exteroceptive Traversability Sensing

To provide a useful prediction of the properties of terrain that lies more than one rover-length away, some researchers have used a learning framework similar to the one presented in this thesis. Researchers at JPL have attempted to model wheel slip as a function of visual and geometric terrain properties, where the wheel slip model is adapted on-line (Angelova et al., 2007a, 2007b; Angelova, Matthies, Helmick, Sibley, & Perona, 2006). They achieve good slip prediction results using an empirically generated slip model. However their approach assumes that the visual appearance of terrain classes is known a priori. Thus it would be inappropriate for use in an environment where the rover might encounter unexpected terrain.

Another group has implemented self-supervised learning for terrain sensing on a larger scale (Sofman et al., 2006). They attempt to generalize a LIDAR-based traversability metric, accurate at a range of tens of meters, to the kilometer-scale field of view of an aerial camera. They succeed in improving the look-ahead range for path planning, but their traversal cost values have no physical interpretation, so there is no obvious method to quantify the accuracy of their traversability map. Also, they assume that color from an overhead image directly maps to traversability without regard to topography. This is unlikely to hold in the planetary exploration setting, where changes in terrain slope may not be accompanied by changes in terrain color.

1.3.2 Terrain Classification

Terrain classification has received significant attention for the purposes of both robotic autonomy and remote science. Terrain classification based on satellite imagery has been commonly used by scientists for land use monitoring, e.g. (Berni, Zarco-Tejada, Suarez, & Fereres, 2009; Olsen, Garner, & Van Dyke, 2002). Unfortunately, many of these approaches involve classification using a dozen or more wavelength bands, requiring sensors which are not typically available on planetary rovers. These approaches also ignore the potentially useful texture and geometry data that is available to ground-based robots, which operate in close proximity to the terrain.

In the field of robotics, terrain classification at a distance of several meters has been achieved using color, texture, geometry (via stereo or LIDAR), and even polarization data (Denes, Gottlieb, Kaminsky, & Huber, 1998). A variety of texture discrimination metrics have been described, including Gabor filters (Weldon, Higgins, & Dunn, 1996), wavelet-based fractal dimensions (Espinal, Huntsberger, Jawerth, &

Kubota, 1998), and receptive fields inspired by the human visual system (Balas, 2006; Malik & Perona, 1990). Various approaches for combining color, texture, and geometry have been proposed including naïve Bayes fusion (Shi & Manduchi, 2003), neural networks (Rasmussen, 2002), meta-classifier fusion (Halatci, Brooks, & Iagnemma, 2008), and semi-supervised fusion (Manduchi, 1999). These approaches are typically used in a supervised fashion, where the number and appearance of classes is known a priori. While (Rasmussen, 2002) addresses the classification problem in the context of road detection, most approaches make no attempt to associate traversability with the classification result. It should be noted that the work in this thesis relies on the visual classifier developed by Halatci, so Section 1.1 closely follows the approach presented in (Halatci, 2006; Halatci et al., 2008).

A limited amount of work has been performed in the area of classification based on proprioceptive terrain sensors such as accelerometers. Such an approach was proposed in (Iagnemma & Dubowsky, 2002), and a functional algorithm was presented in (Brooks & Iagnemma, 2005). A similar algorithm, intended for high-speed ground vehicles, was presented in (DuPont, Roberts, Selekwa, C. Moore, & Collins, 2005; Sadhukhan, 2004). These approaches are useful in classifying the terrain in contact with the rover's wheels, and the approach of Brooks & Iagnemma is described in Section 2.1 for this purpose. However due to its reliance on proprioceptive sensor data, this algorithm cannot be applied directly to classify terrain not in contact with the rover.

1.3.3 Machine Learning

The terrain classification and clustering approaches presented in this thesis take advantage of work in the field of machine learning. While both classification and

clustering have been studied extensively, only a small subset of the previously developed approaches are appropriate for use in a learning framework operating in a time-constrained scenario, and these will be described below.

For classification, support vector machines (SVM) have received significant attention due to the speed at which they can be trained as well as their success in classifying data from a wide variety of datasets (Schölkopf, 2000; Vapnik, 2000). Recent work has provided strict bounds on the classification error rate, given the error rate over the training data (Rakhlin, Mukherjee, & Poggio, 2006). An implementation of an SVM has also been developed for online applications, where training data is presented as a sequence rather than as a single batch (Kivinen, Smola, & Williamson, 2004). It is not appropriate for this thesis, however, because it relies on the conditional independence of sequential training examples—a poor assumption in the scenario considered here. SVM classifiers can be implemented with linear or polynomial kernels, which can reduce both training and classification time in situations when there is a large number of training examples. Details related to reducing the SVM classification time are presented in Appendix D, and SVMs are used extensively in this thesis.

Clustering, as opposed to classification, is a machine learning technique appropriate for situations when the classes are not known a priori, or when labeled training data is not available. It is the task of dividing unlabeled points into "clusters" of similar points. Traditional methods of clustering include the well-known k-means method as well as linkage-based methods derived from graph theory (Bishop, 1995; Brandes, Gaertler, & Wagner, 2003). These methods all rely heavily on the features used to

represent the data. They have not previously been applied to traversability-related terrain segmentation.

Another area of machine learning related to this research is that of novelty detection. Novelty detection is the task of classifying a point as "same" or "different" as compared to the training data, where there are no explicit examples of what is "different." This has occasionally been referred to as "one-class classification," and a one-class variant of the SVM classifier has been proposed (Schölkopf, Platt, Shawe-Taylor, Smola, & Williamson, 2001). Another approach is to model the distribution of the training data, for example using a mixture of Gaussians (MoG) model, and to label a new point as "different" if the modeled density at that point is lower than some threshold. A theoretical analysis of single-class classification strategies was presented in (El-Yaniv & Nisenson, 2007), and this analysis was the inspiration for the approach presented in 1.1. These novelty detection approaches have not previously been applied to terrain identification.

1.3.4 Mobility Prediction

An important aspect of mobility prediction is modeling the interaction between a wheel and the terrain. (Bekker, 1969) is the authoritative work in this field, describing measurable mechanical properties of deformable terrain and defining the relationship between these properties and the net forces and torques acting between the wheel and terrain. Similar work by Wong and Reece differs only in the role of wheel width in the force and torque equations (Wong, 2001; Wong & Reece, 1967). Both of these approaches require the use of dedicated equipment to measure the terrain properties.

To enable parametric terrain modeling in scenarios without dedicated equipment, Iagnemma proposed an approach for estimating terrain parameters using measurements

of the net forces and torques on a wheel (Iagnemma, Shibly, & Dubowsky, 2002; Iagnemma et al., 2004). It was demonstrated that a Kalman filter could be used to estimate the coefficients of a reduced-order Bekker model during a rover traverse. However the estimated terrain properties were not used to predict a measure of traversability of terrain. Kang extended that work and proposed a nondimensionalized drawbar pull—the drag force that would be required to hold the vehicle stationary—as a traversability metric (Kang, 2003; Iagnemma, Kang, Brooks, & Dubowsky, 2003). Kang proposed an approximate equation for drawbar pull as a function of wheel sinkage, wheel torque and vertical load.

Other researchers have attempted to quantify traversability in other ways. In (Seraji, 1999) a traversability index based on fuzzy logic was calculated as a function of terrain slope, rock size, and rock concentration. Another approach, the T-transformation, calculated a traversability index based on terrain slope and geometric roughness of the terrain (Ye & Borenstein, 2004). Neither of these approaches considered the mechanical properties of the terrain, making them incompatible with the notion of non-geometric hazards presented in this thesis.

1.4 Approach Overview

In order to appreciate the relationship between the algorithmic components developed in this thesis, it is useful to understand how they are integrated in an online terrain sensing framework. This section presents the concept of learning from experience, defines the terrain representation and terminology that will be used throughout the thesis, and then describes how each of the algorithmic components fit into the overall self-supervised learning framework.

1.4.1 Learning From Experience

As described in 1.2, the purpose of this thesis is to allow a rover to learn the relationship between mechanical terrain properties and terrain appearance, to enable it to predict the mechanical properties of distant terrain. Figure 1-3 illustrates the three stages of this learning process.

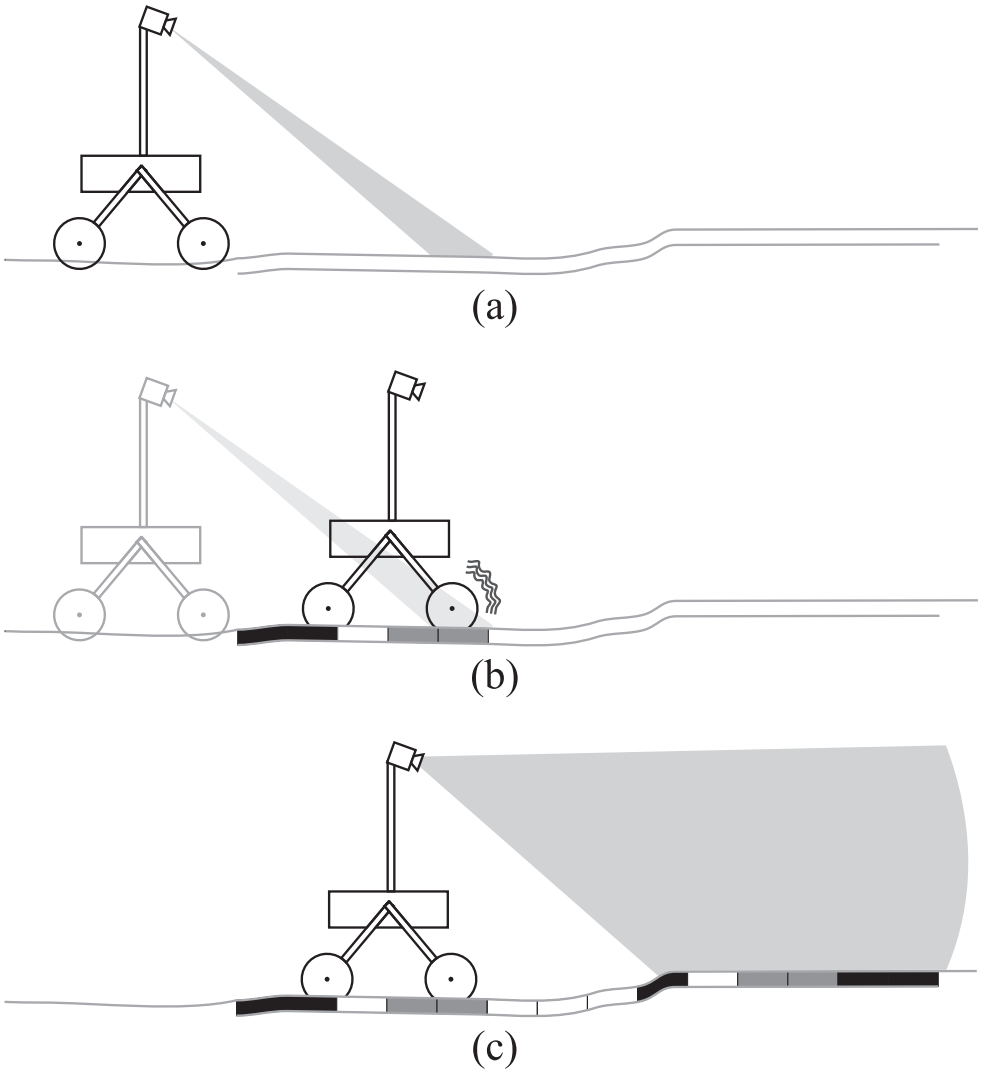

Figure 1-3. Schematic of proposed self-supervised classification framework

Initially, the rover has no knowledge of the relationship between the terrain appearance and its mechanical properties. From a given position, it is assumed that a

rover can sense the appearance of terrain using cameras (Figure 1-3(a)), but cannot yet predict its ability to traverse this terrain.

Figure 1-3(b) shows the rover after it has driven onto a patch of terrain that it previously sensed with its cameras. Using proprioceptive sensors (e.g. vibration sensors or torque sensors), the rover can sense the interaction between the rover wheels and terrain, and thus characterize the mechanical terrain properties which affect the mobility of the rover.

Once the rover has sensed the appearance of a patch of terrain and characterized its effect on rover mobility, it associates the features related to appearance with mobility properties. From this association, the rover can sense the appearance of terrain it has not yet traversed and predict that effect that terrain may have on the rover (Figure 1-3(c)). Thus, the rover has learned to predict the mobility properties of distant terrain from its experiences traversing terrain with a similar appearance.

1.4.2 Terrain Representation and Terminology

To avoid ambiguity in the description of the self-supervised classification framework and its algorithmic components, it is necessary to establish terminology to describe the terrain and the rover's sensors. This section introduces terminology for terrain patches, mechanical terrain properties, terrain classes, proprioceptive and exteroceptive sensors, and the terrain map.

Terrain Patch

In this thesis, terrain around a rover is divided into a regular grid of 20 cm by 20 cm terrain patches, whose locations are fixed in inertial space. Each patch is identified by

an x-coordinate indicating distance in front of the rover's starting position, and a y-coordinate indicating distance to the right of the rover's starting position, as illustrated in Figure 1-4. Thus, a terrain patch $P_{2.2,0.4}$ is the region of terrain located between 2.2 meters and 2.4 meters forward of the rover starting position, and between 0.4 and 0.6 meters right of the rover starting position. This grid is fixed with respect to the ground, so that as the rover travels its wheels come into contact with multiple terrain patches.

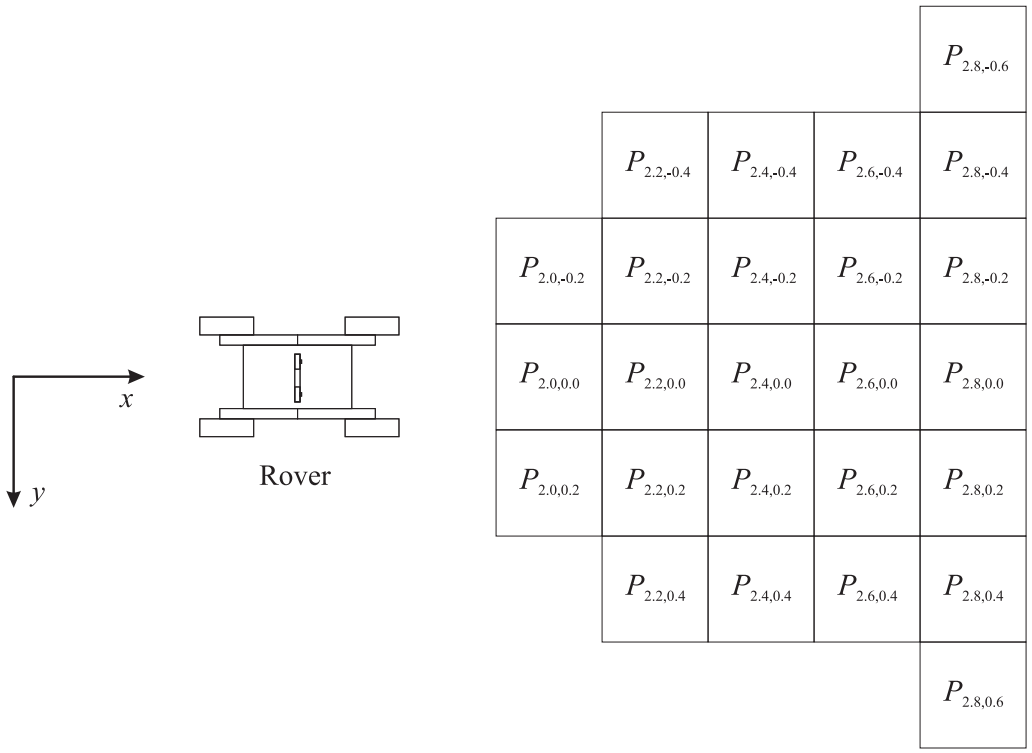

Figure 1-4. Sample overhead view showing regular grid of terrain patches in front of rover

Because terrain is generally not flat, each of the terrain patches may have non-planar topography. That topography is represented by a set of points in 3-D space located on the surface of the terrain. Since this grid-based representation has difficulty representing overhangs, it is assumed that no two points on the terrain surface are directly above one another (i.e. a 2½-D representation is assumed).

Mechanical Terrain Properties

For this thesis, mechanical terrain properties are measurable quantities that can be used to describe the forces and torques between a rover wheel and the terrain. For example, one mechanical terrain property is the maximum thrust force that a rover wheel could exert when in contact with a terrain patch. Here, the primary interest is in mechanical terrain properties that are useful in determining whether a terrain patch may be traversed safely.

Terrain Class

It is assumed that each terrain patch $P_{x,y}$ can be uniquely associated with a terrain class (e.g. "sand," "rock," and "beach grass"). A terrain class is a categorization for a terrain patch based on its mechanical properties: a terrain patch $P_{x1,y1}$ associated with terrain class "sand" will react differently to forces applied by the rover's wheel than would a terrain patch $P_{x2,y2}$ associated with terrain class "rock." In this thesis, terrain classes are categorizations of the mechanical properties of the terrain without regard to its topography. Thus, patches $P_{x1,y1}$ and $P_{x2,y2}$ may be associated with the same terrain class even if $P_{x1,y1}$ is nearly flat and $P_{x2,y2}$ has a steep slope.

It should be noted that terrain classes may be defined by human supervisors based on prior knowledge of the rover's environment, or they may be discovered by the rover through unsupervised learning (i.e. clustering). Human-defined terrain classes typically have some clear semantic interpretation: "sand," "rock," and "beach grass" are all easily understood. Terrain chasses discovered through clustering are not associated with semantic labels, so interpretation of the distinctions between classes may be more difficult.

Proprioceptive and Exteroceptive Sensors

Various sensors are used by the rover to sense its environment. These sensors are either exteroceptive or proprioceptive. Exteroceptive sensors, such as cameras, are able to directly sense features related to terrain. Proprioceptive sensors, such as wheel torque sensors or vibration sensors, are able to sense features related to the terrain only through the physical interaction between the rover wheels and terrain.

Because proprioceptive sensors function by measuring characteristics of wheel-terrain interaction, they are restricted to sensing terrain in direct contact with a rover wheel. In this thesis, sensor data is denoted S, with indices specifying the sensor and the time at which the sensor reading was recorded, for example $S_{torque,t=0}$. Given the position of the rover, it is trivial to identify the terrain patch $P_{x,y}$ with which proprioceptive sensor data $S_{torque,t=0}$ is associated.

Exteroceptive sensors can sense features related to terrain not in contact with the rover, and thus sensor data associated with multiple terrain patches may be sensed simultaneously. For example, an image $S_{camera,t}$ taken at time t can contain pixels associated with multiple terrain patches. To identify the terrain patch associated with a given pixel $S_{camera,t,i,j}$ located at row i and column j, the (stereo-derived) range data associated with that pixel ($S_{range,t,i,j}$) is needed, as well as the rover's position and orientation at time t.

Terrain Map

A terrain map is a rover's internal representation of the surrounding terrain around it. For this thesis, that representation includes the topography of each terrain patch that has been previously sensed, as well as the associated terrain class and mechanical terrain

properties. A sample terrain map is shown in Figure 1-5. Mechanical terrain properties calculated from proprioceptive sensor data are associated with terrain patches for which this proprioceptive data is available. Prediction of mechanical terrain properties for terrain patches which have not been sensed using proprioceptive sensors is the focus of this thesis.

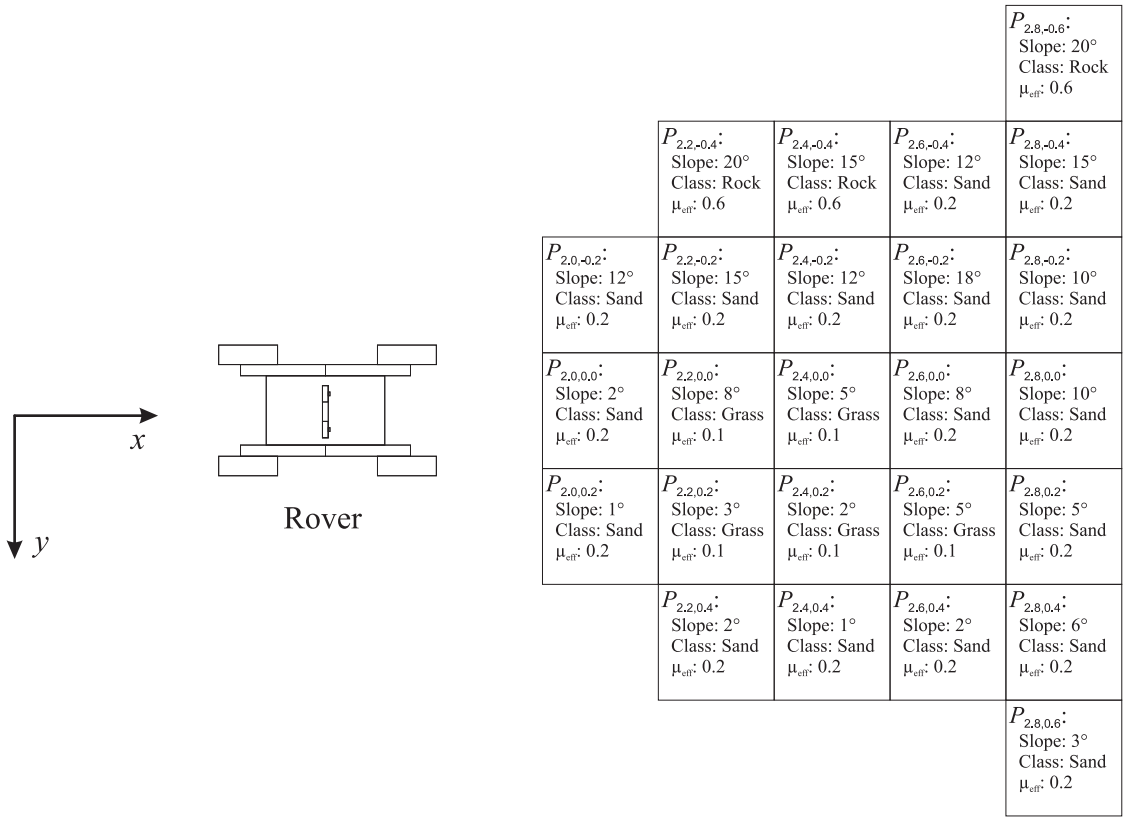

Figure 1-5. Sample terrain map showing data associated with terrain patches in front of rover (overhead view)

1.4.3 Self-Supervised Classification Framework and Algorithmic Components

In this framework, the learning process is divided among three distinct algorithms. The information flow between these algorithms is shown in Figure 1-6. The first algorithm is a proprioceptive terrain classifier, which takes proprioceptive sensor

data (e.g. wheel torque, sinkage, or vibration) as an input and returns a terrain class label as its output. The second algorithm is an exteroceptive terrain classifier, which is trained using labels from the proprioceptive terrain classifier.[5] Once trained, it takes exteroceptive sensor data (here, color stereo images of the terrain) as its input and returns terrain class labels for each of the terrain patches in its field of view. The third algorithm is a terrain characterization algorithm, which uses proprioceptive sensor data to estimate the mechanical terrain properties associated with each terrain class. The output of these three components is a terrain map that contains information about the mechanical terrain properties and topography of the terrain patches around the rover.

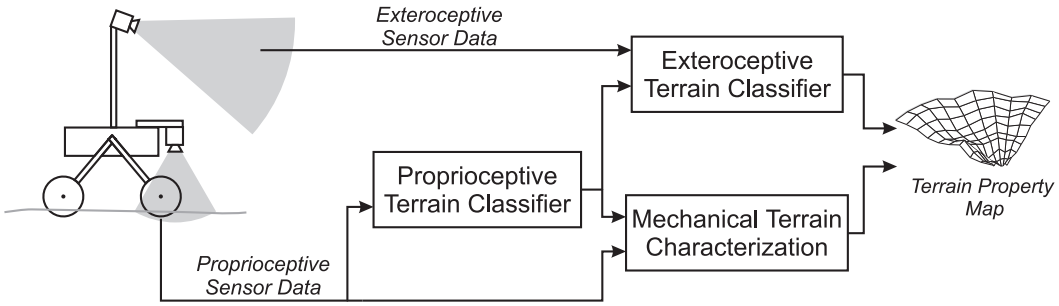

Figure 1-6. Information flow for self-supervised classification framework

Each of these algorithmic components is described in a separate chapter of this thesis. Proprioceptive terrain classification is presented in Chapter 2, exteroceptive terrain classification is presented in Chapter 3, and mechanical terrain characterization is presented in Chapter 4. The following subsections describe each of these algorithms in more detail.

[5] This approach is referred to as self-supervised classification because one classifier (in this case, the exteroceptive terrain classifier) is trained using data labeled by another classifier (in this case, the proprioceptive terrain classifier). In contrast, a supervised classifier is trained using data labeled by a human supervisor.

1.4.3.1 Proprioceptive Terrain Classification

The purpose of proprioceptive terrain classification is to classify terrain patches based on proprioceptive sensor data, such that terrain patches with similar mechanical properties are associated with the same terrain class, and terrain patches with significantly different mechanical properties are associated with different terrain classes. There are a number of potential approaches for accomplishing this task. This thesis presents three distinct approaches.

The first approach, presented in 2.1, relies on training of a supervised classifier to identify terrain classes based on proprioceptive sensor data, where these terrain classes are defined by a human supervisor during training. This requires a priori knowledge of the terrain classes in the rover's environment, and hand labeling of training data.

The second approach, investigated in 2.1, relies on unsupervised clustering to group terrain patches into classes based on proprioceptive sensor data. This approach eliminates the need for hand labeling of data. However, the terrain clusters are not associated with meaningful labels, so interpretations of the distinctions between terrain classes may be difficult. Also, this approach may require more clustered terrain classes to adequately represent the terrain compared to the first approach.

In the third approach, briefly addressed in 1.1, terrain patches are classified based on the mechanical terrain properties identified by the mechanical terrain characterization algorithm. Here, terrain classes are defined a priori to correspond to a range of mechanical terrain properties. This requires that the mechanical terrain characterization algorithm be executed frequently to accumulate training data for the exteroceptive terrain classifier, which may be more computationally expensive than either of the first two

approaches due to the nonlinear optimizations involved in computing the mechanical terrain properties.

1.4.3.2 Exteroceptive Terrain Classifier

The purpose of exteroceptive terrain classification is to classify terrain patches based on features derived from exteroceptive sensor data—in this case, color, visual texture, and topography. The approach proposed in this thesis is to use a two-stage classification process, as shown in Figure 1-7. First, a novel terrain detection stage identifies whether the terrain patch belongs to a known class. If the patch belongs to one of the known classes, the known terrain classifier is invoked. Otherwise, the patch is labeled as "unrecognized" in the terrain class map. The exteroceptive terrain classification algorithm is presented in Chapter 3.

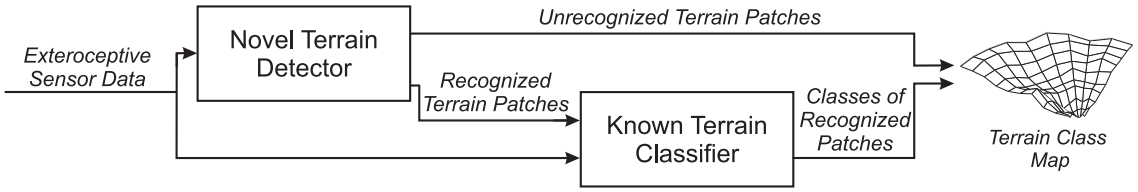

Figure 1-7. Information flow for classification using exteroceptive terrain classifier

1.4.3.3 Mechanical Terrain Characterization

The purpose of mechanical terrain characterization is to use proprioceptive sensor data to identify mechanical properties associated with a terrain patch. The approach presented in this thesis establishes bounds on the net traction force available at a given terrain patch. This approach is described in Chapter 4.

1.5 Contribution of this Thesis

The contribution of this thesis is the development and analysis of a self-supervised learning framework and component algorithms. This framework enables a planetary rover to accurately predict mechanical properties of terrain at a distance by learning from experiences gained during traverses of similar terrain. This work includes the development and validation of

- a self-supervised learning framework,
- supervised and unsupervised proprioceptive terrain classification algorithms,
- an exteroceptive novel terrain detection algorithm capable of identifying terrain patches not belonging to known terrain classes, and
- a mechanical terrain characterization algorithm capable of identifying bounds on the net traction force available at a given terrain patch.

1.6 Outline of this Thesis

This thesis is organized into six chapters, with five appendices. This chapter is the introduction, describing the motivation and related work and providing an overview of the approach.

Chapters 2, 3, and 4 present the development and validation of the algorithmic components used within the self-supervised learning framework. Chapter 2 addresses proprioceptive terrain classification, and presents two distinct approaches for classifying terrain patches based on proprioceptive sensor data. Chapter 3 addresses exteroceptive terrain classification, and presents methods for terrain classification and for identification of novel terrain (i.e. terrain patches that are not associated with any known class).

Chapter 4 addresses mechanical terrain characterization, and presents a method for identifying bounds on the net traction force available at a terrain patch.

Chapter 5 presents the development and experimental validation of the self-supervised framework itself, including a detailed description of how the algorithms from Chapters 2, 3, and 4 are employed in a terrain learning system suitable for novel environments. Chapter 6 presents conclusions and describes potential avenues for future research.

The five appendices present additional information related to the work presented in the thesis body. The first three appendices describe the experiments used to validate the algorithms described in this thesis. Appendix A contains details related to the four-wheeled rover, TORTOISE, that was used as a test platform for each of the algorithms. Appendix B contains details and images from the Wingaersheek Beach experimental test site. Appendix C contains details related to the wheel-terrain interaction testbed, the laboratory platform used to validate the mechanical terrain characterization approach. Appendix D presents general information on support vector machines and describes numerical optimization techniques that were used to speed up the classification process. Appendix E presents Matlab code to extract classification features from raw sensor data.

Chapter

2

Proprioceptive Terrain Classification

Proprioceptive terrain classification is the process of assigning class labels to terrain patches based on features derived from proprioceptive sensor data. Since the terrain classes are associated with mechanical properties, mechanically similar terrain patches should be assigned the same class label, while mechanically distinct terrain patches should be assigned different class labels.

This chapter presents two approaches for proprioceptive terrain classification. The first approach, presented in 2.1, uses a supervised classifier that has been trained by a human operator to classify vibration data. The second approach, presented in 2.1, uses an unsupervised clustering algorithm to group terrain patches into classes based on wheel torque.

2.1 Vibration-Based Terrain Classification

2.1.1 Introduction

This section (2.1) presents a method for classifying terrain patches based on vibrations induced in the rover structure by wheel-terrain interaction. Because mechanically distinct terrains induce distinct vibrations, features derived from these vibrations can be used to distinguish between them. This presents a means for

classification that is independent of the terrain patch's visual appearance and is thus inherently robust to changes in lighting conditions. The approach presented in this section relies on measurement of vibrations using an accelerometer mounted on the rover structure, representation of those vibrations in terms of the log-scaled power spectral density, and classification of the resulting features using a support vector machine (SVM) classifier. It uses a supervised classification framework, which relies on labeled vibration training data collected for each of the terrain classes during an offline learning phase.

Vibration-based terrain classification was suggested in 2002 by Iagnemma and Dubowsky as a novel sensing mode for classifying terrain for hazard detection (Iagnemma & Dubowsky, 2002). Other researchers demonstrated vibration-based terrain classification for a high-speed vehicle, but the accuracy deteriorated at low speeds (i.e. under 50 cm/s) where vibration amplitudes were reduced (DuPont et al., 2005; Sadhukhan, 2004; Weiss, Frohlich, & Zell, 2006). Thus, it would not be applicable to planetary rovers, whose speeds are expected to be under 15 cm/s.

The approach presented here for vibration-based terrain classification was initially developed in (Brooks, 2004) and (Brooks & Iagnemma, 2005), using a Fisher linear discriminant for classification. This section proposes an improved approach that employs an SVM classifier. It also describes experimental results from the Wingaersheek Beach environment. This is the same environment on which the complete self-supervised classification framework is experimentally validated in Chapter 5.

2.1.2 Approach

The vibration-based terrain classification algorithm presented here takes a signal-recognition approach to classifying terrain patches based on vibration signals. As such, it

learns to classify vibrations during an offline training phase in which it is presented with hand-labeled vibration signals. This is in contrast to an approach which might use a solid mechanics model to analytically predict how the rover structure will vibrate in response to interaction with terrain.

2.1.2.1 Description of Vibration Features

This algorithm represents each 1-second segment of vibration data as a vector of frequency-domain features. These features are calculated as follows. Given a time series of vibration signals $\mathbf{v}=[S_{vib,t=t0},\ldots,S_{vib,t=t0+1-1/Fs}]$ sampled at a frequency F_s, the first step is to compute the power spectral density (PSD), using Welch's method (Welch, 1967). Welch's method averages calculations of the power spectral density over eight subwindows to yield a 1025-element vector $\mathbf{p}$, where the ith element, $\mathbf{p}_i$, is the estimate of the power spectral density at a frequency of $F_s(i-1)/2048$. Thus, $\mathbf{p}$ is a time-shift-invariant representation of the vibration. To reduce the dominating effect of high-magnitude elements of $\mathbf{p}$, these magnitudes are log-scaled to yield a vector $\hat{\mathbf{p}}$:

$$\hat{\mathbf{p}}_i = \log(\mathbf{p}_i) \quad i = 1,...,1025.^{6} \tag{2-1}$$

The vibration feature vector $\mathbf{f}$, is the set of elements from $\hat{\mathbf{p}}$ which correspond to a frequency range of interest between F_{min} and F_{max}:

$$\mathbf{f}_i = \hat{\mathbf{p}}_{(i+\lceil 2048 F_{min}/F_s \rceil)} \quad i = 1,...,\left(\lfloor 2048 F_{min}/F_s \rfloor - \lceil 2048 F_{min}/F_s \rceil + 1\right). \tag{2-2}$$

Sample Matlab code for this feature extraction process is presented in Table E-1 in Appendix E.

[6] This logarithmic scaling also has the advantage of representing time-domain convolution with vector addition. Thus, the log-scaled PSD of the convolution of two signals is equal to the sum of their log-scaled PSDs.

For this work, vibrations are sampled at 44.1 kHz, which results in a spacing of 21.5 Hz between frequencies in the PSD estimate. The frequency range of interest is from 0 to 12 kHz. This yields a 558 element vibration feature vector (log-scaled PSD magnitudes) associated with each vibration segment.

2.1.2.2 Classifier Description

An SVM classifier was implemented to classify the vibration features using the open-source library LIBSVM (Chang & C. Lin, 2005, 2008). A Gaussian radial basis function (RBF) was used as the SVM kernel function, with parameters optimized by cross-validation over a set of vibration data not used for testing. (The optimized parameters were C=100 and $\gamma=5*10^{-5}$.) The LIBSVM option to return predicted class likelihood was enabled.

During the offline training phase, the SVM was trained to recognize distinct terrain classes using vibration features calculated from traverses of the rover over terrain patches corresponding to each of the known terrain classes. In the online terrain classification process, vibration features associated with unlabeled terrain patches were calculated and these features were fed into the SVM for classification.

2.1.3 Experiment Details

The performance of the vibration-based terrain classifier was studied using data from experiments with the Field and Space Robotics Laboratory (FSRL) Technology Testbed Rover, TORTOISE, in an outdoor beach environment.

2.1.3.1 Robot Configuration

TORTOISE, shown in Figure 2-1, is an 80-cm-long, 50-cm-wide, 90-cm tall robot with four 20-cm-diameter rigid aluminum wheels with grousers. The wheels on either side are connected to the main body and mast via a differential. A complete description of TORTOISE is presented in Appendix A.

Figure 2-1. Photo of TORTOISE, showing location of local sensor suite

TORTOISE measures vibration signals via a contact microphone mounted to the front right suspension strut of the rover, near the joint where the wheel axle passes through the strut, as seen in Figure 2-2. The vibration signals are recorded using the audio input of a laptop computer. During experiments, 16-bit samples of the vibration signal were collected at a frequency of 44.1kHz.

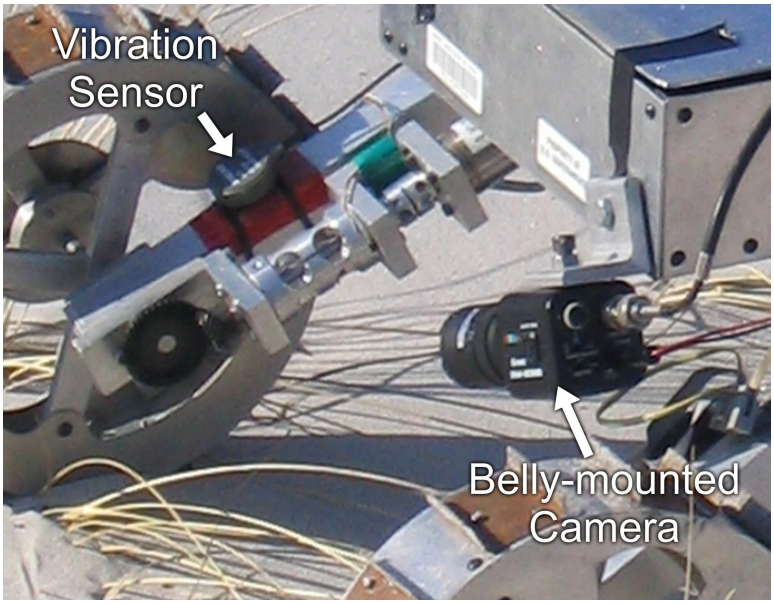

Figure 2-2. TORTOISE's local sensor suite, with vibration sensor and belly-mounted camera

For these experiments, TORTOISE's belly-mounted camera, shown in Figure 2-2, was used to collect images of the terrain being traversed. These images were used to allow a human to identify the terrain classes to serve as ground truth for classifier performance evaluation.

2.1.3.2 Experiment Environment

Experiments were performed at Wingaersheek Beach in Gloucester, MA. This is a sandy beach with a mixture of small and large rock outcrops (relative to the size of the rover) as well as loose rocks. This site was chosen due to its similarity in appearance to the MER landing sites on Mars. In this environment, sand and rock were considered to be two distinct terrain classes. To demonstrate the ability of the classifier to work in a multi-class setting, matted piles of beach grass were used as a third terrain class. These three terrain classes are identified in Figure 2-3. Further details about the experiment environment are presented in Appendix B.

Figure 2-3. TORTOISE on Wingaersheek Beach, showing terrain classes

Three experimental data sets were collected, each during a rover traverse of at least 15 meters along a straight-line path containing a combination of the three terrains. No two paths were identical. During experiments, TORTOISE traveled at a speed of 3 cm/s. In all, 2283 seconds (38 minutes) of vibration data were collected.

2.1.3.3 Data Processing

After the experiments, all vibration data was manually labeled to identify ground truth terrain classes, based on the appearance of the terrain in images collected by the belly-mounted camera. Among all of the data sets, 1593 one-second vibration segments were labeled as sand (1289 segments), beach grass (209 segments), or rock (95 segments).

For the results presented here, cross-validation was used. Thus, each data set was used for testing the classifier that was generated using the remaining data sets as training

data. Due to the reduced amount of training data, cross-validation is expected to under-predict the performance of a classifier generated using all three labeled data sets (Kohavi, 1995).

2.1.4 Results

The performance of the vibration-based terrain classifier was assessed by comparison to the hand-identified class labels (i.e., ground truth) using a receiver operating characteristic (ROC) curve, shown in Figure 2-4. Here the horizontal axis indicates the percentage of false positives (%FP) (e.g., instances when sand or beach grass were falsely identified as rock) and the vertical axis indicates the percentage of true positives (%TP) (e.g., instances when rock was correctly identified as rock). Each terrain class forms a curve on the plot, as the threshold for leaving terrain patches "unclassified" is adjusted. The end point of the curves represents the situation in which none of the terrain patches are left unclassified. Any combination of points on these curves can be achieved through proper selection of the threshold.

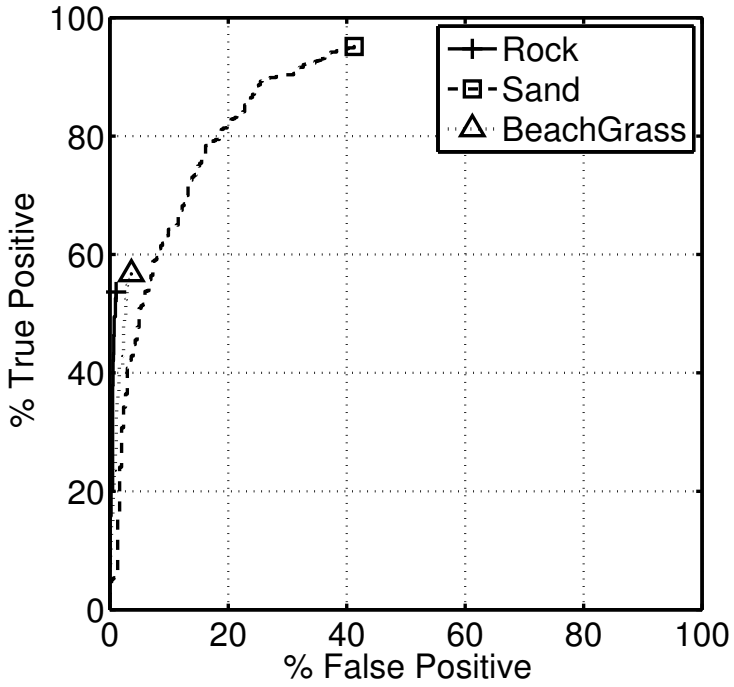

Figure 2-4. ROC curve for vibration-based terrain classifier

In this plot, it can be seen that the classifier exhibits very good discrimination between each of the terrain classes. More than 50% of the terrain patches associated with rock are correctly identified before more than 1% of the non-rock terrain patches are incorrectly identified as rock. Similarly, 50% of the terrain patches associated with beach grass are correctly identified before 3% of the rock and sand terrain patches are falsely identified as rock. Classification of the sand class is also accurate, when a higher classification threshold is used, with 50% of terrain patches associated with sand correctly identified before 5% of the non-sand terrain patches are incorrectly identified as sand. Thus, combining all three terrains, the vibration-based terrain classifier can classify 50% of the terrain patches while maintaining 92% confidence in the class label.[7]

For comparison, note that random assignment of classes to terrains would yield equal values for true positive and false positive, resulting in a straight line from (0,0)

[7] 92.3% confidence is based on the observed mixture of terrains: 6% rock, 13% beach grass, and 81% sand.

towards (100,100). By definition, random assignment into three classes yields only a 33% confidence in the class label.

It should be noted that the low true positive detection rates for rock and beach grass with all terrain patches labeled—54% and 57%, respectively—reflects the fact that there were fewer examples of these terrain classes in the training data than there were for sand. This implicitly gives these two terrain classes a lower prior probability in the final classification. Thus, while they are correctly identified less often than sand, they have a correspondingly lower false positive rate. If a detection rate higher than that shown in Figure 2-4 is desired, more training examples can be provided, or a higher weight can be placed on the existing examples when training the SVM.

2.1.5 Conclusions

In this section an approach has been presented for classifying terrain based on proprioceptive sensor data. It uses a supervised classification framework to distinguish terrain classes based on frequency-domain vibration features, where a human provides class labels during a training process.

The performance of this classification approach is measured by the relationship between the true positive rate and false positive rate for each terrain class. The balance between the fraction of terrain patches labeled and the confidence of the labeling can be adjusted by a threshold on the classification.

Experiments were performed with a four-wheeled rover, TORTOISE, in an outdoor beach environment, with three distinct terrain classes. Classification results from more than 1500 vibration segments demonstrate the ability of this approach to effectively

distinguish these three terrain classes. These results should be seen as an extension to the results presented in (Brooks, 2004) and (Brooks & Iagnemma, 2005).

The proposed algorithm is robust to variations in terrain appearance and lighting as it classifies terrain based solely on wheel-terrain interaction. As such, it presents a method for autonomous assignment of terrain patches to terrain classes, even when terrain appearance or lighting are not known a priori. It is in this role that the vibration-based terrain classification algorithm fits into the self-supervised classification framework presented in Chapter 5.

2.2 Proprioceptive Terrain Clustering

2.2.1 Introduction

In situations when terrain classes are not known in advance, supervised classification such as the vibration-based approach presented in 2.1 is infeasible. In such situations, unsupervised clustering can be used to separate terrain patches into distinct classes. This section presents a method for autonomously clustering terrain patches based on proprioceptive sensor data, thus establishing a set of classes that can be assigned to other terrain patches the rover encounters. Note that while these clusters (i.e. autonomously generated classes) do not necessarily correspond to the classes a human observer would identify, it will be shown that this approach can be used to successfully divide a set of terrain patches into mechanically distinct classes.

There are many possible approaches to clustering terrain patches into distinct classes, and several were investigated over the course of this research. Autonomous clustering based on the terrain patches' visual appearance (using the visual features described in 3.1.2) was studied briefly, but it was observed that the human-identified

terrain classes were not easily separable in that feature space. Another approach, based on clustering vibrations represented by the features described in 2.1.2, also proved to be difficult to separate by autonomous clustering, because the terrain classes have significant overlap in the feature space. This can be seen in Figure 2-5, which shows the distribution of vibrations sensed from each terrain class, as plotted against the first four principal components of the vibration features.

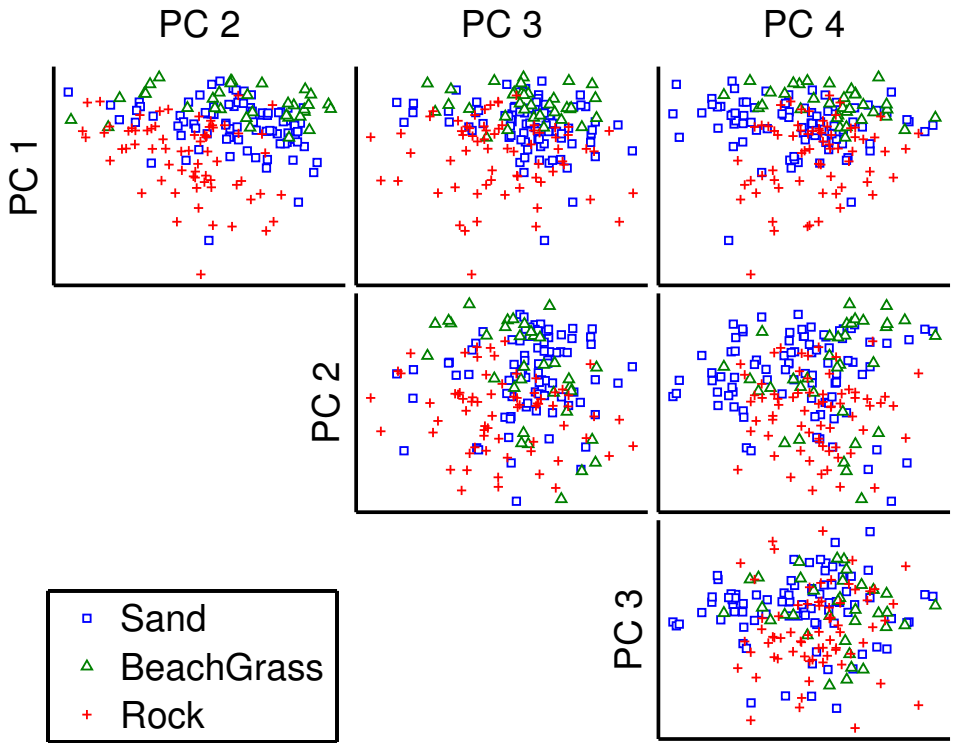

Figure 2-5. Vibration signals for three terrain classes plotted against first four principal components

Another observable quantity is the wheel torque. Various features of the wheel torque signal observed during normal driving were investigated for terrain clustering, from statistics of the raw signal (shown in Figure 2-6) to frequency-spectrum representations, but it was generally observed that large overlap between the human-identified terrain classes suggested that robust clustering would be unlikely to be achievable.

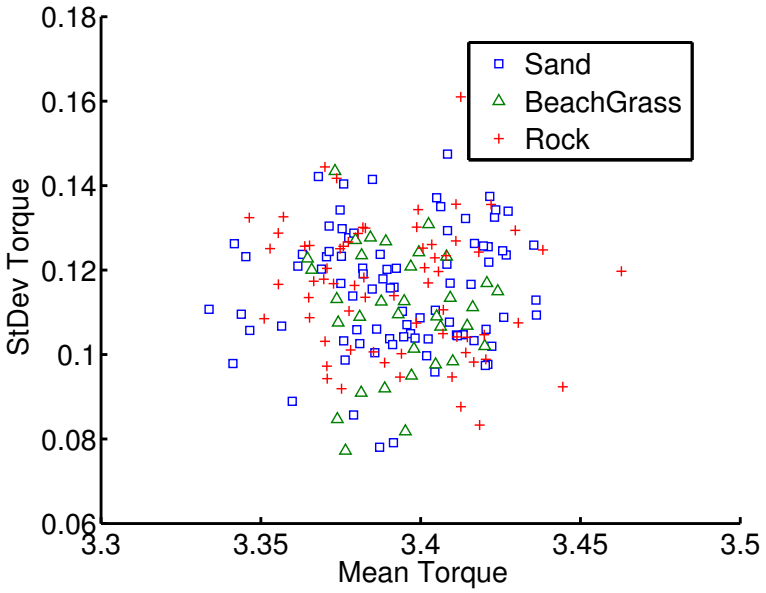

Figure 2-6. Scatter plot of three terrain classes illustrating overlap of statistics of time-windowed torque signal

The terrain clustering approach presented in this section attempts to extract features from the wheel torque signal during periods when the rover is intentionally inducing wheel slip. This wheel slip occurs by means of shear failures within the terrain or at the wheel-terrain interface, and the characteristics of this failure differ depending on the wheel-terrain interaction conditions. For instance, slip on rock occurs by means of failure at the wheel-terrain interface, while gross slip on sand occurs by means of shear failure below the surface of the sand. This difference in slip mechanism between the terrain classes results in significantly distinct torque signals. As a result, torque features sensed while a wheel is slipping are more widely separated in a candidate feature space than torque features sensed during normal driving, as illustrated by Figure 2-7. This separation means that the terrain classes may be more easily grouped into distinct clusters.

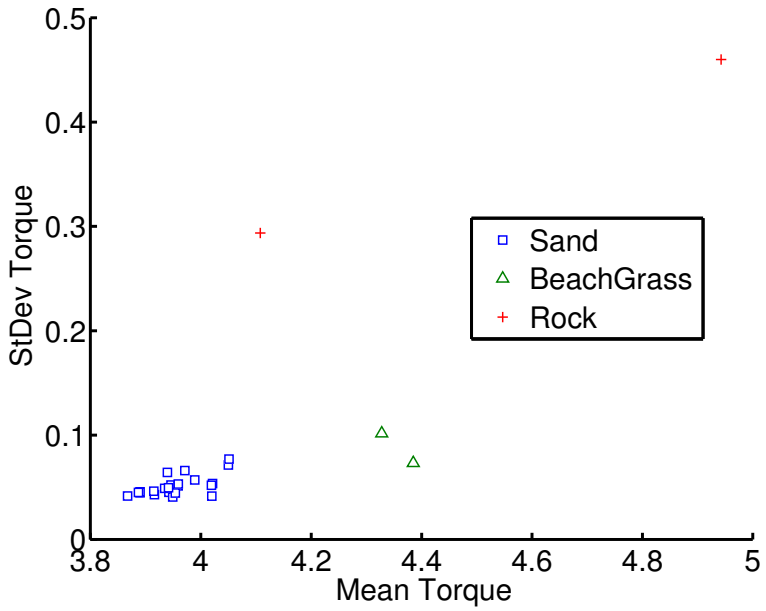

Figure 2-7. Scatter plot of torque signals from three terrain classes with induced wheel slip

Clustering relies on computational algorithms that take as inputs points in a (often high-dimensional) feature space and return a segmentation of those points into distinct clusters. Examples of clustering algorithms include basic *k*-means clustering as well as more advanced graph-theoretic methods and spectral clustering (Brandes et al., 2003). While there are situations in which one clustering algorithm will perform significantly better than others, most clustering algorithms will perform well if the points to be clustered are well separated in a given feature space. As this is the case for the torque features used here, a basic *k*-means clustering algorithm was employed.

2.2.2 Approach

The proprioceptive terrain clustering algorithm groups terrain patches along the rover's path into mechanically distinct clusters. To accomplish this, terrain patches are represented by features extracted from the torque applied to a rover wheel, and those features are fed into a *k*-means clustering algorithm. To increase the separation between

mechanically distinct terrain classes, the wheel torques are sensed while the rover intentionally induces slip between the wheel and the terrain.

2.2.2.1 Rover Wheel Slip Behaviors

To emphasize the difference between mechanically distinct terrains, wheel torque is sensed with the wheel slipping relative to the soil. By ensuring that the wheel is slipping, the torque is usually dictated by the wheel-terrain interaction conditions rather than the feedback control algorithm maintaining the wheel's speed. Two separate rover behaviors for inducing wheel slip were studied. The performance of segmentation using these behaviors is presented in 2.2.4.

The first slip-inducing behavior is termed "Incremental Slip" and is presented as Behavior 1 below. Here, after a period of normal driving, the rover drives the right front wheel faster than the other wheels. Since the rover body remains moving at (approximately) the longitudinal speed of the remaining wheels, wheel slip is induced under the faster-rotating wheel. Initially, the slip ratio[8] commanded is 33%. At t=3 seconds, the rover body speed is decreased, increasing the slip ratio to 50%. At t=6 seconds, the rover body is slowed down further, increasing the slip ratio to 67%. At t=9 seconds, the rover resumes normal driving. The process repeats while the rover traverses the terrain, allowing torque data to be collected at three distinct slip ratios.

[8] The slip ratio is defined as $1 - (v_x / \omega\, r)$, where v_x is the forward velocity of the wheel, ω is the angular velocity, and r is the wheel radius.

Behavior 1. Incremental Slip
1. *Normal Driving* – 11 seconds Drive all wheels at 3 cm/s 2. *33% Slip* – 3 seconds Drive right-front wheel at 4.5 cm/s and other wheels at 3 cm/s 3. *50% Slip* – 3 seconds Drive right-front wheel at 4.5 cm/s and other wheels at 2.25 cm/s 4. *67% Slip* – 3 seconds Drive right-front wheel at 4.5 cm/s and other wheels at 1.5 cm/s 5. Repeat

Note that the "Incremental Slip" results presented in 2.2.4 reflect clustering of wheel torque signals recorded during the second half of the 67% slip state. The 67% slip state was selected because the separation between terrain features was observed to be largest in the high-slip state. Additionally it was observed that by the second half of each slip state, the torque signals tended to have reached steady state or a limit cycle.

The second slip-inducing behavior is termed "Stop and Spin" and is presented as Behavior 2 below. Here, after a period of normal driving, the rover brakes all four wheels to bring the rover to a full stop. It then spins only the right front wheel, thus inducing 100% slip. The "Stop and Spin" results presented in 2.2.4 reflect clustering of wheel torque signals recorded during the second half of the spin state.

Behavior 2. Stop and Spin
1. *Normal Driving* – 10 seconds Drive all wheels at 3 cm/s 2. *Stop* – 1 second Brake all wheels 3. *Spin* – 4 seconds Drive right-front wheel at 3 cm/s and brake other wheels 4. Repeat

2.2.2.2 Torque Features

While the rover's right-front wheel is slipping, the torque is recorded at a sampling frequency F_s of 26.7 Hz, yielding a time series $\boldsymbol{\tau} = [S_{torque,t_0},...,S_{torque,t_1}]$. From

the torque signals recorded in each high-slip state—either 67% slip or spin, depending on the behavior—a single set of five features is extracted. For the state starting at time t_0 and ending at time t_1, these features are

1) mean torque, μ_τ (N m):

$$\mu_\tau = \frac{1}{\left\lfloor F_s\left(\frac{t_1 - t_0}{2}\right)\right\rfloor} \sum_{i=\left\lceil F_s\left(\frac{t_1-t_0}{2}\right)\right\rceil+1}^{F_s(t_1-t_0)+1} \boldsymbol{\tau}_i \quad , \tag{2-3}$$

2) standard deviation of torque, σ_τ (N m):

$$\sigma_\tau = \left(\left(\frac{1}{\left\lfloor F_s\left(\frac{t_1 - t_0}{2}\right)\right\rfloor - 1} \right) \sum_{i=\left\lceil F_s\left(\frac{t_1-t_0}{2}\right)\right\rceil+1}^{F_s(t_1-t_0)+1} \left(\boldsymbol{\tau}_i - \mu_\tau\right)^2 \right)^{1/2} \quad , \tag{2-4}$$

3) maximum torque, $\bar{\tau}$ (N m):

$$\bar{\tau} = \max_{i \in \left\{\left\lceil F_s\left(\frac{t_1-t_0}{2}\right)\right\rceil, \ldots, F_s(t_1-t_0)\right\}} \boldsymbol{\tau}_i \, , \tag{2-5}$$

4) minimum torque, $\underline{\tau}$ (N m):

$$\underline{\tau} = \min_{i \in \left\{\left\lceil F_s\left(\frac{t_1-t_0}{2}\right)\right\rceil, \ldots, F_s(t_1-t_0)\right\}} \boldsymbol{\tau}_i \, , \tag{2-6}$$

5) difference between maximum and minimum torque, r_τ (N m):

$$r_\tau = \bar{\tau} - \underline{\tau} \, . \tag{2-7}$$

This set of five features is combined into a vector, $\mathbf{f} = [\mu_\tau, \sigma_\tau, \bar{\tau}, \underline{\tau}, r_\tau]$, and passed to the clustering algorithm.

2.2.2.3 Clustering Algorithm

The torque features associated with all of the high-slip states from a single rover traverse of 15 to 20 meters are passed to the clustering algorithm.[9] Because the terrain

[9] In practice, the clustering algorithm could be run every few meters of a traverse, with the clustering results analyzed to see whether the new clusters are significantly better than the previous clusters.

classes of interest were observed to be well separated within the feature space, as was illustrated in Figure 2-7, a simple *k*-means clustering algorithm was used. For this work, the *k*-means algorithm is implemented using the `kmeans` function in Matlab's Statistics Toolbox. Pseudocode for the *k*-means algorithm is presented in Table 2-1. For the proprioceptive terrain clustering, between two and five clusters are used, and five replicates (i.e., repetitions of the algorithm using randomly selected initial values) are used to reduce the likelihood of the algorithm becoming trapped in a local minimum.

TABLE 2-1. PSEUDOCODE FOR *K*-MEANS CLUSTERING ALGORITHM

Given: N feature vectors
Initialize k cluster centers as random selections from feature vectors
for *i = 1 to 100*
  Calculate (L2) distance between each feature vector and each cluster center
  Assign each feature vector to the cluster with the closest cluster center
  if *no feature vectors have switched clusters,* ***then break***
  Calculate new cluster centers as the mean of the feature vectors in each cluster
  if any clusters have zero assigned feature vectors, exit with an error
next *i*
return *cluster assignments for each feature vector*

2.2.3 Experiment Details

As with the vibration-based terrain classifier presented in 2.1, the proprioceptive terrain clustering algorithm was tested using data from TORTOISE experiments on Wingaersheek Beach.

2.2.3.1 Robot Configuration

TORTOISE, shown in Figure 2-1, is a four-wheeled robot designed to test terrain-sensing algorithms for planetary rovers. Each of the four rigid aluminum wheels, fitted with short grousers, is driven by its own motor, allowing the speed of the wheels to be

controlled independently. A complete description of TORTOISE is presented in Appendix A.

For the proprioceptive terrain clustering algorithm, TORTOISE senses wheel torque using a torque sensor mounted to the motor driving the right front wheel, as seen in Figure 2-8. The torque signals are processed using an A/D converter on the rover's control computer and recorded at 26.7 Hz during experiments.

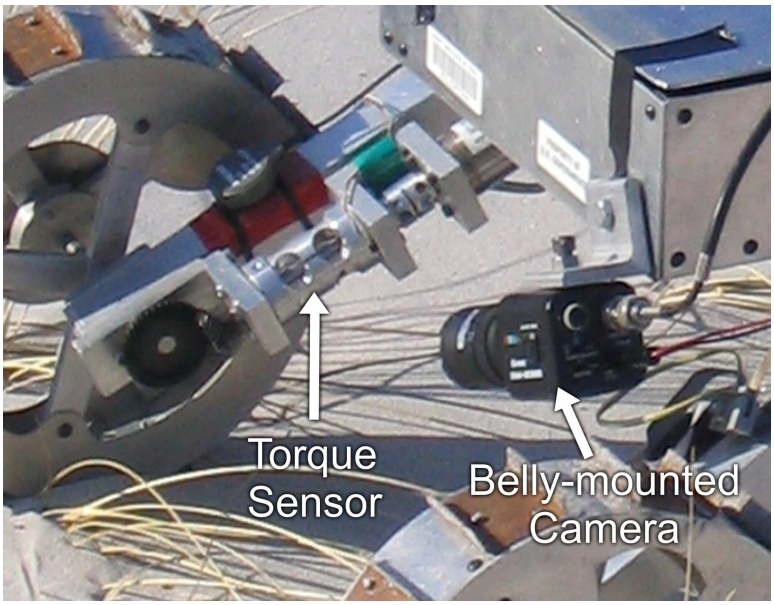

Figure 2-8. TORTOISE's local sensor suite, with torque sensor and belly-mounted camera

As with the vibration-based terrain classification, TORTOISE's belly-mounted camera, shown in Figure 2-8, was used to collect images of the terrain being traversed. After the experiments, these images were used to identify terrain classes to serve as ground truth.

2.2.3.2 Experiment Environment

Wingaersheek Beach was used as the experiment environment for the proprioceptive terrain segmentation experiments. The three distinct terrain classes were

sand, rock, and beach grass. These terrain classes are identified in Figure 2-3. Full details about the experiment environment are presented in Appendix B.

Sixteen experimental data sets were collected, each set corresponding to a rover traverse along a straight-line path containing a combination of the three terrains. No two paths were identical. For seven of the data sets, the rover executed Behavior 1 ("Incremental Slip") described in 2.2.2, totaling 101 slip cycles. For the other nine data sets, the rover executed Behavior 2 ("Stop and Spin"), totaling 237 spin cycles.

2.2.3.3 Data Processing

After the data was collected, all of the terrain traversed by the rover was manually labeled, using images from the belly-mounted camera to identify the ground truth terrain class. Of the "incremental slip" data sets, 55 of the slip cycles had the right front wheel in contact with sand, 13 with beach grass, and 5 with rock. Of the "stop and spin" data sets, 164 of the cycles had the right front wheel in contact with sand, 12 with beach grass, and 11 with rock. Cycles in which the terrain in contact with the right front wheel is unclear were not labeled.

For each of the data sets, torque feature vectors associated with all cycles (labeled and unlabeled) were passed to the clustering algorithm. Thus, the clustering algorithm clustered the torque features from each data set without using any information from the other data sets, and the performance of the clustering was evaluated separately for each data set. The robustness of the algorithm was assessed by comparing the clustering performance across all data sets.

2.2.4 Results

The results of experimental torque data clustering are presented in Table 2-2. Here, algorithm performance is measured by its ability to separate the three human-labeled terrain classes (i.e. sand, rock, and beach grass). Specifically, the "maximum classification accuracy" metric is the largest fraction of terrain that can be classified correctly, subject to the limitation that all terrain within the same cluster must be assigned the same class label. This metric has the benefit of being insensitive to arbitrary ordering of the clusters, and it does not penalize a clustering algorithm that is able to detect finer distinctions than the hand-labeled classes. It should be noted, however, that even the worst clustering approach will achieve a maximum classification accuracy equal to the fraction of terrain belonging to the most common class. (This means that if 85% of the terrain is sand, even randomly assigned clusters will have a maximum classification accuracy of at least 85%.) This baseline accuracy is noted in the top row of the table. The percentages listed are the mean of the performances observed across all data sets. The numbers in brackets indicate 95% confidence intervals for the mean.

TABLE 2-2. PERFORMANCE OF PROPRIOCEPTIVE TERRAIN CLUSTERING ALGORITHM

Number of Clusters	Maximum Classification Accuracy	
	Incremental Slip Behavior (Baseline: 80.0%)	Stop and Spin Behavior (Baseline: 87.4%)
2	83.8% [78.9% - 88.8%]	94.1% [89.2% - 99.1%]
3	86.5% [81.5% - 91.4%]	97.7% [94.8% - 100%]
4	87.4% [80.8% - 94.1%]	99.3% [98.3% - 100%]
5	88.2% [81.8% - 94.5%]	98.9% [97.7% - 100%]

The second column of the table shows the performance of the proprioceptive terrain clustering algorithm when used to cluster data from the "incremental slip" data sets. For these data sets, 80% of the terrain traversed is sand, so this represents the minimum performance of a clustering algorithm. Here, algorithm performance improves as the number of clusters is increased, but the mean performance does not reach even 90% when the terrain is divided into five clusters – two more clusters than absolutely necessary for 100% correct classification.

The third column of the table shows the performance of the terrain clustering algorithm when clustering data from the "stop and spin" data sets. For these data sets, 87.4% of the terrain traversed is sand, so this represents the baseline performance. Here it can be seen that the terrain clustering algorithm performs significantly better than the baseline even when only two clusters are used. As the number of clusters is increased, performance also increases, and when four clusters are used, more than 99% of the terrain is correctly classified based on the cluster labels. The small decrease in performance as the number of clusters is increased to five does not appear to be statistically significant.

2.2.5 Conclusions

Section 1.1 has presented a second algorithm for separating terrain into classes based on proprioceptive sensor data. It uses unsupervised clustering to divide terrain into clusters, where the terrain is represented by features of the wheel torque signal. By operating on the wheel torque signal recorded while the wheel is slipping relative to the terrain, this clustering approach groups terrains based on properties affecting the mechanical interaction between the wheel and the terrain. This approach is inherently insensitive to the terrain appearance.

This approach was validated using data collected during experiments with a four-wheeled rover in a natural beach environment with three distinct terrain classes. By comparing the output terrain clusters to human-identified terrain classes, the performance of the clustering algorithm can be assessed. Clustering results were compared for two behaviors by which the rover can induce wheel slip. The results demonstrate that clustering of torque data collected during the “stop and spin” behavior is more robust than that of the “incremental slip” behavior. This difference is likely due to the rolling contact in the "incremental slip" behavior disengaging the wheel from the terrain at load-bearing points before the failure threshold was reached, thereby masking the difference in material properties within the terrains. This decrease in maximum torque is particularly evident when the wheel is spinning on rock. The robustness of the clustering of the “stop and spin” data sets was observed to be very good.

As with the vibration-based terrain classification algorithm, the proprioceptive terrain clustering algorithm serves as a method for assigning labels to terrain based on features derived from wheel terrain interaction. Whereas vibration-based terrain

classification is appropriate for situations when representative terrain vibrations may be hand-labeled during a training phase, proprioceptive terrain clustering is appropriate for completely autonomous situations, when human supervision is unavailable. By robustly separating the terrain patches into mechanically distinct clusters using proprioceptive sensor data, this algorithm fits into the self-supervised classification framework (Chapter 5) as a proprioceptive terrain classifier.

Chapter

3

Exteroceptive Terrain Classification

Exteroceptive terrain classification is the process of assigning class labels to terrain patches based on vision data collected from a rover's cameras. This chapter presents a two-stage approach to this classification, as shown in Figure 3-1. The visual terrain classifier is presented in 3.0. When presented with visual data associated with a terrain patch, this classifier identifies which of the known classes (i.e. classes for which the classifier has training data) appears most similar to the newly observed patch. In a situation in which some of the observed classes have no training data—either because the rover is encountering an unexpected terrain class, or because terrain patches to use for training have not yet been identified for some of the terrain classes—a separate stage is necessary to identify when the newly observed patch lies outside the set of known classes. This "novelty terrain detection" stage is presented in 3.1.

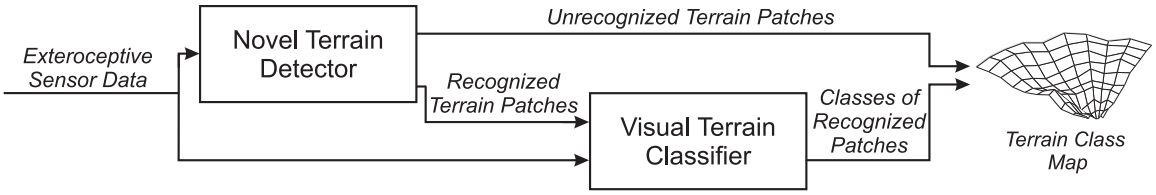

Figure 3-1. Information flow for exteroceptive terrain classifier

3.1 Visual Terrain Classification

3.1.1 Introduction

Classification of terrain using visual features is an area that has received significant previous attention, from scientists studying land use (Olsen et al., 2002) to engineers designing navigation systems for autonomous robots (Rasmussen, 2002). In this thesis, the visual terrain classification approach of Halatci is followed closely (Halatci, 2006; Halatci et al., 2008). This approach represents the appearance of a terrain patch via color, visual texture, and geometric feature vectors. For each of these three sensing modes, a SVM classifier is used to estimate likelihoods of the terrain patch belonging to each of the known terrain classes. The three sensing modes are then combined using naïve Bayes fusion to estimate the combined class likelihoods. The terrain patch is classified as belonging to the terrain class with the highest likelihood.

Much of the development of the algorithm presented in this section (1.1) was performed by Halacti for his Master's thesis, though both the visual texture and geometric features have small modifications from that presented in (Halatci et al., 2008). The algorithm description is included here as it is a critical component of the self-supervised classification system, and the visual features used in this classifier form the foundation of the novel terrain detection approach presented in 1.1. This section will also present detailed results for visual classification of terrains in the Wingaersheek Beach environment, for direct comparison to the self-supervised classification results in Chapter 5.

3.1.2 Approach

Here, exteroceptive terrain classification operates by extracting visual features from terrain observed using a stereo pair of color cameras. Separate SVM classifiers for each sensing mode—color, visual texture, and range—are used to predict the likelihood that a particular terrain patch belongs to any given terrain class. The resulting class likelihoods are combined using naïve Bayes fusion to yield a combined class assignment.

3.1.2.1 Visual Features

The appearance of a terrain patch is represented as a set of feature vectors derived from the color, visual texture, and geometry of the terrain. These features are all extracted from color images collected using a stereo pair.

3.1.2.1.1 Color

Color data is directly available from the cameras as red, green, and blue (RGB) intensities. However, the illumination intensity affects all three values in a raw RGB representation, which can lead to poor classification results. To reduce the effect of the overall illumination level, a modified hue, saturation, and value (HSV) representation of color is used as in (Sofman et al., 2006). In this approach, hue (an angle) is represented as two values—sin(hue) and cos(hue)—to eliminate the artificial discontinuity at 2π. Thus, color is represented as a 4-element vector: [sin(hue), cos(hue), saturation, value].

3.1.2.1.2 Visual Texture

Visual texture is a measure of the local spatial variation in the intensity of an image. Researchers have proposed many metrics for visual texture, such as Gabor filters and local energy methods (Bouman & Liu, 1991; Reed & du Buf, 1993). The work in this

thesis uses a wavelet-based approach, similar to the one demonstrated in (Espinal et al., 1998). Here, a grayscale image is decomposed with the Haar wavelet (Strang, 1993). Three scales of wavelets are used, each scale having horizontal, diagonal, and vertical wavelets, corresponding to estimating the derivative of the intensity in the horizontal, diagonal, and vertical directions at each length scale. The scales used are 2, 4, and 8 pixels. Because this process is sensitive to local changes in intensity, the magnitudes of the wavelet coefficients are then averaged over windows of 11, 9, and 7 wavelets. Thus, visual texture is represented by a 9-element vector, composed of the window-averaged horizontal, diagonal, and vertical wavelet coefficients at each scale.

The visual texture features are calculated using the following procedure. First, the 640 pixel × 480 pixel color image I (with all $I_{i,j,color} \in [0,1]$) is converted to a grayscale image G using Matlab's `rgb2gray` function, such that

$$G_{i,j} = 0.2989\, I_{i,j,red} + 0.587\, I_{i,j,green} + 0.114\, I_{i,j,blue}, \tag{3-1}$$

for i=1,…,480 and j=1,…,640.[10] Texture based on the grayscale image is calculated using the Haar wavelet. Here, the low-pass wavelet l is [0.25, 0.5, 0.25], and the high-pass wavelet h is [-0.5, 0, 0.5]. Using these wavelets four images are calculated, each of which has half the resolution of G: $A1$, which has the low-pass wavelet applied in both the horizontal and vertical directions, as

$$A1_{i,j} = \begin{cases} \sum_{m=1}^{3}\sum_{n=1}^{3} l_m l_n G_{2i+m-2,2j+n-2} & i = 2,...,239 \;\; j = 2,...,319 \\ 0 & i = 1,240 \;\; j = 1,...,320 \text{ or } i = 1,...,240 \;\; j = 1,320; \end{cases} \tag{3-2}$$

[10] The constants in Equation (3-1) were specified within the `rgb2gray` function.

V1, which has the low-pass wavelet applied in the horizontal direction, and the high-pass wavelet applied in the vertical direction, as

$$V1_{i,j} = \begin{cases} \sum_{m=1}^{3}\sum_{n=1}^{3} h_m l_n G_{2i+m-2,2j+n-2} & i = 2,...,239 \;\; j = 2,...,319 \\ 0 & i = 1,240 \;\; j = 1,...,320 \text{ or } i = 1,...,240 \;\; j = 1,320; \end{cases} \tag{3-3}$$

H1, which has the high-pass wavelet applied in the horizontal direction and the low-pass wavelet applied in the vertical direction, as

$$H1_{i,j} = \begin{cases} \sum_{m=1}^{3}\sum_{n=1}^{3} l_m h_n G_{2i+m-2,2j+n-2} & i = 2,...,239 \;\; j = 2,...,319 \\ 0 & i = 1,240 \;\; j = 1,...,320 \text{ or } i = 1,...,240 \;\; j = 1,320; \end{cases} \tag{3-4}$$

and *D1*, which has the high-pass wavelet applied in both directions, as

$$D1_{i,j} = \begin{cases} \sum_{m=1}^{3}\sum_{n=1}^{3} h_m h_n G_{2i+m-2,2j+n-2} & i = 2,...,239 \;\; j = 2,...,319 \\ 0 & i = 1,240 \;\; j = 1,...,320 \text{ or } i = 1,...,240 \;\; j = 1,320. \end{cases} \tag{3-5}$$

Here *H1*, *D1*, and *V1* contain directional derivative information at the 2-pixel scale, and *A1* contains a low-pass-filtered version of the grayscale image at ½ of the original dimensions.

To calculate the directional derivatives at the 4-pixel scale, the wavelets are applied to *A1*. *A2* has the low-pass wavelet applied in both horizontal and vertical directions:

$$A2_{i,j} = \begin{cases} \sum_{m=1}^{3}\sum_{n=1}^{3} l_m l_n A1_{2i+m-2,2j+n-2} & i = 2,...,119 \;\; j = 2,...,159 \\ 0 & i = 1,120 \;\; j = 1,...,160 \text{ or } i = 1,...,120 \;\; j = 1,160. \end{cases} \tag{3-6}$$

V2 has the low-pass wavelet applied in the horizontal direction and the high-pass wavelet applied in the vertical direction:

$$V2_{i,j} = \begin{cases} \sum_{m=1}^{3}\sum_{n=1}^{3} h_m l_n A1_{2i+m-2,2j+n-2} & i = 2,...,119 \;\; j = 2,...,159 \\ 0 & i = 1,120 \;\; j = 1,...,160 \text{ or } i = 1,...,120 \;\; j = 1,160. \end{cases} \quad (3\text{-}7)$$

H2 has the high-pass wavelet applied in the horizontal direction and the low-pass wavelet applied in the vertical direction:

$$H2_{i,j} = \begin{cases} \sum_{m=1}^{3}\sum_{n=1}^{3} l_m h_n A1_{2i+m-2,2j+n-2} & i = 2,...,119 \;\; j = 2,...,159 \\ 0 & i = 1,120 \;\; j = 1,...,160 \text{ or } i = 1,...,120 \;\; j = 1,160. \end{cases} \quad (3\text{-}8)$$

D2 has the high-pass wavelet applied in both directions:

$$D2_{i,j} = \begin{cases} \sum_{m=1}^{3}\sum_{n=1}^{3} h_m h_n A1_{2i+m-2,2j+n-2} & i = 2,...,119 \;\; j = 2,...,159 \\ 0 & i = 1,120 \;\; j = 1,...,160 \text{ or } i = 1,...,120 \;\; j = 1,160. \end{cases} \quad (3\text{-}9)$$

Thus, *H2*, *D2*, and *V2* contain the directional derivative information at the 4-pixel scale and *A2* contains a low-pass-filtered version of the grayscale image at ¼ of the original dimensions.

To compute the directional derivative information at the 8-pixel scale, the wavelet filtering process is applied to *A2*. *V3*, *H3*, and *D3* are calculated as

$$V3_{i,j} = \begin{cases} \sum_{m=1}^{3}\sum_{n=1}^{3} h_m l_n A2_{2i+m-2,2j+n-2} & i = 2,...,59 \;\; j = 2,...,79 \\ 0 & i = 1,60 \;\; j = 1,...,80 \text{ or } i = 1,...,60 \;\; j = 1,80. \end{cases} \quad (3\text{-}10)$$

$$H3_{i,j} = \begin{cases} \sum_{m=1}^{3}\sum_{n=1}^{3} l_m h_n A2_{2i+m-2,2j+n-2} & i = 2,...,59 \;\; j = 2,...,79 \\ 0 & i = 1,60 \;\; j = 1,...,80 \text{ or } i = 1,...,60 \;\; j = 1,80. \end{cases} \quad (3\text{-}11)$$

$$D3_{i,j} = \begin{cases} \sum_{m=1}^{3}\sum_{n=1}^{3} h_m h_n A2_{2i+m-2,2j+n-2} & i = 2,...,59 \;\; j = 2,...,79 \\ 0 & i = 1,60 \;\; j = 1,...,80 \text{ or } i = 1,...,60 \;\; j = 1,80. \end{cases} \quad (3\text{-}12)$$

Given the directional derivatives on the 2-, 4-, and 8-pixel scales, the texture features are the means of the directional derivatives calculated over 11-, 9-, and 7-wavelet windows. Thus, the first texture feature, *fh3*, for the pixel located at (*i*,*j*), which is a measure of the horizontal derivative at the 8-pixel scale, is calculated as the mean of a 7 × 7 block of pixels in *H3*:

$$fh3 = \frac{1}{7 \cdot 7} \sum_{m=1}^{7} \sum_{n=1}^{7} H3_{\lceil i/8 \rceil + m - 4, \lceil j/8 \rceil + n - 4}. \tag{3-13}$$

where $i \in \{1,...,480\}$ and $j \in \{1,...,640\}$. For this calculation, *H3* is assumed to be zero outside the region in which it was defined. The other texture features associated with this pixel—*fd3*, *fv3*, *fh2*, *fd2*, *fv2*, *fh1*, *fd1*, and *fv1*—are calculated using the same approach of averaging the derivatives over windows:

$$fd3 = \frac{1}{7 \cdot 7} \sum_{m=1}^{7} \sum_{n=1}^{7} D3_{\lceil i/8 \rceil + m - 4, \lceil j/8 \rceil + n - 4}. \tag{3-14}$$

$$fv3 = \frac{1}{7 \cdot 7} \sum_{m=1}^{7} \sum_{n=1}^{7} V3_{\lceil i/8 \rceil + m - 4, \lceil j/8 \rceil + n - 4}. \tag{3-15}$$

$$fh2 = \frac{1}{9 \cdot 9} \sum_{m=1}^{9} \sum_{n=1}^{9} H2_{\lceil i/4 \rceil + m - 5, \lceil j/4 \rceil + n - 5}. \tag{3-16}$$

$$fd2 = \frac{1}{9 \cdot 9} \sum_{m=1}^{9} \sum_{n=1}^{9} D2_{\lceil i/4 \rceil + m - 5, \lceil j/4 \rceil + n - 5}. \tag{3-17}$$

$$fv2 = \frac{1}{9 \cdot 9} \sum_{m=1}^{9} \sum_{n=1}^{9} V2_{\lceil i/4 \rceil + m - 5, \lceil j/4 \rceil + n - 5}. \tag{3-18}$$

$$fh1 = \frac{1}{11 \cdot 11} \sum_{m=1}^{11} \sum_{n=1}^{11} H1_{\lceil i/2 \rceil + m - 6, \lceil j/2 \rceil + n - 6}. \tag{3-19}$$

$$fd1 = \frac{1}{11 \cdot 11} \sum_{m=1}^{11} \sum_{n=1}^{11} D1_{\lceil i/2 \rceil + m - 6, \lceil j/2 \rceil + n - 6}. \tag{3-20}$$

$$fv1 = \frac{1}{11 \cdot 11} \sum_{m=1}^{11} \sum_{n=1}^{11} VI_{\lceil i/2 \rceil + m - 6, \lceil j/2 \rceil + n - 6}. \quad (3\text{-}21)$$

Thus, the texture feature vector for the pixel located at (i,j) is the 9-element vector [*fh3*, *fd3*, *fv3*, *fh2*, *fd2*, *fv2*, *fh1*, *fd1*, *fv1*].

3.1.2.1.3 Geometry

Terrain geometry is available through stereo image processing. The raw output of a stereo processing algorithm is a cloud of range data points. Here the points are divided into a grid of 20-cm by 20-cm terrain patches projected onto a horizontal plane. The geometric features are statistics calculated from the elevation of points associated with each terrain patch. When calculating the features, the n points associated with a given terrain patch are represented as a $n \times 3$ matrix denoting each point's position in the [forward, right, down] coordinate frame with its origin at the rover's starting position: $\mathbf{P} = \{\mathbf{p}_1, \ldots, \mathbf{p}_n\}^T$.

The first element of the geometric feature vector is the average slope of the terrain, defined as the angle φ between the least-squares-fit plane and the horizontal plane, in radians. To calculate φ, the first step is to calculate the 3×3 covariance matrix, $\mathbf{C}$:

$$\mathbf{C}_{i,j} = \frac{1}{n} \sum_{k=1}^{n} \left(\mathbf{P}_{k,i} - \frac{1}{n} \sum_{l=1}^{n} \mathbf{P}_{l,i} \right) \left(\mathbf{P}_{k,j} - \frac{1}{n} \sum_{l=1}^{n} \mathbf{P}_{l,j} \right), \quad \text{for } i = 1,2,3 \quad j \in \{1,2,3\}. \quad (3\text{-}22)$$

The minimum eigenvalue s of $\mathbf{C}$ and its corresponding eigenvector $\mathbf{u}$ can be calculated using singular value decomposition, such that

$$\{s, \mathbf{u}\} = \underset{s \in \Re, \mathbf{u} \in \Re^{3 \times 1}}{\arg\min} s \quad \text{where } \mathbf{u} \cdot \mathbf{u} = 1, \mathbf{C}\mathbf{u} = \mathbf{u}s. \quad (3\text{-}23)$$

Since $\mathbf{u}$ is a unit vector normal to the least-squares-fit plane, φ can be calculated as

$$\varphi = \left|\arccos\left(\mathbf{u} \cdot \hat{\mathbf{z}}\right)\right|, \tag{3-24}$$

where $\hat{\mathbf{z}}$ is a unit vector pointing down.

The second element is the mean-squared deviation from that plane along its normal, $\sigma_{\perp}^2$. Here, this value is the same as the minimum singular value of the covariance matrix, so

$$\sigma_{\perp}^2 = s\,. \tag{3-25}$$

The third element is the variance in the height of the range data points, σ_z^2, calculated as

$$\sigma_z^2 = \frac{1}{n}\sum_{k=1}^{n}\left(\mathbf{p}_k \cdot \hat{\mathbf{z}} - \frac{1}{n}\sum \mathbf{p}_k \cdot \hat{\mathbf{z}}\right)^2. \tag{3-26}$$

The fourth element is the height difference between the highest and lowest points within the patch, r_z:

$$r_z = \max\left(\mathbf{p}_k \cdot \hat{\mathbf{z}}\right) - \min\left(\mathbf{p}_k \cdot \hat{\mathbf{z}}\right). \tag{3-27}$$

Thus, the geometry of each patch is represented as a 4-element vector: [φ, $\sigma_{\perp}^2$, σ_z^2, r_z]. These features were chosen based on the work of Halatci who used a similar feature set for classification of terrain in images collected by the Mars Exploration Rovers (Halatci et al., 2008). The Matlab code (Mathworks, 2005) for this terrain geometry feature extraction process is presented in Table E-2 in Appendix E.

3.1.2.2 Classifier Description

The visual terrain classifier uses a support vector machine classifier, implemented using the open-source library LIBSVM (Chang & C. Lin, 2005, 2008), as was used for the vibration-based terrain classifier presented in 2.1. For visual classification, linear or

low-order polynomial kernels are appropriate, because optimizations can allow for very fast classification (see Appendix D for details). Here, a linear kernel is used, with the cost factor C optimized by cross-validation over a subset of images used for training. (For this work the optimized value was C=10. The option to return class likelihoods was enabled.)

It has been previously demonstrated that a straightforward approach of concatenating the color, visual texture, and geometric features into a single feature vector can yield poor classification results (Halatci et al., 2008), so a naïve Bayes fusion approach is used here. This approach assumes that color, visual texture, and geometric features are conditionally independent given the terrain class. Thus, the likelihood of a terrain patch belonging to a terrain class is the product of the class likelihoods for each sensing mode, e.g. as

$$\begin{aligned} &P(Sand \mid color, texture, geometry) \\ &\quad = P(Sand \mid color) \cdot P(Sand \mid texture) \cdot P(Sand \mid geometry). \end{aligned} \tag{3-28}$$

Note that since there may be many pixels observed in each terrain patch, the overall estimate of the class likelihood, based on the pixels' color data, is taken as the geometric mean of the class likelihoods of the individual pixels. Thus, where the SVM yields the likelihood of a terrain class for each pixel based on its color—e.g. $P(Sand \mid color(pixel_1))$—the color-based class likelihood is calculated as

$$\begin{aligned} P(Sand \mid color) &= P(Sand \mid color(pixel_1), ..., color(pixel_n)) \\ &= \prod_{i=1}^{n} \left(P(Sand \mid color(pixel_i)) \right)^{1/n}. \end{aligned} \tag{3-29}$$

The same approach is used to calculate the class likelihood for visual texture:

$$\begin{aligned} P(Sand \mid texture) &= P(Sand \mid texture(pixel_1), ..., texture(pixel_n)) \\ &= \prod_{i=1}^{n} \left(P(Sand \mid texture(pixel_i)) \right)^{1/n}. \end{aligned} \tag{3-30}$$

In this supervised classification framework, hand-labeled feature vectors associated with each of the classes are used for SVM training. In the naïve Bayes fusion approach, separate SVM models are trained to classify color, visual texture, and geometry features. For this work 400 color feature vectors associated with each of the terrain classes is used to train the color SVM model. Visual texture and geometry SVM models are trained in the same manner.

3.1.3 Experiment Details

As with the local terrain classifiers, the visual terrain classifier was experimentally validated using data collected during experiments with the FSRL Technology Testbed Rover, TORTOISE, in an outdoor beach environment.

3.1.3.1 Robot Configuration

TORTOISE, shown in Figure 3-2, is an 80-cm-long, 50-cm-wide robot with four rigid aluminum wheels with grousers. The wheels on either side are connected to the main body with a differential, such that the pitch angle of the main body is the average of the pitch angles of the left and right wheel pairs. A complete description of TORTOISE is presented in Appendix A.

Figure 3-2. TORTOISE, showing location of stereo camera pair

Visual terrain classification relies primarily on TORTOISE's forward-looking stereo camera pair, which is mounted on a rigid mast 90 cm above the terrain. The stereo pair is a Videre Design "dual DCAM" with a 19 cm baseline, capturing color images at 640×480 resolution (Videre Design, 2001). A sample image from the left camera of the stereo pair is shown in Figure 3-3. Range data were extracted from the stereo images using SVS (Small Vision System), Videre Design's commercial stereo processing software (Konolige, 2007).

Figure 3-3. Sample image from stereo camera

Mounted to the rover body is a two-axis tilt sensor, Crossbow CXTA02, measuring body pitch and roll. Additionally, all four wheel motors are equipped with encoders, to measure wheel angular position. Wheel odometry, body pitch, and roll are used to align stereo-generated range data with an Earth-fixed reference frame.

During experiments, the rover traveled at a speed of 3 cm/sec. Stereo images were captured every 1.5 seconds. Images and sensor outputs were stored during experiments and processed offline.

3.1.3.2 Experiment Environment

Experiments were performed at Wingaersheek Beach, in Gloucester, MA. The beach, which is largely composed of sand, has both small, loose rocks and large outcrops. This site was chosen due to its similarity in appearance to the MER landing sites on Mars. As with the local terrain classification, three distinct terrain classes were considered for visual terrain classification: sand, beach grass, and rock. These terrain classes are identified in Figure 3-4. To the rover, sand appears as a uniform gray flat

surface, rock appears tan and orange with some steep slopes and fine uniform texture, and beach grass appears highly textured with mixed browns and dark shadows.

Figure 3-4. TORTOISE on Wingaersheek Beach, showing terrain classes

Six experimental data sets were collected over the course of three days. Each data set consisted of a time series of stereo images and other sensor data recorded during a straight-line traverse of at least 10 meters over a combination of two or three terrains. No two paths were identical. During the experiments lighting conditions ranged from diffuse lighting from an overcast sky to harsh point lighting from low, direct sunlight. In all, 1646 image pairs were collected along with corresponding internal sensor data.

3.1.3.3 Data Processing

The stored data collected during the experiments was post-processed offline. Every 20th image pair was hand-labeled to identify the ground-truth terrain class corresponding to each pixel. For each of these labeled image pairs, range data was also

calculated. By combining the labels with the range data, ground-truth terrain classes were identified for each 20-cm by 20-cm terrain cell. For each of the six data sets, between 10 and 27 image pairs were hand labeled. The first two or three image pairs from each data set were used for training the classifiers, with the remaining images used for testing. Note that separate classifiers were trained and tested for each data set.

3.1.4 Results

The accuracy of the visual terrain classifier was assessed for each of the data sets described in 3.1.3. Figure 3-5 shows the receiver operating characteristic (ROC) curves for a representative data set. Here the horizontal axis indicates the false positive percentage (%FP) and the vertical axis indicates the true positive percentage (%TP). Each terrain forms a curve on the plot as the threshold for leaving terrain "unclassified" is adjusted. The end point of the curves represents the case in which none of the terrain is left unclassified. Any combination of points on these curves can be achieved through proper selection of the threshold. Note that the scale of the x-axis is magnified to allow the curves to be easily seen.

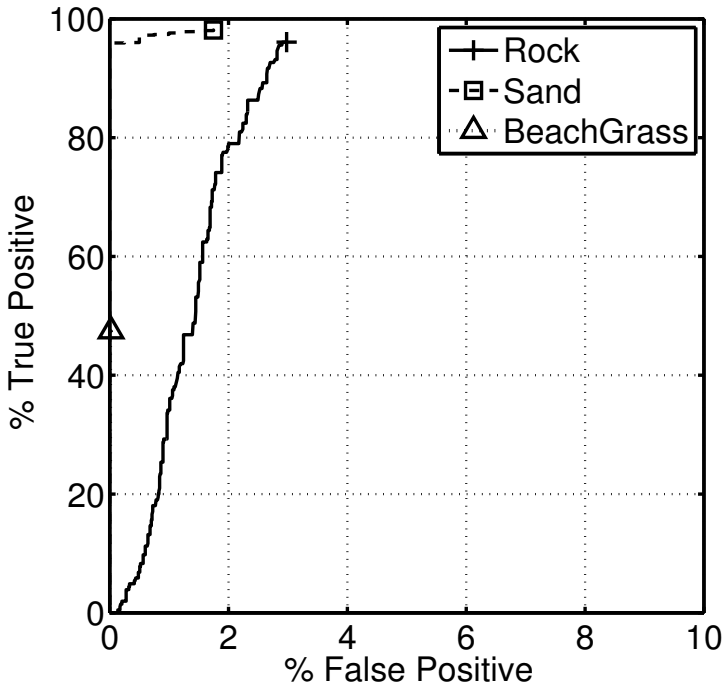

Figure 3-5. Representative ROC curves for visual terrain classifier

In this plot it can be seen that the manually trained classifier performed very well at identifying both sand and beach grass. More than 95% of the sand was correctly identified before any of the other terrains was falsely identified as sand. For beach grass, nearly 50% was correctly identified with less than 0.1% of the other terrains falsely identified. Results for rock were also very good, with 96% of the rock correctly identified and less than 3% of the other terrains falsely identified as rock.

Numerical results also indicate robust performance of the visual classifier across all six data sets, as shown in Table 3-1. The top two rows show statistics of the true positive percentage of the classifiers when no data is left unlabeled, corresponding to the vertical coordinate of the ROC curve endpoints. The third and fourth rows show statistics of the false positive percentage, corresponding to the horizontal coordinate of the ROC curve endpoints. The bottom two rows show statistics related to the ratio between the true

positive percentage and the false positive percentage. The metric, %TP/(%TP + %FP), is closely related to the fraction of labeled patches which are labeled correctly. The values in brackets indicate a 95% confidence interval for the statistic.

TABLE 3-1. PERFORMANCE OF VISUAL TERRAIN CLASSIFIER

Mean % True Positive	95.1% [93.1% - 97.1%]
St. Dev. of % True Positive	1.9% [1.2% - 4.7%]
Mean % False Positive	4.9% [2.9% - 6.9%]
St. Dev. of % False Positive	1.9% [1.2% - 4.7%]
Mean %TP/(%TP + %FP)	0.95 [0.93 - 0.97]
St. Dev. of %TP/(%TP + %FP)	0.02 [0.01 - 0.05]

In this table, it can be seen that on average more than 95% of each terrain class was correctly identified, with only 5% being falsely identified when all of the terrain patches were assigned a class. It should be noted, however, that the true positive rate and false positive rate tend to increase and decrease together, as more or less of the terrain is assigned a given class label. The metric presented in the bottom two rows is intended to measure the accuracy while being insensitive to that variation. Here it can be seen that on average, 95% of terrain classified as a given terrain class actually belongs to that class, even when no terrain is left unclassified. This result shows that accurate visual classification can be accomplished using an SVM classifier with the proposed features in a natural outdoor environment. These visual classification results will be used for comparison in 5.1.4 to assess the performance of the self-supervised classification framework.

3.1.5 Conclusions

Section 1.1 has presented a method for classifying terrain based on visual features. In this approach, a supervised framework is used to classify terrain based on color, visual texture, and geometry, with the multiple sensory modes combined using naïve Bayes fusion.

This approach was applied to experimental data collected with a four-wheeled rover in an outdoor beach environment. Classification accuracy was assessed by comparing the classifier results to hand-labeled ground truth data. These results demonstrate that this visual classification approach can be used to accurately classify natural outdoor terrain in real-world conditions.

This visual terrain classifier is appropriate for use in scenarios in which labeled examples of all terrain classes are available for training. As described in the introduction to this chapter, it can also be used as a component of a more general vision system, capable of classifying terrain in the presence of unexpected terrain classes. The results presented in this section are also useful as a baseline for comparison to the self-supervised classification results presented in Chapter 5.

3.2 Visual Detection of Novel Terrain

3.2.1 Introduction

In the planetary exploration scenario, situations often occur when a robot encounters a terrain patch belonging to a class it wasn't trained to recognize. A traditional supervised visual classifier like the one described in 1.1 would assume that the terrain patch belonged to one of the known classes, then make an incorrect class prediction. For instance, if a classifier has only learned to recognize safely traversable terrain classes, it

would predict that all terrain patches are traversable, potentially jeopardizing the safety of the robot. If the novel terrain represented something of scientific interest, failure to identify it could result in a missed scientific opportunity. The purpose of the novel terrain detection algorithm is to identify terrain patches that lie outside the set of known classes and thus represent a previously unobserved class. This would allow appropriate caution or interest to be taken by the rover.

The goal of a novel terrain detection algorithm is to distinguish between terrain patches belonging to a set of a priori known terrain classes and terrain patches belonging to an unknown "novel" class. This section presents an approach for detection of novel terrain using color stereo imagery. It employs the same color, visual texture, and range-derived geometric data features described in 1.1 as features for classification.

The innovation of this approach is the use of a two-class classifier for novelty detection. While novelty detection algorithms have been developed for scenarios in which the only available training data is associated with the known classes, this approach is intended for scenarios in which an additional set of unlabeled data is also available for training. In the planetary exploration scenario, terrain patches associated with the known terrain classes may be identified autonomously using the proprioceptive terrain classification techniques described in Chapter 2. This approach takes advantage of the availability of unlabeled visual data[11] to improve the accuracy of novel terrain detection. The use of unlabeled data was inspired by the work of (El-Yaniv & Nisenson, 2007) on optimal single-class classification strategies. Because no hand-labeling of visual data is

[11] Here, unlabeled visual data can be visual data associated with any terrain patch that hasn't been autonomously classified using other sensors. If proprioceptive sensors are used for this autonomous classification, then visual data of terrain patches not sensed proprioceptively are unlabeled.

required, this approach is appropriate for detection of novel terrain without a human in the loop.

Section 3.1.2 describes the two-class classification approach to novelty detection, as well as two baseline approaches which will be used for performance comparison. Section 3.2.3 gives details about the experiments conducted to analyze the performance of the proposed approach, and section 3.2.4 presents the results of those experiments. Section 3.2.5 presents conclusions and suggests directions for future research.

3.2.2 Approach

As described in the introduction, the goal of novel terrain detection is to distinguish between terrain patches belonging to a set of a priori known terrain classes and terrain patches belonging to an unknown "novel" class. This problem is distinct from traditional two-class classification problems because labeled examples of the novel class do not exist. Previously proposed approaches to novelty detection, such as those based on a one-class SVM (Schölkopf, 2000) or distribution modeling (Bishop, 1995), are trained using only labeled examples of known terrain classes. In the scenario considered here, however, it is assumed that information is available about both the a priori known classes and a "world" class, which is a mixture of both known and unknown classes. This situation arises when only a subset of the terrain patches observed by the robot are associated with known terrain classes.

For example, this occurs when terrain is labeled as "known" only after the robot has come into physical contact with it, or when it is labeled based on exteroceptive sensor

data[12] available for only a small fraction of the observed terrain. The two-class classification approach presented here uses a SVM classifier trained to distinguish known classes from the world class, thereby implicitly identifying the novel class. For comparison, baseline approaches based on a one-class SVM and a distribution model are also presented in section 3.2.2.3.

3.2.2.1 Theoretical Justification

Justification for the proposed approach to novelty detection is based on a comparison of an optimal novelty detector and an optimal two-class classifier in the scenario when the probability density functions of all classes are known. This analysis shows that the novelty detector and a two-class classifier can identify the same regions associated with the novel and known classes.

In the following analysis, it is assumed that the world class, W, represents a mixture of all of the terrains in the environment. W is composed of two disjoint classes: A (known terrain), and B (novel terrain). Any patch of terrain will belong to A or B, but not both. In this hypothetical scenario, it is assumed that the probability density functions associated with A and B are known. Here $p(\mathbf{x}|A)$ and $p(\mathbf{x}|B)$ represent the probability density of a feature vector $\mathbf{x}$ occurring given that it is associated with terrain class A or B, respectively.

In this scenario, the goal of novelty detection is to identify the region of the feature space containing the largest fraction of B, while containing only a specified fraction (r) of A, ideally zero. Thus, the novelty detection problem is posed as

[12] The thermal emission spectrometer carried by the Mars Exploration Rovers represents one such exteroceptive sensor, since each observation represents only a 20 mrad field of view (20 cm at a range of 10 m).

$$\mathbf{S}_{ND}{}^{*} = \arg\max_{\mathbf{S}} \int_{\mathbf{S}} \mathrm{p}(\mathbf{x}|B)d\mathbf{x} \text{ s.t. } \int_{\mathbf{S}} \mathrm{p}(\mathbf{x}|A)d\mathbf{x} = r \quad , \tag{3-31}$$

where $\mathbf{S}$ is a region of the feature space, and $\mathbf{S}_{ND}{}^{*}$ is the region of the feature space identified as novel. Note that r is the rate of false positives—instances when known terrain is incorrectly identified as novel. In principle r can be set to zero, but if there exists some $\mathbf{x}$ where both $\mathrm{p}(\mathbf{x}|A)>0$ and $\mathrm{p}(\mathbf{x}|B)>0$, increasing r will have the benefit of increasing the detection rate of novel terrain, which may be desirable. The solution to the novelty detection problem is

$$\mathbf{S}_{ND}{}^{*} = \left\{\mathbf{x} : \mathrm{p}(\mathbf{x}|A) \le t\,\mathrm{p}(\mathbf{x}|B)\right\}, \tag{3-32}$$

where t is found such that

$$\int_{\mathbf{S}_{ND}{}^{*}} \mathrm{p}(\mathbf{x}|A)d\mathbf{x} = r. \tag{3-33}$$

Here t is a monotonic function of r. This solution can be understood intuitively by contradiction. If there is some region outside $\mathbf{S}_{ND}{}^{*}$ where $\mathrm{p}(\mathbf{x} \mid A) < t\,\mathrm{p}(\mathbf{x} \mid B)$, then the fraction of B in $\mathbf{S}_{ND}{}^{*}$ could be increased by changing $\mathbf{S}_{ND}{}^{*}$. $\mathbf{S}_{ND}{}^{*}$ is unique as long as there is no region of measure greater than zero where $\mathrm{p}(\mathbf{x} \mid A) = t\,\mathrm{p}(\mathbf{x} \mid B)$.

In practice, there is no way to explicitly estimate the distribution of the novel class, so $\mathrm{p}(\mathbf{x}|B)$ cannot be used directly. Instead, we assume that it is possible to estimate $\mathrm{p}(\mathbf{x}|W)$, the probability density of the world class, which is given as

$$\mathrm{p}(\mathbf{x}|W) = \alpha\,\mathrm{p}(\mathbf{x}|A) + (1-\alpha)\,\mathrm{p}(\mathbf{x}|B). \tag{3-34}$$

Here α is unknown, representing the fraction of A in W (i.e., the fraction of the rover's environment made up of known terrain). Using $\mathrm{p}(\mathbf{x}|W)$, the A vs. W two-class classification problem can be written as

$$\mathbf{S}_W^* = \arg\min_{\mathbf{S}} \left[c_A \int_{\mathbf{S}} \mathrm{p}(\mathbf{x}|A) d\mathbf{x} + c_W \left(1 - \int_{\mathbf{S}} \mathrm{p}(\mathbf{x}|W) d\mathbf{x} \right) \right] , \tag{3-35}$$

where the region $\mathbf{S}_W^*$ is the region of the feature space classified as the world class. Here c_A is the cost of misclassifying A as W, and c_W is the cost of misclassifying W as A. Equation (3-35) is the problem that traditional two class classifiers attempt to solve without explicit definitions of p($\mathbf{x}|A$) and p($\mathbf{x}|W$). The solution to this two-class classification problem in terms of p($\mathbf{x}|A$) and p($\mathbf{x}|W$) is

$$\mathbf{S}_W^* = \left\{ \mathbf{x} : \mathrm{p}(\mathbf{x}|A) \le \frac{c_W}{c_A} \mathrm{p}(\mathbf{x}|W) \right\}. \tag{3-36}$$

Written in terms of p($\mathbf{x}|A$) and p($\mathbf{x}|B$), this becomes

$$\mathbf{S}_W^* = \left\{ \mathbf{x} : \mathrm{p}(\mathbf{x}|A) \le \frac{c_W (1-\alpha)}{c_A - \alpha c_w} \mathrm{p}(\mathbf{x}|B) \right\}. \tag{3-37}$$

Thus it can be seen that $\mathbf{S}_{ND}^*$ and $\mathbf{S}_W^*$ are both defined as regions where p($\mathbf{x}|A$) is less than some factor multiplied by p($\mathbf{x}|B$). Without knowledge of α or p($\mathbf{x}|B$), c_A and c_W can be found from (3-36) such that

$$\int_{\mathbf{S}_W^*} \mathrm{p}(\mathbf{x}|A) d\mathbf{x} = r \quad . \tag{3-38}$$

With these values of c_A and c_W, $\mathbf{S}_{ND}^*$ and $\mathbf{S}_W^*$ are identical. Thus, it follows that a two-class classifier distinguishing the known class, A, from the world class, W, can be used for detection of the novel class, B.

3.2.2.2 Detailed Approach

The proposed two-class classification approach employs a support vector machine to classify terrain based on visual features. This section describes the visual features, the classification algorithm, and the training process.

3.2.2.2.1 Visual Features

The representation of the terrain color, visual texture, and geometric features is identical to that described for the visual classifier in 3.1.2.1, and their description is repeated here for completeness. These features are all extracted from color images collected using a stereo pair.

Color data is directly available from the cameras as red, green, and blue (RGB) intensities. However, the illumination intensity affects all three values in a raw RGB representation, which can lead to poor classification results. To reduce the effect of the overall illumination level, a modified hue, saturation, and value (HSV) representation of color is used as in (Sofman et al., 2006). In this approach, hue (an angle) is represented as two values—sin(hue) and cos(hue)—to eliminate the artificial discontinuity at 2π. Thus, color is represented as a 4-element vector: [sin(hue), cos(hue), saturation, value].

Visual texture is a measure of the local spatial variation in the intensity of an image. Researchers have proposed many metrics for visual texture, such as Gabor filters and local energy methods (Bouman & Liu, 1991; Reed & du Buf, 1993). The work in this thesis uses a wavelet-based approach, similar to the one demonstrated in (Espinal et al., 1998). Here, a grayscale image is decomposed with the Haar wavelet (Strang, 1993). Three scales of wavelets are used, each scale having horizontal, diagonal, and vertical wavelets, corresponding to estimating the derivative of the intensity in the horizontal, diagonal, and vertical directions at each length scale. The scales used are 2, 4, and 8 pixels. Because this process is sensitive to local changes in intensity, the magnitudes of the wavelet coefficients are then averaged over windows of 11, 9, and 7 wavelets. Thus, visual texture is represented by a 9-element vector, composed of the window-averaged

horizontal, diagonal, and vertical wavelet coefficients at each scale. The process of calculating these visual texture coefficients from an image is presented in 3.1.2.1.2.

Terrain geometry is available through stereo image processing. The raw output of a stereo processing algorithm is a cloud of range data points. Here, the points are divided into a grid of 20-cm by 20-cm terrain patches projected onto a horizontal plane. The geometric features are statistics calculated from the elevation of points associated with each terrain patch. Here, the n points associated with a given terrain patch are represented as a $n \times 3$ matrix denoting each point's position in the [forward, right, down] coordinate frame with its origin at the rover's starting position: $\{\mathbf{p}_1,\ldots,\mathbf{p}_n\}^T$. The first element of the geometric feature vector is the average slope of the terrain, defined as the angle φ between the least-squares-fit plane and the horizontal plane, in radians. The second element is the mean-squared deviation from that plane along its normal, $\sigma_{\perp}^2$. The third element is the variance in the height of the range data points, σ_z^2. The fourth element is the height difference between the highest and lowest points within the patch, r_z. Thus, the geometry of each patch is represented as a 4-element vector: [φ, $\sigma_{\perp}^2$, σ_z^2, r_z]. These features were chosen based on the work of Halatci who used a similar feature set for classification of terrain in images collected by the Mars Exploration Rovers (Halatci et al., 2008). Equations showing how these features can be calculated from the matrix of points is presented in 3.1.2.1.3.

For the two-class classification approach, the visual features associated with color, visual texture, and geometry are concatenated into a single feature vector for each pixel. This combined feature vector has 17 elements. The first four elements of the combined feature vector are the color features associated with the pixel. The next nine

elements of the combined feature vector are the texture features associated with the pixel. The last four elements of the combined feature vector are the geometry features associated with the terrain patch to which the pixel corresponds. Note that while the color and visual texture features are distinct for each pixel, the geometric feature vectors are identical for all pixels in the same terrain patch.

3.2.2.2.2 Classification Algorithm

As with the previously presented classifiers, the support vector machine was implemented using the open-source library LIBSVM (Chang & C. Lin, 2005, 2008). For novelty detection, a Gaussian radial basis function (RBF) kernel[13] was used, with parameters optimized by cross-validation over a subset of the images used for training. (The optimized parameters were C=1, γ=1, and $c_W / c_A = 0.05$.)

Terrain classification was performed on the same grid of 20-cm by 20-cm terrain patches used for the geometric feature extraction. Multiple pixels in an image can correspond to the same terrain patch, and the concatenated color-texture-geometry feature vector associated with each pixel is classified separately by the support vector machine. The classification result for a patch is calculated by a majority vote of the individual pixel classification results. Thus, for each pixel (i, j) associated with a patch P, the support vector machine yields a predicted terrain class $C_{i,j}$, and the terrain class C_P associated with terrain patch P, is calculated as

$$C_P = \arg\max_{C} \sum_{(i,j) \text{ in } P} isequal\left(C, C_{i,j}\right). \tag{3-39}$$

[13] The radial basis function kernel and other kernels are described in detail in Appendix D.

3.2.2.2.3 Classifier Training

Training of the two-class classifier requires two sets of data: one set which represents terrain of known classes, and one set of unlabeled data which represents terrain of all (known and unknown) classes. Four hundred pixels are used to represent the known class for training, and two thousand pixels are used to represent the world class for training. The feature vectors associated with these pixels are used to train the two-class SVM. These values (400 known pixels and 2000 world pixels) were selected to balance the competing requirements of computation cost and classification accuracy.[14]

3.2.2.3 Baseline Approaches

To assess the performance of the proposed two-class classification approach to detection of novel terrain, it was compared to two existing approaches: one-class SVM and mixture-of-Gaussians distribution modeling.

3.2.2.3.1 One-Class SVM Approach

The one-class SVM, described in (Schölkopf et al., 2001), is a classification framework designed to segment a feature space into "same" and "different" classes. While a traditional two-class SVM operates by finding the hyperplane with the largest margin separating two classes in a Hilbert space, the one-class SVM operates by finding the hyperplane with the largest margin separating the "same" class from the origin in that Hilbert space.

As with the proposed two-class SVM novelty detector, the one-class SVM was implemented using LIBSVM. Again, a Gaussian RBF kernel was used. Parameters of the

[14] Analysis of the performance of the proposed novelty detection approach with more or fewer training points suggested that further increasing the number of training points might increase the accuracy of novelty detection, though this would increase the computational cost.

SVM and its kernel were optimized by cross-validation over a subset of the training images. The optimized parameters were ν=0.2 and γ=1.

The one-class SVM used the same concatenated feature vector as the two-class SVM. As above, 400 pixels belonging to the known class were used to represent the known class for training purposes. The one-class SVM used no training data from the world class. Classification of terrain patches was implemented using a majority vote of the pixel classification results.

3.2.2.3.2 Distribution Modeling

Another approach to novelty detection is based on distribution modeling, which is implemented here using a mixture of Gaussians (MoG) model. This approach attempts to model the underlying probability density function of the known class. To classify a new feature vector as known or novel, the probability density function is evaluated and compared to a constant threshold value. If the probability density is above the threshold, the feature vector is classified as known. Otherwise the feature vector is classified as novel. It should be noted that this is equivalent to assuming that the world class is uniformly distributed in the feature space. (Following the notation of 3.2.2.1, $p(\mathbf{x}|W)$ is assumed to be independent of $\mathbf{x}$.)

Here, a mixture of Gaussians model was implemented and the number of Gaussian modes was optimized by cross-validation over a subset of the training images. Training was done using the expectation maximization (EM) procedure (Bilmes, 1998; Bishop, 1995).

The approach to combine color, texture, and geometric features within the MoG model differs somewhat from the other models because the MoG model has the potential

to over-fit Gaussian modes in a high-dimensional feature space.[15] To avoid overfitting, separate MoG models were created—one for color, one for visual texture, and one for terrain geometry—and these three models were combined using the naïve Bayes assumption that feature vectors from the three sensing modes were conditionally independent given the terrain class. Four hundred feature vectors from the known class were used for training each of the MoG models.

Terrain classification was performed by combining the probability density estimates from each of the MoG models. The color-derived probability density for a patch was calculated as the geometric mean of the color MoG probability densities for the image pixels associated with the terrain patch. Thus, the color MoG model yielded a probability density for each pixel, e.g. $P(Known \mid color(pixel_1))$, and the combined color probability density estimate $P(Known \mid color(pixel_1), \ldots, color(pixel_n))$ was calculated as

$$\begin{aligned} P(Known \mid color) &= P(Known \mid color(pixel_1),...,color(pixel_n)) \\ &= \prod_{i=1}^{n} \left(P(Known \mid color(pixel_i))\right)^{1/n}. \end{aligned} \tag{3-40}$$

The texture-derived probability density was calculated the same way, e.g.

$$\begin{aligned} P(Known \mid texture) &= P(Known \mid texture(pixel_1),...,texture(pixel_n)) \\ &= \prod_{i=1}^{n} \left(P(Known \mid texture(pixel_i))\right)^{1/n}. \end{aligned} \tag{3-41}$$

Each patch had only a single geometry feature vector. The overall probability density of a patch was calculated as the product of the three sensing mode probability densities—color, visual texture, and geometry—as

[15] Because the number of covariance coefficients increases with the square of the dimension of the feature space, the amount of training data required also increases as the square of the dimension of the feature space. Thus, training one 9-dimensional MoG model requires three times the training data as three 3-dimensional MoG models.

$$P(Known \mid color, texture, geometry) = P(Known \mid color) \cdot P(Known \mid texture) \cdot P(Known \mid geometry). \quad (3\text{-}42)$$

The novelty of a patch was then determined by comparing the overall probability density to a threshold.

3.2.3 Experiment Details

The three approaches for detection of novel terrain were compared using experimental data collected with the TORTOISE rover on Wingaersheek Beach. This section will describe only the details of those experiments that were used to assess the novelty detection algorithms. Full specifications for TORTOISE are presented in Appendix A. Details about the experimental environment are presented in Appendix B.

3.2.3.1 Robot Configuration

The novel terrain detection experiments rely primarily on TORTOISE's forward-looking mast-mounted stereo camera pair, and its body-mounted two-axis tilt sensor. The stereo pair has a 19-cm stereo baseline, and captures color images at a resolution of 640×480. Range data is extracted from the stereo images using the SVS (Small Vision System) commercial stereo processing software. Range data are corrected for camera pitch and roll based on tilt sensor readings.

During experiments, the rover traveled at a speed of 3 cm/sec. Stereo images were captured every 1.5 seconds. Images and other sensor outputs were stored during experiments and processed offline.

3.2.3.2 Experimental Environment

Experiments were performed at Wingaersheek Beach in Gloucester, MA. In this environment, the three terrain classes are sand, rock, and beach grass. Visually, the sand appears as a uniform gray flat surface, rock appears tan and orange with some steep slopes and fine uniform texture, and beach grass appears highly textured with mixed brown and dark shadows.

Six experimental data sets were collected, each during a rover traverse of at least 10 meters along a straight-line path containing a combination of two or three terrains. No two paths were identical. In all, 1646 image pairs were collected. During the experiments lighting conditions ranged from overcast conditions with diffuse light to cloudless conditions with low, direct sunlight.

3.2.3.3 Data Processing

Data sets collected during the experiments were post-processed offline. In each of the data sets, every fifth image pair was passed to the stereo processing software for range data extraction. Every fourth image pair with range data was hand-labeled to identify a ground-truth terrain class for each pixel. This spacing was chosen to reduce the effect of repeated training and testing on similar images of the same terrain patch. Labeled examples of data corresponding to the known (e.g. sand and beach grass, or sand and rock) classes were drawn from the first three hand-labeled images in a data set. Unlabeled examples, corresponding to the "world" class, were drawn from the first 10 (labeled and unlabeled) images in a data set for which the range data had been calculated. Performance of the novel terrain detectors was assessed based on the remaining hand-labeled images in a data set. In total, 75 hand-labeled images were used for testing.

3.2.4 Results

The performance of the two-class classification approach was compared to that of the baseline approaches for each test set. Figure 3-6 shows the ROC curve of the results for each approach across all of the data sets. For this figure, the rock class was used as the novel class.[16] Thus, the labeled training data was drawn only from the sand and beach grass classes. Here the vertical axis indicates the percentage of true novel detection (%TN) (i.e., the fraction of rock terrain patches which were correctly identified as novel), and the horizontal axis indicates the percentage of false novel detection (%FN) (i.e., the fraction of sand or beach grass terrain patches which were incorrectly identified as novel). Each detection approach forms a curve on the plot, since both %TN and %FN are functions of the novelty detection threshold. Note that random assignment of terrain as novel would tend to yield a diagonal line from (0,0) to (100,100). Better performance is indicated by proximity of a curve to the upper-left corner of the plot.

[16] In the Wingaersheek Beach data sets all three terrain classes were known a priori. To simulate the presence of novel terrain, terrain patches corresponding to one of the classes—in this case, the rock class—were intentionally removed from the set of labeled training examples.

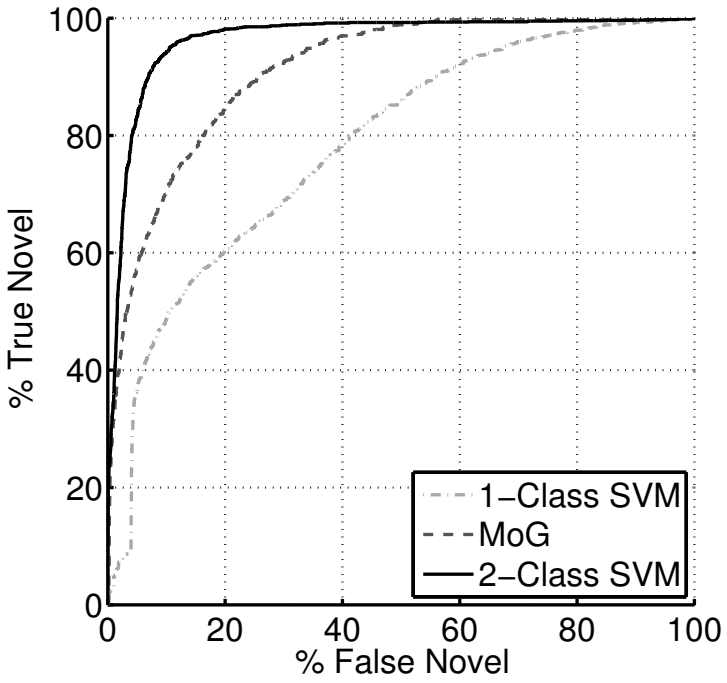

Figure 3-6. ROC curves for baseline approaches and two-class classification approach for all data sets with rock as novel class

It can be seen that the two-class classification approach demonstrated higher accuracy than the baseline approaches, particularly when a low false novel rate is required. Of the baseline approaches, higher accuracy was demonstrated by the MoG distribution modeling approach. This difference is particularly significant in the detection of novel terrain with less than 10% false novel detection, where the two-class classifier detected 94% of the novel terrain, and the one-class SVM detected less than 50%.

To summarize the performance of the novelty detectors, several performance metrics can be used. Here, each of the curves is represented by a single point displaying the best classifier performance, and %TN and %FN values are compared at that point. For this work, each curve is summarized by the point that maximizes the difference between %TN and %FN. At this point, the baseline one-class SVM detected 56% of novel terrain while misidentifying 15%, and the baseline MoG distribution modeling

approach detected 87% while misidentifying 22%. The two-class classification approach performed significantly better, detecting 95% of the novel terrain while misidentifying only 11%.

Another metric for comparison of the ROC curves is the area under the curve, referred to as P(A) (Simpson & Fitter, 1973). The one-class SVM performed significantly better than random chance, with a P(A) of 78.3%. (Random assignment to classes will yield a P(A) of 50%.) The other novelty detectors performed better still. The MoG approach demonstrated a P(A) of 91.2%, while the two-class classification approach performed slightly better, with a P(A) of 96.6%.

Similar results were observed using beach grass as the novel class, as shown in Figure 3-7. Use of sand as the novel class yielded significantly deteriorated performance, because very little training data was available from the known class.

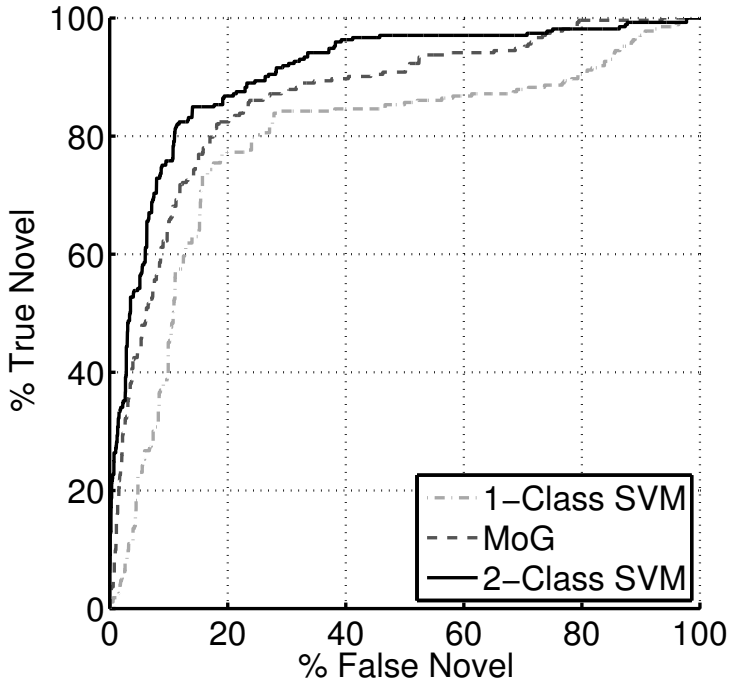

Figure 3-7. ROC curves for baseline approaches and two-class classification approach for all data sets with beach grass as novel class

A numerical summary of the performance of the three algorithms for detection of novel terrain over all data sets is shown in Table 3-2. Mean and standard deviation are compared for each of the three metrics: % True Novel and % False Novel at the point representing the best classifier performance, and P(A). Note that these statistics were compiled across all six data sets using rock and beach grass, separately, as the novel terrain class. The numbers in brackets indicate the 95% confidence interval of the statistic.

TABLE 3-2. COMPARISON OF NOVEL TERRAIN DETECTION APPROACHES

	One-Class SVM	MoG Distribution Modeling	Two-Class SVM
Mean % True Novel	91.0% [83.1% - 98.9%]	85.1% [72.9% - 97.4%]	88.7% [80.0% - 97.4%]
St. Dev. of % True Novel	11.0% [7.6% - 20.2%]	17.1% [11.8% – 31.3%]	12.2% [8.4% – 22.3%]
Mean % False Novel	35.1% [11.5% - 58.7%]	20.2% [9.8% - 30.5%]	15.2% [6.8% - 23.6%]
St. Dev. of % False Novel	33.0% [22.7% - 60.2%]	14.5% [10.0% – 26.4%]	11.7% [8.0% – 21.3%]
Mean P(A)	73.9% [55.9% – 92.0%]	83.6% [71.5% - 95.7%]	87.1% [77.5% – 96.8%]
St. Dev. P(A)	25.3% [17.4% – 46.1%]	16.9% [11.6% – 30.9%]	13.5% [9.3% – 24.7%]

For each of these metrics, the two-class classification approach outperformed the baseline mixture of Gaussians approach, though not by a significant margin for any metric individually. The two-class classification approach outperformed the one-class SVM in both the false novel detection rate and the area under the ROC curve, both by significant margins, while the difference in the true novel detection rate was not significant. These results suggest that the two-class approach demonstrates more accurate and robust novel terrain detection than either of the baseline approaches.

Computation time for classification using the two-class approach on a desktop computer ranged from 12-70 seconds for a 640×480 image. Computation time varied based on the complexity of the boundary between the known and novel classes (as measured by the number of support vectors), and the fraction of the image with valid range data.

3.2.5 Conclusions

This section has presented a two-class classification approach to novel terrain detection. This approach uses samples of visual data from unlabeled images to represent the world class for use in training a novel terrain detection algorithm. A theoretical analysis showed the fundamental similarities between two-class classification and novelty detection. Using experimental data from the TORTOISE rover on Wingaersheek Beach, the two-class classification approach was compared to two baseline approaches for novelty detection which use only data from known terrain classes during training. The results suggests that the two-class classification approach achieves a higher accuracy than the baseline approaches while reducing variability between data sets.

3.2.5.1 Future work

For a robot in rough terrain, the computational cost of novel terrain detection can be significant, with the current approach taking 12-70 seconds per image on a modern desktop computer. Computation time could likely be reduced by an order of magnitude or more by replacing the Gaussian kernel of the SVM with a polynomial kernel. Mathematical details of optimizing a SVM for use with a polynomial kernel are presented in Appendix D.

Additionally, this two-class classification approach to novelty detection is not restricted to the use of a SVM classification algorithm. Other two-class classification algorithms, including those based on regularized least squares regression or Bayesian logistic regression, may be used in the place of the SVM. Further experimental studies would be necessary to determine whether one classification algorithm performs significantly better than any other when used for novelty detection.

Chapter

4

Mechanical Terrain Characterization

The purpose of mechanical terrain characterization is to identify mechanical properties associated with a particular terrain class from proprioceptive sensor data. In this thesis, the mechanical properties of interest are measurable quantities that describe the forces and torques acting between a rover wheel and the terrain. The mechanical terrain characterization approach presented in this chapter establishes minimum and maximum bounds on the net traction force available at a given terrain patch based on observed rover wheel torque and sinkage when wheel slip is induced.

4.1 Introduction

Understanding the physical interaction between a planetary rover and the terrain it is traversing is critical to predicting whether that terrain can be traversed safely. Some types of terrain (e.g. loosely packed sand) are treacherous to traverse on even shallow slopes, as significant wheel sinkage may occur, leading to high motion resistance and rover entrapment. Other terrain types (e.g., textured rock) present a solid footing on which a rover might safely climb steep slopes. The purpose of mechanical terrain characterization is to measure mechanical terrain properties that can be used to determine whether a terrain patch may be safely traversed. This chapter is focused on the

characterization of deformable terrain under a rigid wheel, a scenario in which excessive wheel slip could result in the wheel becoming trapped.

Previous researchers have taken various approaches to characterizing deformable terrain. Bekker, Wong, and Reece developed parametric models for normal and shear stress on wheels in deformable terrain that can be used to calculate the net forces and torques on wheels (Bekker, 1969; Wong, 2001; Wong & Reece, 1967). In their models, terrain is characterized by eight parameters. Measuring these parameters requires dedicated equipment to apply normal and shear forces and measure the corresponding displacements. Iagnemma developed an approach to measure the parameters of a reduced-order Bekker model without dedicated terrain sensing equipment, by measuring wheel torque and sinkage during a rover traverse (Iagnemma et al., 2002; Iagnemma et al., 2004). Kang extended that work and proposed a nondimensionalized metric based on drawbar pull—the drag force that would be required to hold the vehicle stationary—as a traversability metric (Iagnemma et al., 2003; Kang, 2003). This metric, the drawbar pull divided by the vertical load, represents the available net traction force as a fraction of the weight on a wheel. Analyzing simulations over a variety of terrains Kang found an approximate equation for drawbar pull as a function of wheel sinkage, wheel torque and vertical load. However, while Kang's predictions of drawbar pull accurately approximate the predictions of the Bekker model when averaged over many terrains, he provided no guarantees about the error of any single drawbar pull prediction.

In the field of planetary exploration, overly optimistic predictions related to the traversability of terrain can lead to catastrophic failure. This chapter presents a novel, optimization-based method for predicting strict upper and lower bounds on Kang's

traversability metric for a terrain patch, such that if the terrain model assumptions are correct, the traversability metric is guaranteed to fall between the bounds. By providing bounds on the traversability metric, this approach serves as a method for characterizing terrain traversability in potentially high-risk scenarios.

4.2 Approach

The terrain characterization approach proposed here attempts to find upper and lower bounds on Kang's nondimensionalized drawbar pull traversability metric for a given patch of terrain, without requiring that drawbar pull be measured directly. This is accomplished by using constrained optimization to combine a terrain model with observed wheel-terrain interaction measurements, specifically wheel torque and sinkage. Section 4.2.1 describes the nondimensionalized drawbar pull measure which is used as the traversability metric, section 4.2.2 describes the specific attributes of terrain interaction being sensed, section 4.2.3 describes the wheel-terrain interaction models, and section 4.2.4 describes the optimization method as it applies to each model.

4.2.1 Traversability Metric

The traversability metric used here for terrain characterization is the nondimensionalized drawbar pull, DP/W, which is a measure of the net available traction force between the wheel and the terrain. The net traction force can be modeled via lumped forces acting on a single, rigid wheel, as shown in Figure 4-1. In this figure, the wheel is traveling from left to right and rotating clockwise. Forces and torques on the axle are shown, assuming the wheel to be in equilibrium. Here, W is the vertical load on the wheel (including its own weight), T is the torque exerted on the wheel by a drive

motor, *DP* is the drawbar pull, and *z* is the wheel sinkage. Clearly, if the drawbar pull is positive, the wheel can exert a force to move the rover in the desired direction of travel. Conversely, if the drawbar pull is negative, resistance on the wheel will slow the rover, possibly causing the rover to become immobilized.

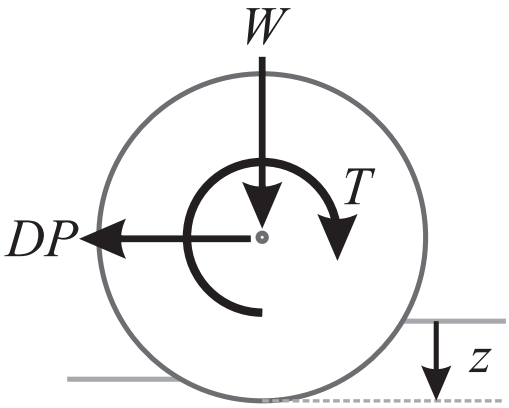

Figure 4-1. Wheel forces, torque, and sinkage

The nondimensionalized drawbar pull is calculated by dividing the drawbar pull by the vertical load on the wheel. This value, *DP/W*, is related to the load a rover can tow relative to its own weight, as illustrated in Figure 4-2(a), or the maximum slope up which a rover can move, as illustrated in Figure 4-2(b). Neglecting redistribution of vertical loads on the wheels, the effect of slope on stresses within the terrain[17], and changes in *DP/W* with the normal force (i.e. nonlinear wheel-terrain interaction effects), the wheel can travel up a slope of angle $\alpha = \text{atan}(DP/W)$.

[17] On steep slopes large internal stresses may exist to support the weight of the terrain higher up the slope. This will reduce the net traction force available to move the rover.

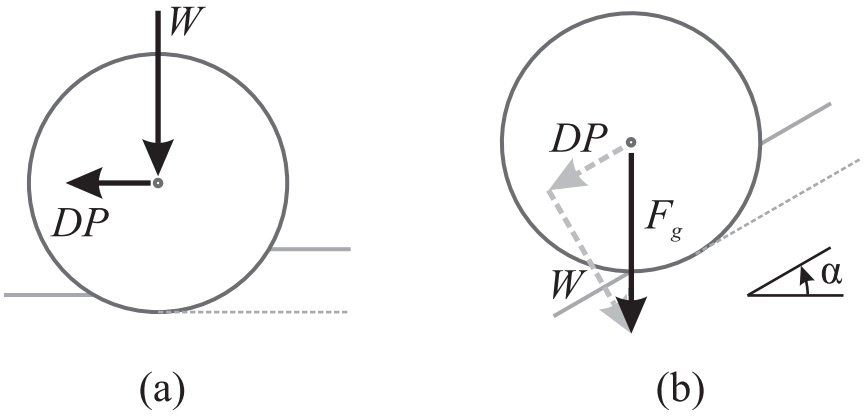

Figure 4-2. Wheel forces on flat terrain (a) and slopes (b)

It is important to note that the drawbar pull is a function of both the mechanical properties of terrain being traversed and the wheel slip ratio, *i*, which is defined as

$$i = 1 - \frac{v_x}{\omega r}, \tag{4-1}$$

where v_x is the forward velocity of the wheel, ω is the angular velocity, and r is the wheel radius. The relationship between drawbar pull and the wheel slip ratio is illustrated in Figure 4-3, which shows the experimentally observed relationships for four of the terrains studied later in this chapter. Since the traversability metric is a function of drawbar pull, the value of wheel slip must be specified for the traversability metric to be measured on a given terrain. Here, the drawbar pull is measured with a wheel slip ratio between 0.4 and 0.7, conditions under which the drawbar pull is relatively insensitive to changes in slip for most terrains.

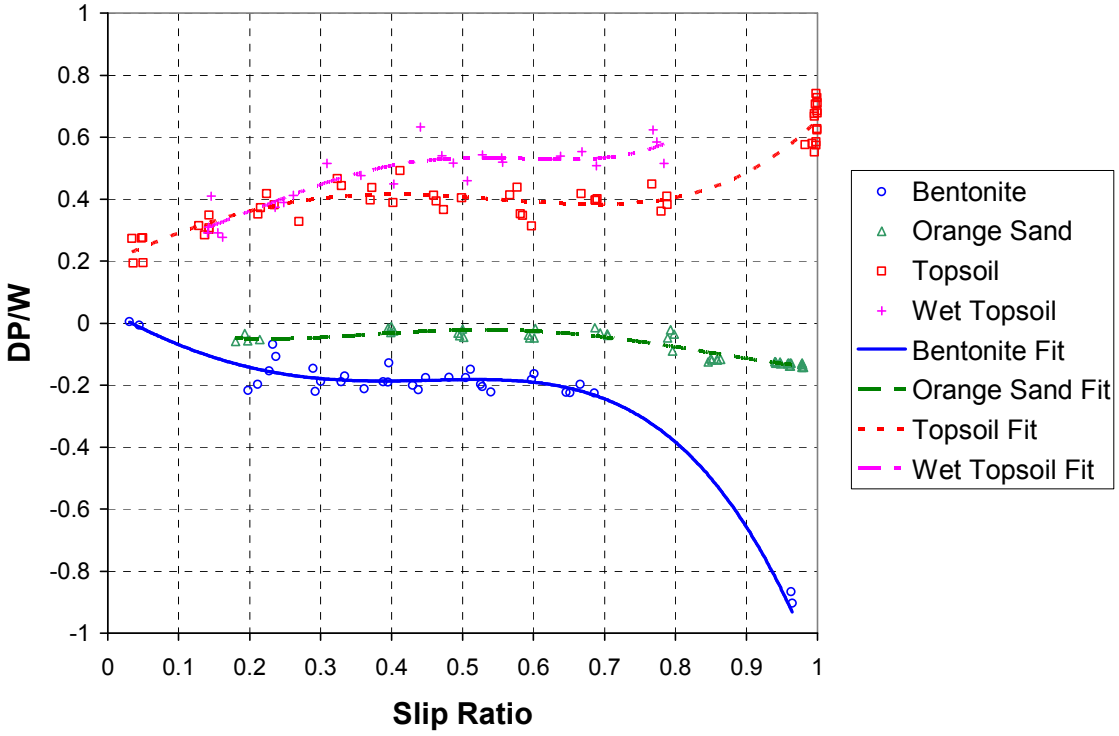

Figure 4-3. Nondimensionalized drawbar pull (DP/W) as a function of slip for four terrains (experimental data points and best fit curves)

By specifying the wheel slip to be a moderate value—neither very low where some easily traversable terrains exhibit small drawbar pull, nor very high where material transport around the wheel can affect drawbar pull—this approach ensures that the traversability metric provides a conservative estimate of the force that a wheel could apply to stop itself from sliding down a slope, or to drive up a slope.[18]

4.2.2 Terrain Sensing

While drawbar pull could potentially be directly measured using a dedicated force sensor mounted on a rover suspension element or wheel mount, such a sensor has not been included on previous Mars rovers. In this work, it is assumed that the rover is

[18] If a rover is driving up a slope at a slip ratio less than 0.4, and the drawbar pull it can exert is not sufficient to maintain its forward progress, the slip ratio will tend to increase. Thus, at some point in the future the rover will be able to exert the drawbar pull calculated for higher-slip conditions.

equipped with a torque sensor on (at least) one driven wheel. The ability to measure wheel sinkage is also assumed.

Here two different sinkage measurement capabilities are considered: absolute and relative sinkage measurement, illustrated in Figure 4-4. Absolute sinkage measurement refers to the ability to measure the distance between the undisturbed soil surface and the lowest point on the wheel, at a single (specified) wheel slip ratio, as illustrated in Figure 4-4(a). This measurement could be attained using a camera with a view of the side of the wheel, or by a dedicated sinkage sensor (Brooks et al., 2006; Reina et al., 2006).

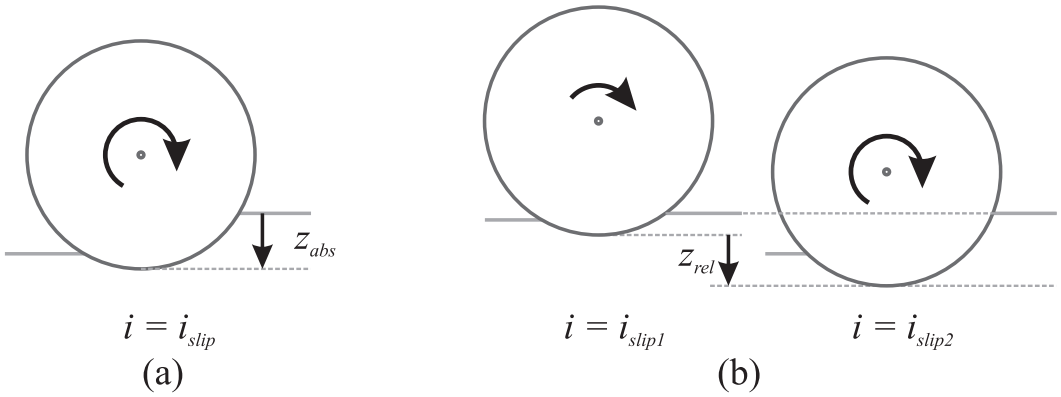

Figure 4-4. Absolute sinkage (a) vs. relative sinkage (b)

The alternative to absolute sinkage measurement is relative sinkage measurement, which is the ability to measure the difference in the vertical position of the wheel at two different slip ratios, as illustrated in Figure 4-4(b). On flat terrain, this could be accomplished using only proprioceptive sensors that measure the suspension configuration, as in (Wilcox, 1994).

Since the drawbar pull is evaluated under slip conditions, wheel torque and sinkage must be measured while the wheel is slipping. Here, wheel slip is induced by driving one wheel faster than the others, as in the behaviors presented in 2.2.2.

4.2.3 Terrain Models

A terrain model is used to relate observed wheel sinkage and torque to a predicted drawbar pull. Here two different terrain models are presented: a contact region model, which can describe most plausible interaction states with rigid or deformable terrain; and a Bekker model, which closely approximates the behavior of many real-world deformable terrains. Results for both these models will be shown in 4.4.

4.2.3.1 Contact Region Model

The contact region model described here is a highly nonrestrictive model for wheel terrain interaction. This model is depicted in Figure 4-5. Given an angle θ from the vertical, wheel terrain interaction forces are modeled as a normal stress distribution $\sigma(\theta)$ and a tangential stress distribution $\tau(\theta)$ that act within a contact region between θ_1 and θ_2. The only constraint on the stresses is that they must be non-negative—that is, the soil cannot apply tension, and the tangential stress must always oppose the net applied wheel torque.

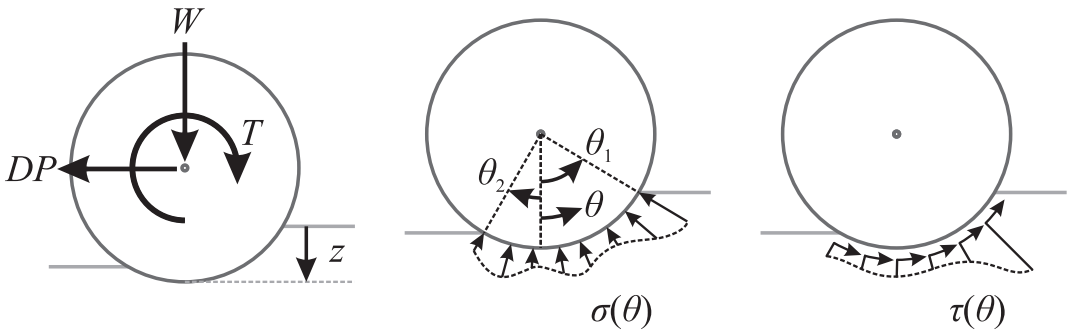

Figure 4-5. Contact Region model

To compute the net forces applied to the wheel by the terrain, these stresses are integrated over the contact region:

$$W = rb\int_{\theta_2}^{\theta_1}\sigma(\theta)\cos\theta\,d\theta + rb\int_{\theta_2}^{\theta_1}\tau(\theta)\sin\theta\,d\theta\,, \tag{4-2}$$

$$DP = rb\int_{\theta_2}^{\theta_1}\tau(\theta)\cos\theta\,d\theta - rb\int_{\theta_2}^{\theta_1}\sigma(\theta)\sin\theta\,d\theta\,, \tag{4-3}$$

$$T = r^2 b\int_{\theta_2}^{\theta_1}\tau(\theta)d\theta\,. \tag{4-4}$$

Here, r is the wheel radius and b is the wheel width. Since the wheel is assumed to be in equilibrium, W is the vertical load on the terrain, DP is the drawbar pull, and T is the torque applied by the motor. Using (4-2) and (4-3), the nondimensionalized drawbar pull DP/W can be calculated from the normal and tangential stresses.

It can be observed that this model is descriptive, rather than predictive. While a wide variety of terrain interaction phenomena can be represented as a pair of normal and tangential stress distributions within this model, knowledge of those forces and torques provides no insight as to the wheel-terrain interaction conditions at a different slip ratio or vertical load.

4.2.3.2 Bekker Model

The Bekker terrain model described here is a parameterized form of the contact region model, which sacrifices generality for predictive ability (Bekker, 1969). Developed by Bekker in the 1950s and 1960s, the Bekker model defines parametric functions for the normal stress $\sigma(\theta)$ and tangential stress $\tau(\theta)$, as shown in Figure 4-6.

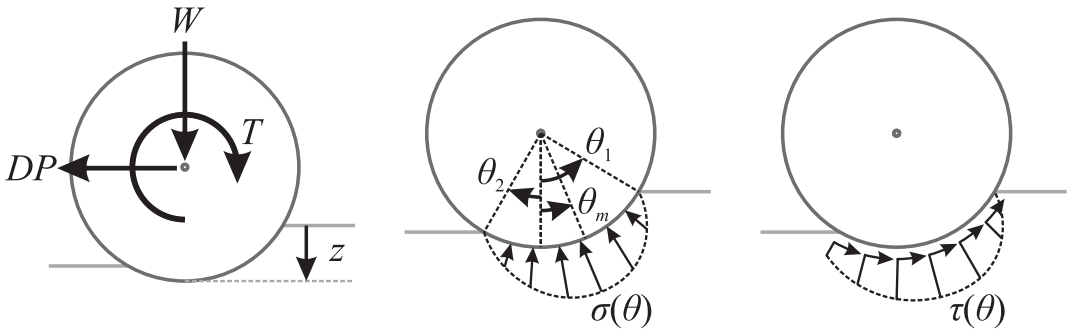

Figure 4-6. Bekker terrain model

The equation describing the normal stress function is as follows:

$$\sigma(\theta) = \left(\frac{k_c}{b} + k_\phi \right) \left(r\cos\theta^*(\theta) - r\cos\theta_1 \right)^n , \tag{4-5}$$

using

$$\theta^*(\theta) = \begin{cases} \theta & \text{for } \theta \geq \theta_m \\ \theta_1 - \dfrac{\theta_1 - \theta_m}{\theta_m - \theta_2}(\theta - \theta_2) & \text{for } \theta \leq \theta_m \end{cases} , \tag{4-6}$$

$$\theta_m = (c_1 + c_2 i)\theta_1 , \tag{4-7}$$

and the equation describing the shear stress equation is as follows:

$$\tau(\theta) = (c + \sigma(\theta)\tan\phi)\left(1 - \exp\left(\frac{-j(\theta)}{K} \right) \right), \tag{4-8}$$

using

$$j(\theta) = r(\theta_1 - \theta - (1-i)(\sin\theta_1 - \sin\theta)) . \tag{4-9}$$

where i is the slip ratio from Equation (4-1). In this representation, a terrain is characterized by the following Bekker parameters: k_c, k_φ, n, c_1, c_2, c, φ, and K, defined in Table 4-1.[19]

TABLE 4-1. BEKKER MODEL PARAMETERS

Symbol	Name	Role
k_c, k_φ	sinkage moduli	k_c and k_φ determine the magnitude of normal stress as a function of vertical soil deflection
n	sinkage exponent	n determines the rate of change of normal stress as a function of vertical soil deflection
c_1, c_2	wheel slip coefficients	c_1 and c_2 determine the location of the maximum normal stress as a function of wheel slip
c	soil cohesion	c determines the maximum shear stress which can be supported at zero normal stress
φ	angle of internal friction	φ determines the ratio between shear stress and normal stress for large normal stresses
K	shear deformation modulus	K determines the rate of change of shear stress as a function of vertical soil deflection

These parameters have been measured for a wide range of terrains. Parameters for sand, loam, and clay are found in (Wong, 2001). Estimates of the cohesion and internal friction angle of Martian soils have been measured by the Viking lander (H. J. Moore, Hutton, Scott, Spitzer, & Shorthill, 1977), Sojourner rover (Rover Team, 1997), and the Spirit rover (Arvidson et al., 2004). By using the minimum and maximum values for each parameter observed in published data, plausible ranges for each of these parameters can be defined. Table 4-2 lists the parameter ranges assumed for this Bekker model.

[19] It should be noted that while the foundations of this model were introduced by Bekker, Equation (4-7) for θ_m is due to Wong and Reece (1967). An alternative parameterization of (4-5) by Wong and Reece includes an additional factor of $b^{(1-n)}$, and replaces k_c and k_φ with $c\ k_c'$ and $\gamma_s\ k_\varphi'$.

TABLE 4-2. RANGES FOR BEKKER PARAMETERS[20]

Parameter	Minimum Value	Maximum Value	Units
$k_c/b + k_\varphi$	1000	3000	kPa/m^n
n	0.578	1.2	
c_1	0.18	0.43	
c_2	0.32	0.41	
c	0	42	kPa
φ	15	43	deg
K	0.01	0.04	m

As with the contact region model, the stresses computed from the Bekker model can be integrated using Equations (4-2), (4-3), and (4-4) to find the net forces acting on the rover wheel. Thus, given a known vertical load W, wheel slip ratio i, and the Bekker soil parameters, the nondimensionalized drawbar pull DP/W can be calculated.

4.2.4 Optimization Framework Description

An optimization framework is used to find bounds on the value of the traversability metric, DP/W, across the range of terrains described by each terrain model, given a set of experimental observations. Specifically, to find a lower bound on the traversability metric, DP/W is minimized subject to the constraints of the terrain model, experimentally observed torque T, sinkage z, slip i, and vertical load W.

Three different combinations of terrain models and wheel sinkage measurements were considered for the traversability metric bounding problem. The first approach used the contact region model and assumed knowledge of absolute wheel sinkage. This is the most general model for terrain and the optimization has a closed-form solution, but it

[20] The value for $k_c/b + k_\varphi$ is given as a single parameter, since k_c and k_φ cannot be independently identified with a single wheel width. This range assumes a wheel width of 0.051 meters, the width of the TORTOISE rover's wheels.

requires measurement of absolute wheel sinkage, which might not be possible in practical scenarios.[21]

The second approach uses a Bekker terrain model and assumes knowledge of relative wheel sinkage. This is a more restrictive model of the terrain compared to the contact region model, but it is capable of predicting behavior at different slip conditions and requires measurement of only the relative sinkage.

The third approach uses a Bekker terrain model and assumes knowledge of absolute wheel sinkage. This again uses a relatively restrictive model and requires measurement of absolute sinkage, but has the potential for prediction of tighter bounds on the traversability metric compared to the other two approaches.

The following sections describe the optimization of each of the three approaches.

4.2.4.1 Contact Region Model with Absolute Sinkage

Due to the simplicity of the contact region model, upper and lower bounds on *DP/W* can be written explicitly, assuming the absolute sinkage is known. Here the optimization problems for the lower and upper bounds are posed as

[21] Measurement of absolute sinkage can be accomplished as in (Brooks et al., 2006), but this approach requires the presence of a camera with a view of the side of the wheel, sufficient illumination, and visual contrast between the wheel rim and the terrain. Guaranteeing sufficient illumination would require the addition of a light source to the rover. Other methods of measuring absolute wheel sinkage may require additional hardware, such as laser or sonar range sensors.

$$\left(\frac{DP}{W}\right)^*_{\min} = \min_{\sigma(\cdot),\tau(\cdot)} \quad \frac{rb\int_{\theta_2}^{\theta_1}\tau(\theta)\cos\theta\,d\theta - rb\int_{\theta_2}^{\theta_1}\sigma(\theta)\sin\theta\,d\theta}{W_{measured}}$$

$$\begin{aligned} \text{subject to} \quad & \sigma(\theta) \geq 0 \quad \forall\,\theta \in [\theta_2, \theta_1] \\ & \tau(\theta) \geq 0 \quad \forall\,\theta \in [\theta_2, \theta_1] \\ & T_{measured} = r^2 b\int_{\theta_2}^{\theta_1}\tau(\theta)d\theta \\ & W_{measured} = rb\int_{\theta_2}^{\theta_1}\sigma(\theta)\cos\theta\,d\theta + rb\int_{\theta_2}^{\theta_1}\tau(\theta)\sin\theta\,d\theta \end{aligned} \tag{4-10}$$

and

$$\left(\frac{DP}{W}\right)^*_{\max} = \max_{\sigma(\cdot),\tau(\cdot)} \quad \frac{rb\int_{\theta_2}^{\theta_1}\tau(\theta)\cos\theta\,d\theta - rb\int_{\theta_2}^{\theta_1}\sigma(\theta)\sin\theta\,d\theta}{W_{measured}}$$

$$\begin{aligned} \text{subject to} \quad & \sigma(\theta) \geq 0 \quad \forall\,\theta \in [\theta_2, \theta_1] \\ & \tau(\theta) \geq 0 \quad \forall\,\theta \in [\theta_2, \theta_1] \\ & T_{measured} = r^2 b\int_{\theta_2}^{\theta_1}\tau(\theta)d\theta \\ & W_{measured} = rb\int_{\theta_2}^{\theta_1}\sigma(\theta)\cos\theta\,d\theta + rb\int_{\theta_2}^{\theta_1}\tau(\theta)\sin\theta\,d\theta. \end{aligned} \tag{4-11}$$

The explicit solutions for the lower and upper bounds are

$$\left(\frac{DP}{W}\right)^*_{\min} = \min\left\{\begin{array}{l} \frac{1}{\cos\theta_1}\left(\frac{T}{rW}\cos(\theta_1-\theta_2)-\sin\theta_1\right) \\ \frac{1}{\cos\theta_2}\left(\frac{T}{rW}\cos(\theta_1-\theta_2)-\sin\theta_2\right) \end{array}\right\}, \tag{4-12}$$

$$\left(\frac{DP}{W}\right)^*_{\max} = \max\left\{\begin{array}{l} \frac{1}{\cos\theta_1}\left(\frac{T}{rW}-\sin\theta_1\right) \\ \frac{1}{\cos\theta_2}\left(\frac{T}{rW}-\sin\theta_2\right) \end{array}\right\}. \tag{4-13}$$

These bounds correspond to situations in which the stresses are concentrated at the front and rear contact region boundaries, as shown in Figure 4-7. Thus, the stresses are zero except at the ends of the contact region, where (in theory) they are concentrated as Dirac delta functions. Figure 4-7(a) and (b) illustrate the two scenarios that could yield the lower bound presented in Equation (4-12). Figure 4-7(c) and (d) illustrate the two scenarios that could yield the upper bound presented in Equation (4-13).

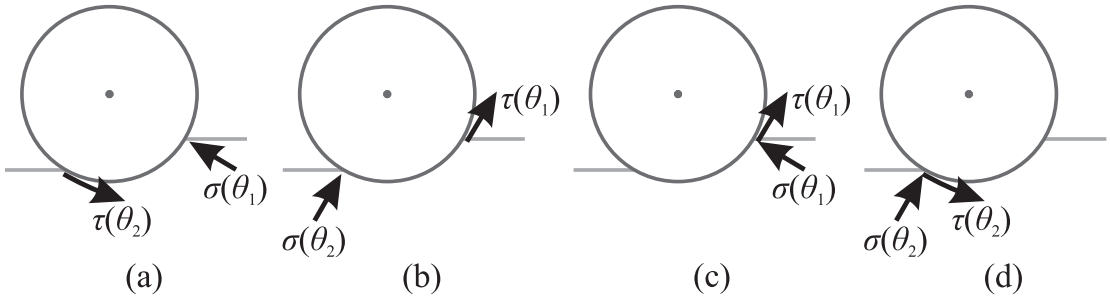

Figure 4-7. Locations of concentrated stresses for lower bound ((a) or (b)), and upper bound ((c) or (d))

Here, θ_1 is calculated from the absolute sinkage z_{abs} as

$$\theta_1 = \operatorname{acos}\left(1 - \frac{z_{abs}}{r}\right), \tag{4-14}$$

For simplicity, θ_2 is assumed to be equal to $-\theta_1$, implying that soil does not build up behind the wheel to a height higher than the undisturbed soil surface. In steady state, this means that disturbed soil (behind the wheel) is at least as dense as undisturbed soil (in front of the wheel). Given this assumption, the bounds can be simplified to

$$\left(\frac{DP}{W}\right)^*_{\min} = \frac{1}{\cos\theta_1}\left(\frac{T}{rW}\cos(2\theta_1) - \sin\theta_1\right), \tag{4-15}$$

$$\left(\frac{DP}{W}\right)^*_{\max} = \frac{1}{\cos\theta_1}\left(\frac{T}{rW} + \sin\theta_1\right). \tag{4-16}$$

4.2.4.2 Bekker Model with Relative Sinkage

The complexity of the stress functions in the Bekker model prohibit derivation of an explicit solution for *DP/W* bounds, so numerical optimization is used to find the minimum and maximum *DP/W*. Constrained optimization is implemented using sequential quadratic programming (SQP) using the Matlab `fmincon` function (Mathworks, 2005). Specifically, *DP/W* as calculated using Equations (4-2) and (4-3) is minimized (or maximized) over the parameters defined in Table 4-3. The optimization problem to find the lower bound is posed as the following minimization:

$$\left(\frac{DP}{W}\right)^{*}_{\min} = \min_{\substack{(k_c/b+k_\varphi),n,c_1,c_2,c,\tan\varphi,\\ K,\theta_{1,slip1},\theta_{1,slip2},\theta_{2,slip1},\theta_{2,slip2}}} \frac{rb\int_{\theta_{2,slip2}}^{\theta_{1,slip2}}\tau_{slip2}(\theta)\cos\theta\,d\theta - rb\int_{\theta_{2,slip2}}^{\theta_{1,slip2}}\sigma_{slip2}(\theta)\sin\theta\,d\theta}{W_{slip2}}$$

subject to Equality Constraints

$$T_{slip1} = r^2 b\int_{\theta_{2,slip1}}^{\theta_{1,slip1}}\tau_{slip1}(\theta)d\theta$$

$$T_{slip2} = r^2 b\int_{\theta_{2,slip2}}^{\theta_{1,slip2}}\tau_{slip2}(\theta)d\theta$$

$$z_{rel} = r\left(\cos\theta_{1,slip1} - \cos\theta_{1,slip2}\right)$$

$$W_{slip1} = rb\int_{\theta_{2,slip1}}^{\theta_{1,slip1}}\sigma_{slip1}(\theta)\cos\theta\,d\theta + rb\int_{\theta_{2,slip1}}^{\theta_{1,slip1}}\tau_{slip1}(\theta)\sin\theta\,d\theta$$

$$W_{slip2} = rb\int_{\theta_{2,slip2}}^{\theta_{1,slip2}}\sigma_{slip2}(\theta)\cos\theta\,d\theta + rb\int_{\theta_{2,slip2}}^{\theta_{1,slip2}}\tau_{slip2}(\theta)\sin\theta\,d\theta \quad (4\text{-}17)$$

Inequality Constraints

$$1000\ \text{kPa/m}^n \le (k_c/b + k_\varphi) \le 3000\ \text{kPa/m}^n$$

$$0.578 \le n \le 1.2$$

$$0.18 \le c_1 \le 0.43$$

$$0.32 \le c_2 \le 0.41$$

$$0\ \text{kPa} \le c \le 42\ \text{kPa}$$

$$\tan 15° \le \tan\varphi \le \tan 43°$$

$$0.01\ \text{m} \le K \le 0.04\ \text{m}$$

$$0\ \text{rad} \le \theta_{1,slip1} \le \pi/2\ \text{rad}$$

$$0\ \text{rad} \le \theta_{1,slip2} \le \pi/2\ \text{rad}$$

$$-\theta_{1,slip1} \le \theta_{2,slip1} \le 0\ \text{rad}$$

$$-\theta_{1,slip2} \le \theta_{2,slip2} \le 0\ \text{rad},$$

where $\sigma_{slip1}(\theta)$ and $\sigma_{slip2}(\theta)$ are the normal stress distributions at slip ratios i_{slip1} and i_{slip2}, calculated using Equation (4-5), and $\tau_{slip1}(\theta)$ and $\tau_{slip2}(\theta)$ are the shear stress distributions at slip ratios i_{slip1} and i_{slip2}, calculated using Equation (4-8). The optimization problem to find the upper bound is a maximization with the same arguments and bounds. Here the experimentally observed wheel torque (T_{slip1} and T_{slip2}, measured at two different slip ratios, i_{slip1} and i_{slip2}), relative sinkage z_{rel} , and vertical loads W_{slip1} and W_{slip2} are enforced using equality constraints.

TABLE 4-3. OPTIMIZATION PARAMETERS FOR BEKKER MODEL WITH RELATIVE SINKAGE

Parameter	Lower Bound	Upper Bound	Units
Terrain parameters			
$k_c/b + k_\varphi$	1000	3000	kPa/m^n
n	0.578	1.2	
c_1	0.18	0.43	
c_2	0.32	0.41	
c	0	42	kPa
tan φ	tan 15°	tan 43°	
K	0.01	0.04	m
Sinkage angles			
$\theta_{1,slip1}$	0	$\pi/2$	radians
$\theta_{1,slip2}$	0	$\pi/2$	radians
$\theta_{2,slip1}$	- $\theta_{1,slip1}$	0	radians
$\theta_{2,slip2}$	- $\theta_{1,slip2}$	0	radians

Since numerical optimization routines are known to have the potential to find local minima (or maxima) rather than the desired global minima (or maxima), the optimization procedure was repeated ten times with randomly generated starting conditions. It should be noted that the optimization starting conditions must satisfy the equality constraints in Equation (4-17), so randomly generated parameters from the ranges defined in Table 4-3 underwent an initial optimization to find values satisfying the equality constraints.

4.2.4.3 Bekker Model with Absolute Sinkage

The optimization process for the Bekker model assuming knowledge of absolute sinkage differs only slightly from the process in 4.2.4.2, where knowledge of relative sinkage is assumed. Again, due to the complexity of the stress functions in the Bekker model, derivation of an explicit solution for *DP/W* bounds is not feasible, so numerical optimization is employed. Constrained optimization is implemented using sequential quadratic programming (SQP) using the Matlab `fmincon` function (Mathworks, 2005). In this optimization, *DP/W* as calculated using Equations (4-2) and (4-3) is minimized (or maximized) over the parameters defined in Table 4-4. The optimization problem to find the lower bound is posed as the following minimization:

$$\left(\frac{DP}{W}\right)^{*}_{\min} = \min_{(k_c/b+k_\varphi),n,c_1,c_2,c,\tan\varphi,K,\theta_2} \frac{rb\int_{\theta_2}^{\theta_1}\tau(\theta)\cos\theta\,d\theta - rb\int_{\theta_2}^{\theta_1}\sigma(\theta)\sin\theta\,d\theta}{W_{measured}}$$

subject to Equality Constraints

$$T_{measured} = r^2 b\int_{\theta_2}^{\theta_1}\tau(\theta)d\theta$$

$$W_{measured} = rb\int_{\theta_2}^{\theta_1}\sigma(\theta)\cos\theta\,d\theta + rb\int_{\theta_2}^{\theta_1}\tau(\theta)\sin\theta\,d\theta \qquad (4\text{-}18)$$

Inequality Constraints

$$1000\ \text{kPa/m}^n \le (k_c/b + k_\varphi) \le 3000\ \text{kPa/m}^n$$
$$0.578 \le n \le 1.2$$
$$0.18 \le c_1 \le 0.43$$
$$0.32 \le c_2 \le 0.41$$
$$0\ \text{kPa} \le c \le 42\ \text{kPa}$$
$$\tan 15° \le \tan\varphi \le \tan 43°$$
$$0.01\ \text{m} \le K \le 0.04\ \text{m}$$
$$-\theta_1 \le \theta_2 \le 0\ \text{rad},$$

where $\sigma(\theta)$ is the normal stress distribution calculated using Equation (4-5), and $\tau(\theta)$ is the shear stress distribution calculated using Equation (4-8). The optimization problem to find the upper bound is a maximization with the same arguments and bounds. Here the experimentally observed torque $T_{measured}$ and vertical load $W_{measured}$ are enforced as equality constraints in the optimization. In contrast to the relative sinkage case, when absolute sinkage z_{abs} is measured, θ_1 can be calculated directly from z_{abs}, allowing it to be removed from the set of parameters being optimized:

$$\theta_1 = \text{acos}\left(1 - \frac{z_{abs}}{r}\right). \tag{4-19}$$

TABLE 4-4. OPTIMIZATION PARAMETERS FOR BEKKER MODEL WITH ABSOLUTE SINKAGE

Parameter	Lower Bound	Upper Bound	Units
Terrain parameters			
$k_c/b + k_\varphi$	1000	3000	kPa/m^n
n	0.578	1.2	
c_1	0.18	0.43	
c_2	0.32	0.41	
c	0	42	kPa
tan φ	tan 15°	tan 43°	
K	0.01	0.04	m
Sinkage angle			
θ_2	- θ_1	0	radians

The optimization routine was repeated ten times with randomly seeded initial parameter values. As with the relative sinkage case, these parameters were run through an initial optimization phase to find a set of parameters satisfying the equality constraints, prior to the *DP/W* optimization.

4.3 Experiment Details

The mechanical terrain characterization approaches were validated using data from laboratory experiments with the FSRL wheel-terrain interaction testbed. Additional experiments with the TORTOISE rover on Wingaersheek Beach were also conducted.

4.3.1 FSRL Wheel-Terrain Interaction Testbed Experiments

Initial validation of the mechanical terrain characterization approaches was done on data collected during experiments with the FSRL wheel-terrain interaction testbed, using five distinct terrains. These experiments were conducted by Shinwoo Kang for research presented in (Kang, 2003). The analysis of the data presented here represents work completed for this thesis.

The FSRL wheel-terrain interaction testbed, shown in Figure 4-8 and described in detail in Appendix C, is an apparatus designed to measure forces on a rigid wheel driven over terrain. It consists of a driven wheel mounted on an undriven vertical axis. The wheel-axis assembly is mounted on a driven carriage, so that the wheel forward velocity and angular velocity can be controlled independently. These testbed experiments were conducted using a rigid black plastic wheel 4.8 cm wide and 20 cm in diameter. Sand is bonded to the outside of the wheel to improve traction.

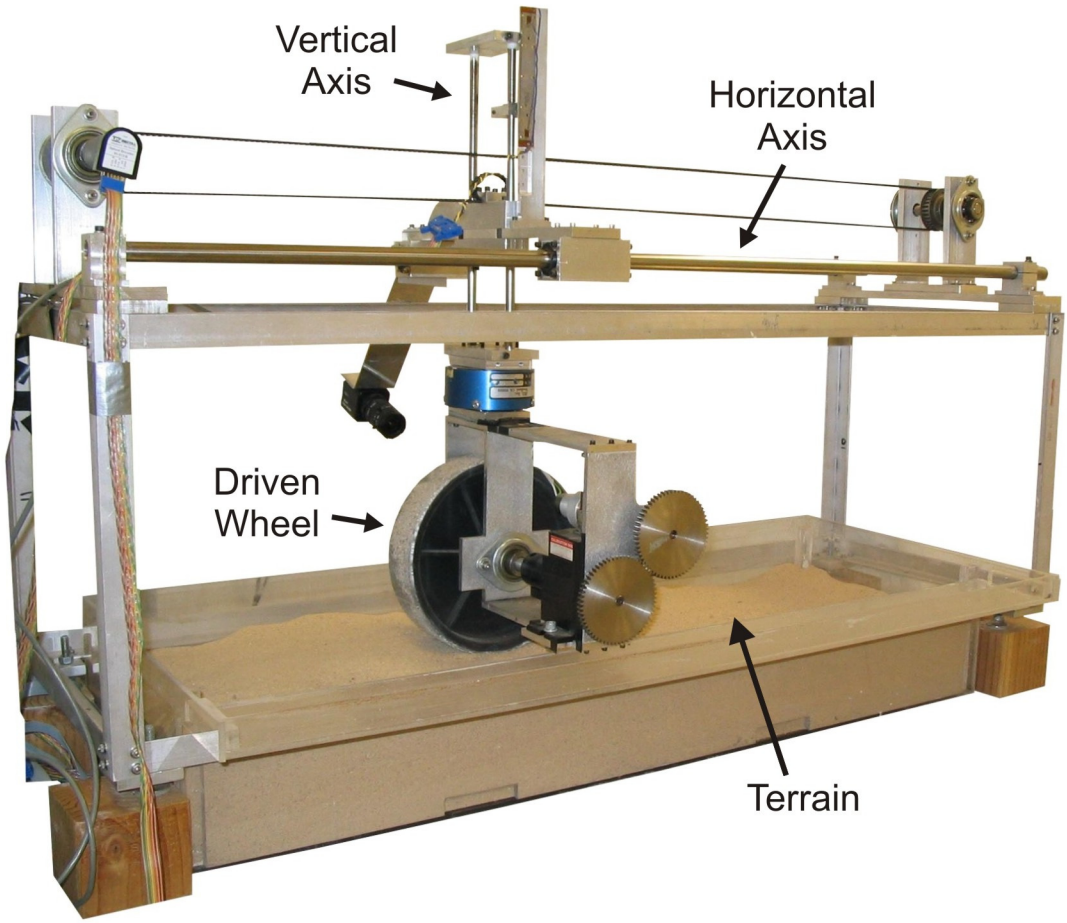

Figure 4-8. FSRL wheel-terrain interaction testbed

Under the wheel is a Plexiglas bin containing the terrain material. The bin is 90 cm long, 30 cm wide, and 15 cm deep. Five distinct terrains were used in these experiments: dry bentonite clay, modeling clay, orange sand, dry topsoil, and wet topsoil. The dry bentonite clay was a tan colored fine-grained material with the appearance of fine-grained sand. The modeling clay was a medium gray, damp, highly cohesive material that was flexible enough to be formed by hand, but rigid enough that it would maintain its shape once formed. The orange sand was fine-grained, nearly cohesionless dry sand. The topsoil was loamy black soil. In some of the experiments the soil was dry to the touch. In other experiments it was wet.

Figure 4-9 shows the sensors used for mechanical terrain characterization. Drawbar pull was measured using a six-axis force-torque sensor mounted between the wheel assembly and the vertical axis. Wheel torque was measured using a rotating torque sensor mounted between the motor and the wheel. Wheel angular velocity was measured with a tachometer attached to the wheel motor, and the horizontal position of the carriage was measured with an encoder. Sinkage was measured using a linear potentiometer mounted on the carriage, not shown in the figure. The vertical load was adjusted by attaching metal plates to the top of the vertical axis, and the total vertical load was measured between experiments using a digital scale.

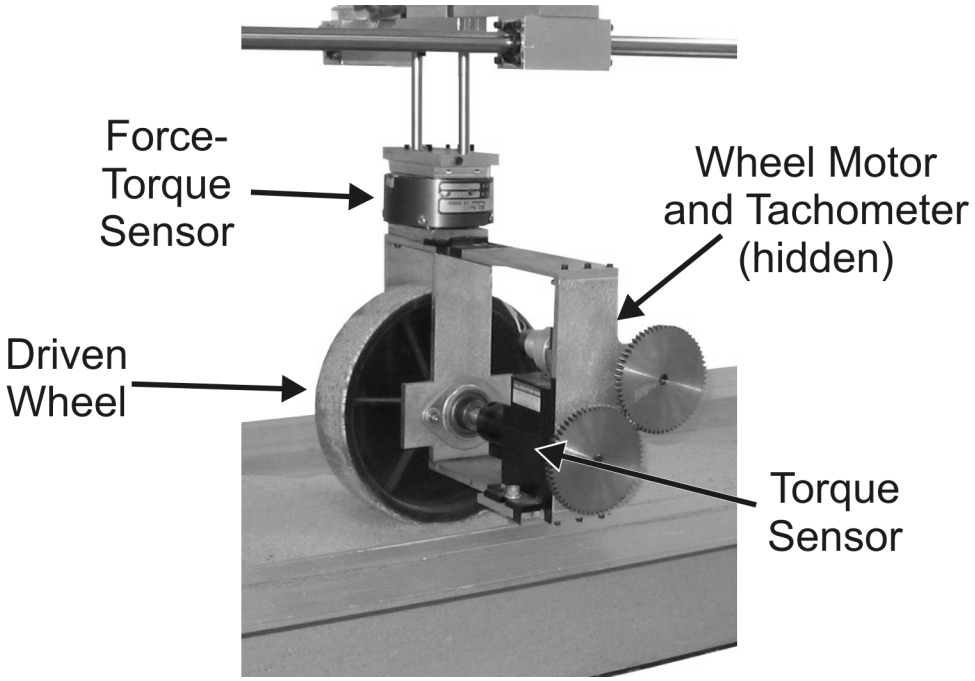

Figure 4-9. FSRL wheel-terrain interaction testbed wheel with sensors

Each test run consisted of the wheel traveling from one end of the bin to the other at a specified forward velocity and angular velocity, over a single terrain and with a fixed vertical load. Twelve combinations of terrains and vertical loads were tested: bentonite at 21.4 N; clay at 53.2 N, 68.4 N, and 83.5 N; orange sand at 53.2 N, dry topsoil at 53.2 N,

60.8 N, 68.4 N, 76.0 N, and 83.5 N; and wet topsoil at 53.2 N and 68.4 N. Each of these combinations was run at least twice for each of two slip ratios, with the higher slip ratio ranging from 0.2 to 0.5. The lower slip ratio ranged from 0.04 to 0.23.

After the experiments were completed, steady-state wheel torque and sinkage values were extracted from each run, and the median value of torque and sinkage was used in the analysis for each combination of terrain, vertical load, and wheel slip. For validation of the relative sinkage approach, z_{rel} was calculated as the difference between the sinkages observed at low slip and high slip.

4.3.2 TORTOISE Experiments on Wingaersheek Beach

Additional experiments were conducted using the four-wheeled rover, TORTOISE, in an outdoor beach environment. Both TORTOISE and Wingaersheek Beach have been described previously, so this section will address the aspects of the experiments specifically relevant to terrain characterization.

TORTOISE, shown in Figure 4-10, is robot with four rigid aluminum wheels, specifically designed for terrain sensing experiments. For the terrain characterization algorithm, TORTOISE sensed wheel torque using a torque sensor mounted to the motor driving the right front wheel, as seen in Figure 4-11. A camera mounted on the belly of the robot captured images of the right-front wheel during experiments, for use in measuring absolute wheel sinkage, and a potentiometer measured the angle between the rover body and the right wheel pair. Complete details about TORTOISE are presented in Appendix A.

Figure 4-10. Photo of TORTOISE, showing location of local sensor suite

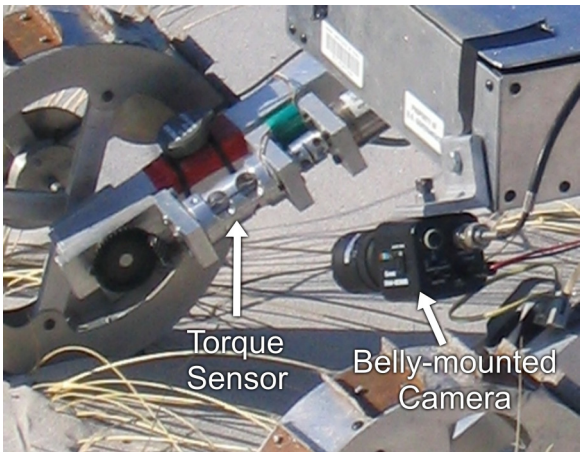

Figure 4-11. TORTOISE's local sensor suite, with torque sensor and belly-mounted camera

As described in the previous chapters, Wingaersheek Beach is an outdoor beach environment. Here, the three distinct terrain classes are sand, rock, and beach grass. The area used for experiments was below the high-tide level, so the sand was densely packed. Full details about Wingaersheek Beach are presented in Appendix B.

To induce wheel slip, the "Incremental Slip" behavior described in 2.2.2 was implemented. Here, the rover drives normally for 11 seconds, then (at t=0 seconds) starts to spin the right-front wheel faster than the other wheels. Since the rover body remains moving at the speed of the other three wheels, this causes the right-front wheel to slip relative to the terrain, at a slip ratio of 33%. At t=3 seconds, the other three wheels are slowed down, reducing the rover body speed and increasing the slip ratio to 50%. At t=6 seconds, the other three wheels are slowed down further, increasing the slip ratio to 67%. At t=9 seconds, the rover resumes normal driving. The process then repeats.

For mechanical terrain characterization, analysis was performed using wheel torque recorded during the second half of the 50% slip stage. The 50% slip stage was selected because 50% slip is close to the range of slip ratios studied on the wheel-terrain interaction testbed. The second half of the stage was used to allow the wheel sinkage and torque to reach their steady state values.

Data from a single rover traverse of 11 meters over all three terrain classes was collected. Absolute wheel sinkage was measured using the images from the belly-mounted camera by hand-labeling the wheel rim and wheel-terrain interface. Images from the belly-mounted camera were also used to identify the terrain being traversed at any instant. Wheel sinkage and torque were passed to the optimization algorithm to determine bounds on the normalized drawbar pull, DP/W. No measurement of the drawbar pull was made, so assessment of the accuracy of the bounds relies on consistency between the predicted bounds and the known terrain classes.

4.4 Results

4.4.1 FSRL Wheel-Terrain Interaction Testbed

Each of the terrain characterization approaches—contact region model with absolute sinkage, Bekker model with relative sinkage, and Bekker model with absolute sinkage—were applied to the FSRL wheel-terrain interaction testbed data, to compare the experimentally observed drawbar pull to predicted bounds for the drawbar pull.

Figure 4-12 shows the results for the contact region model with absolute sinkage measurement. In this figure, the horizontal axis indicates the terrain type and vertical load, and the vertical axis indicates the normalized drawbar pull, *DP/W*. The triangles and squares indicate the predicted upper and lower bounds predicted for the normalized drawbar pull, and the circles indicate the experimentally observed normalized drawbar pull.

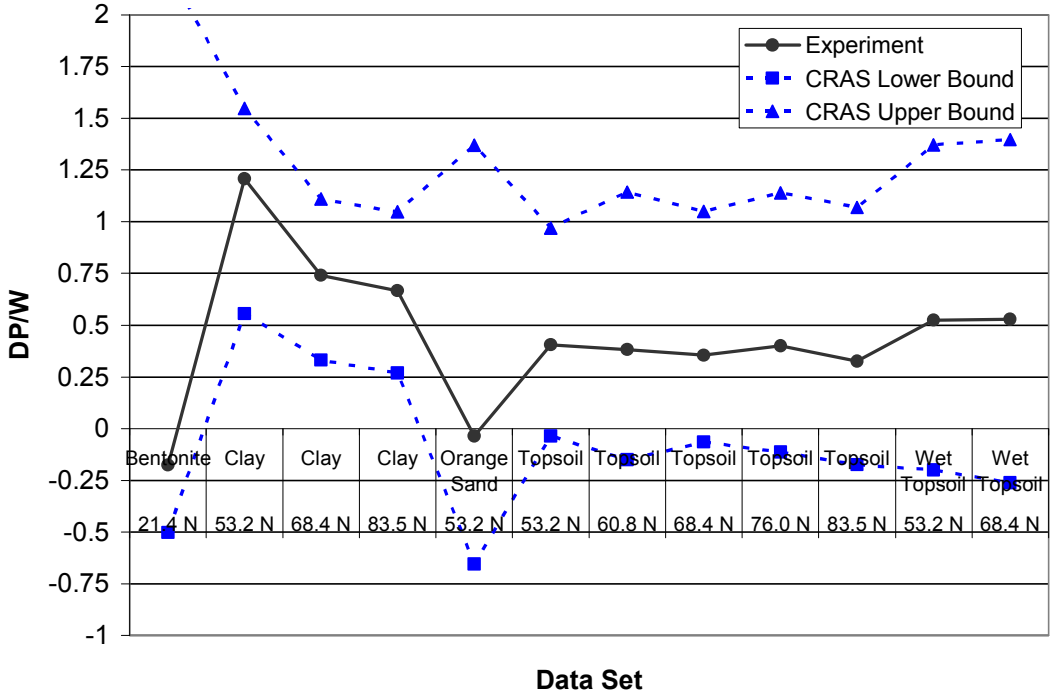

Figure 4-12. Testbed results for Contact Region Model with Absolute Sinkage (CRAS)

In this figure it can be seen that this approach is consistently correct with respect to its bounds: none of the observed drawbar pull values fall outside the predicted bounds. However these bounds are quite loose, with an average margin[22] of 0.84 between the observed value and the upper bound, and an average margin of 0.53 between the observed value and the lower bound. Thus they are likely to be marginally helpful in confidently identifying terrain that can be safely traversed. For example, although wet topsoil is relatively easy to traverse (with a measured *DP/W* of just over 0.5), the bounds cannot confidently predict that it would be at all traversable, since the predicted lower bound is less than zero.

Figure 4-13 shows results for the Bekker model with relative sinkage measured. Here the predicted bounds are significantly tighter. With this approach, the average margin between the measured value of *DP*/*W* and the upper bound was 0.10, and the average margin between the measured value and the lower bound was 0.43. In one case (clay at 53.2 N) the optimization predicted an upper bound which fell below the measured value of *DP*/*W*. However, while this small underestimation may lead the rover to underestimate the safety of traversing this terrain, a pessimistic error such as this would not put the rover in danger. In another case (bentonite at 21.4 N) the optimization algorithm was unable to find any combination of parameters that yielded the observed wheel sinkage and torque. This suggests that the model may not accurately represent the relationship between slip, sinkage, and torque in that terrain. Overall, the results are good, with tight upper bounds. While the looseness of the lower bounds is somewhat improved

[22] The average margin was calculated as the average of the absolute values of the differences between the measured *DP/W* and the bound.

over the contact region model, tighter lower bounds would improve the ability of this approach to identify safely traversable terrains.

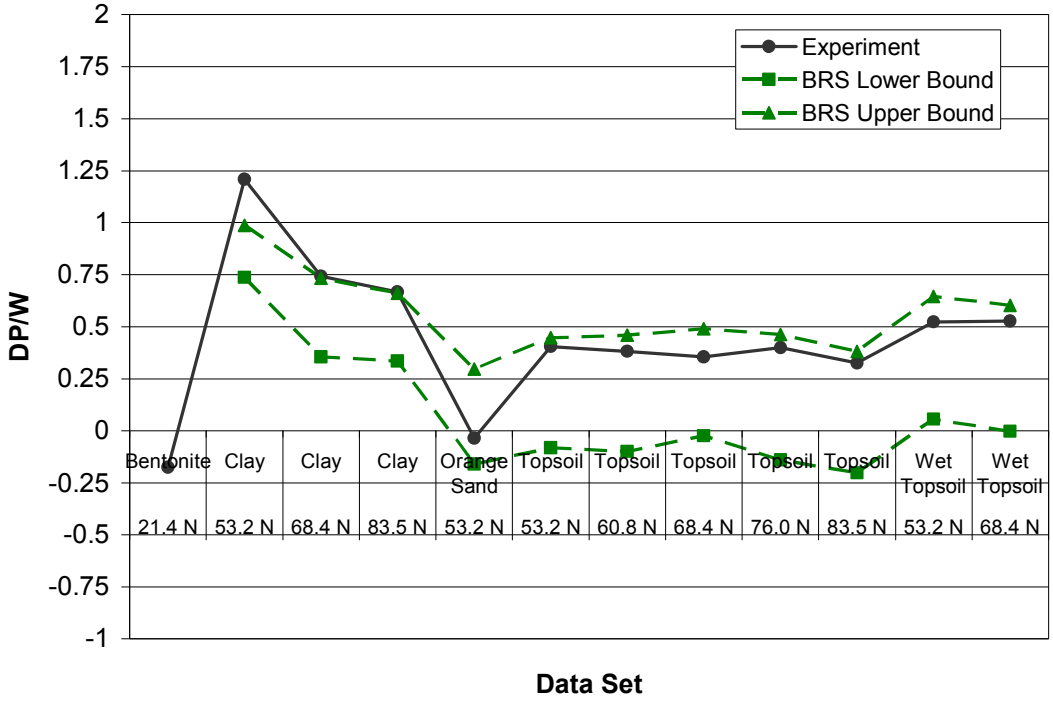

Figure 4-13. Testbed results for Bekker Model with Relative Sinkage (BRS)

Figure 4-14 shows the results for the Bekker model with absolute sinkage measured. This approach shows the tightest bounds of the three approaches, with an average margin of 0.23 between the observed *DP/W* and the upper bound, and an average margin of 0.21 between the observed *DP/W* and the lower bound. Compared to the previous approaches, the greatest improvement is in the tightness of the lower bound.

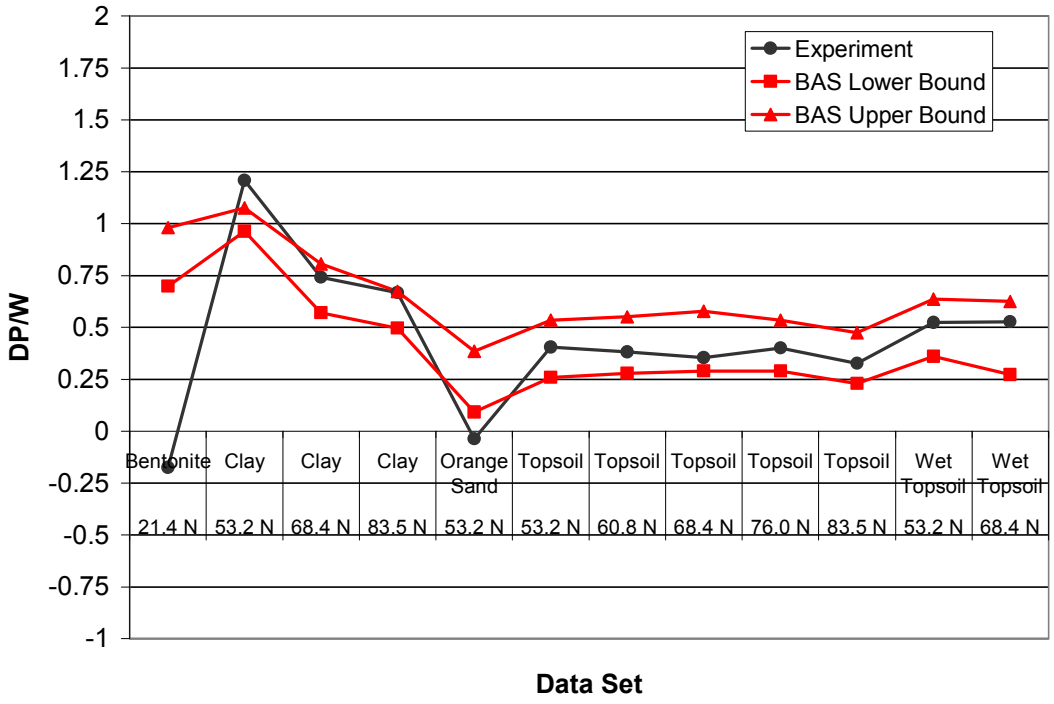

Figure 4-14. Testbed results for Bekker Model with Absolute Sinkage (BAS)

There are three cases in which the experimentally observed drawbar pull lay outside the calculated bounds. For clay at 53.2 N the upper bound on *DP/W* was too low, and for orange sand the lower bound was too high. This suggests that the model may not accurately represent the stress distributions in terrains producing very low (<0) or very high (>1) values of *DP/W*. This may be related to the range of terrains for which the Bekker parameters were previously measured,[23] and that the Bekker parameter ranges defined in Table 4-2 need to be widened to accurately model the terrains used in this experiment. Additionally, the lower bound for bentonite at 21.4 N was 0.87 higher than the experimentally observed *DP/W*. This difference is large enough to suggest errors in

[23] The ranges for the Bekker parameters defined in Table 4-2 were based on several previous works, each of which measured Bekker parameters for only a few different types of terrain. Since the terrains studied in these previous works were not originally intended to span the space of physically reasonable terrains, there may be some terrains whose Bekker parameters lie outside the ranges defined in Table 4-2.

the data collection specific to this data set, but since no errors were obvious in the data, this case was included for completeness. Without including the Bentonite data set, the average margin between the measured *DP*/*W* and both the upper and lower bounds is 0.15.

Figure 4-15 shows a comparison of all the predicted bounds, and Table 4-5 summarizes the numerical results. As described previously, the contact region model with absolute sinkage yielded the loosest bounds, while the Bekker model with absolute sinkage yielded the tightest bounds. For conservative traversability prediction, the lower bound is more important, and in this situation the Bekker model with absolute sinkage is significantly better in identifying safely traversable terrain than the other models, despite the slight overestimation of *DP/W* for orange sand.

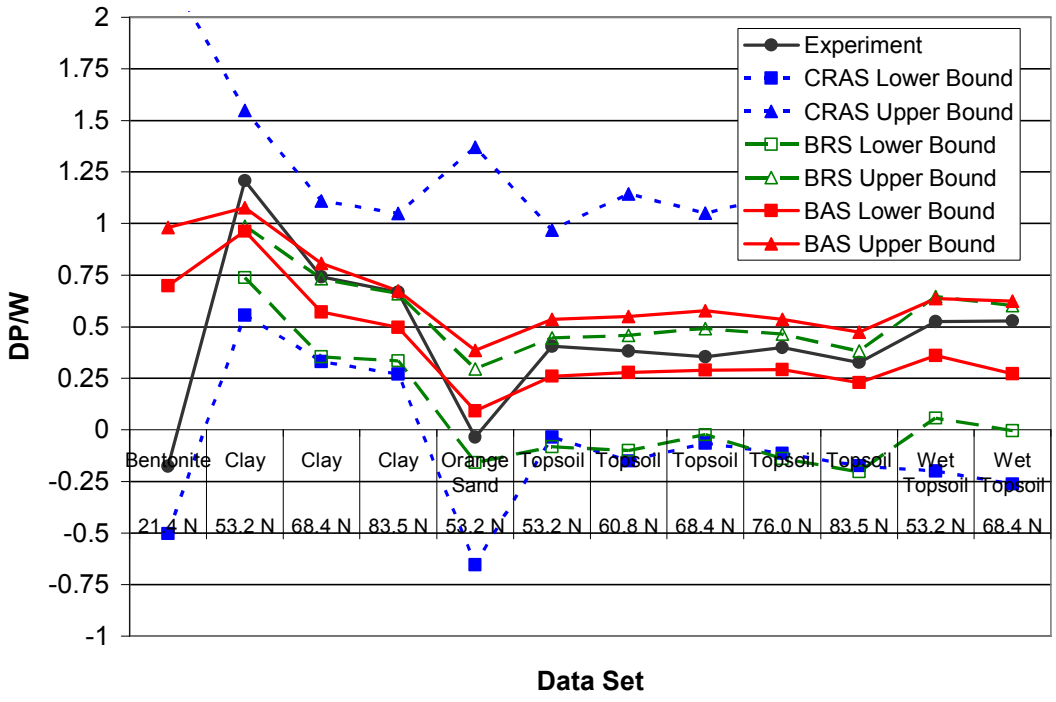

Figure 4-15. Comparison of testbed results for all approaches

TABLE 4-5. SUMMARY OF TESTBED RESULTS

Approach	Average Margin between Measured *DP/W* and Bound	
	Lower Bound	Upper Bound
Contact Region Model with Absolute Sinkage	0.53	0.84
Bekker Model with Relative Sinkage	0.43	0.10
Bekker Model with Absolute Sinkage	0.21	0.23

4.4.2 TORTOISE Rover on Wingaersheek Beach

To study the performance of the mechanical terrain characterization algorithm in an outdoor environment, the Bekker model with absolute sinkage approach was applied to data from the TORTOISE rover on Wingaersheek Beach, as shown in Figure 4-16. In this figure, the horizontal axis indicates the approximate position of the right-front wheel of the rover during the 50% spin state. The vertical axis indicates the normalized drawbar pull, *DP/W*. The shade of the background indicates the terrain being traversed, as determined by manual labeling.

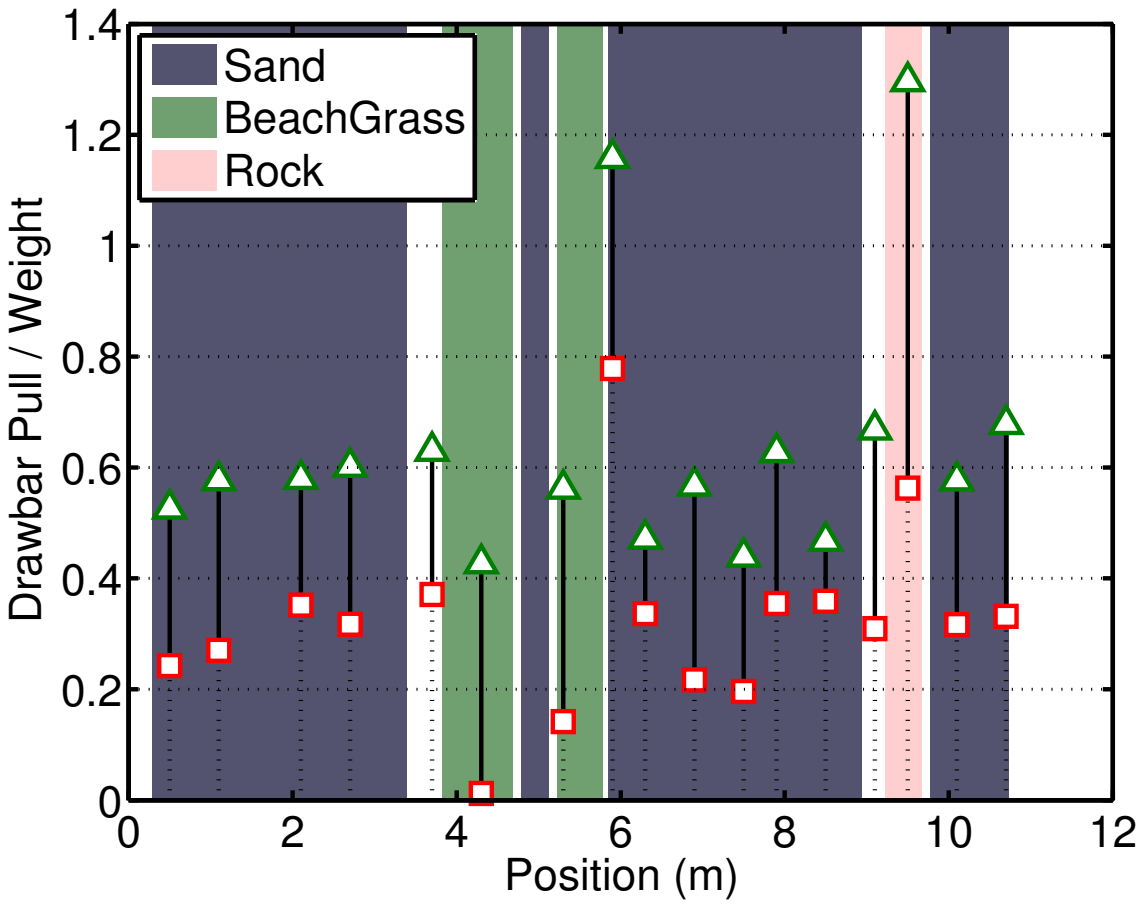

Figure 4-16. TORTOISE results for Bekker Model with Absolute Sinkage

While no ground truth for the drawbar pull measurement is available for these results, they appear to be consistent with known physical characteristics of the terrains being traversed. In this chart, the *DP/W* bounds appear to be lowest when the right-front wheel is on beach grass. This is consistent with the low available drawbar pull expected for beach grass, a highly compressible terrain that is relatively slippery. The predicted *DP/W* bounds are highest when the wheel is on rock. This result is consistent with the high available drawbar pull expected for rough, highly cohesive rock. For sand, both the *DP/W* bounds and the expected value of drawbar pull lie between those of sand and beach grass.

4.5 Conclusions

This chapter has presented an approach for evaluating terrain traversability which is appropriate for situations when a high degree of confidence is required. This approach uses an optimization framework to find upper and lower bounds on the normalized drawbar pull subject to observed wheel sinkage and torque. It uses two general terrain models, and presents three distinct model/measurement pairs. The normalized drawbar pull is guaranteed to lie between the bounds if the terrain is accurately represented by the model.

Using data from the FSRL wheel-terrain interaction testbed with five different terrains and six different vertical loads, the three methods were compared. The tightest bounds were achieved using the Bekker model with absolute sinkage, which demonstrated good consistency with experimentally observed drawbar-pull. This drawbar pull bounding method was also applied to data from a four-wheeled rover in a natural environment, and the associated drawbar pull predictions appear to be consistent with known physical characteristics of the terrains being traversed.

This technique for terrain characterization is likely to be useful in situations where a conservative estimate of wheel thrust is desired but cannot be measured directly. As a proprioceptive terrain sensing technique, it can be used for terrain clustering (by simple binning of the predicted lower bound), or it can be used as a component of a larger system, such as the self-supervised terrain classification approach presented in Chapter 5.

4.5.1.1 Future Work

Future work in the area of terrain characterization has the potential to further improve the ability of a rover to predict terrain traversability. Because the approach of

measuring relative sinkage is particularly sensitive to the relationship between sinkage and slip ratio, use of a more accurate model for slip-sinkage[24] behavior might improve the bounds for the relative sinkage measurement approach significantly. Additionally, experiments on sloped terrain would be valuable to determine how much the slope of the terrain affects the net traction force.

[24] Slip-sinkage is the mechanism by which a wheel that is slipping relative to the terrain exhibits higher sinkage than a wheel that is rolling without slip. Slip-sinkage behavior was observed in experiments by Hegedus (1963), and mathematical models were described by Bekker (1969, pp. 139-140) and by Steiner (1978).

Chapter

5

Self-Supervised Classification

In this thesis, a self-supervised classification framework is proposed which allows measurements of mechanical properties of local terrain to be generalized to yield predictions about mechanical properties of distant terrain. The self-supervised classification framework uses the algorithmic components presented in Chapters 2, 3, and 4.

This chapter presents two instantiations of the self-supervised classification framework. The first instantiation, presented in Section 1.1, uses a supervised proprioceptive terrain classifier to identify human-defined terrain classes associated with proprioceptively sensed terrain patches. Because the exteroceptive terrain classifier learns to identify terrain patches in the distance that correspond with the human-defined terrain classes, this instantiation is used to experimentally validate the self-supervised classification framework, Thus the results of exteroceptive terrain classification can be directly compared to ground truth (i.e. hand-labeled terrain classes observed in stereo camera images). However, because human supervision is required to train the proprioceptive terrain classifier, this instantiation is not appropriate for implementation in novel environments where some of the terrain classes may not be known a priori.

The second instantiation, presented in Section 1.1, is designed for scenarios in which no a priori knowledge of the terrain classes is available. In this instantiation, terrain classes are defined to correspond to ranges of a traversability metric, and thus exteroceptive terrain class predictions are used to predict the traversability of distant terrain. This instantiation is demonstrated using experimental data.

5.1 Experimental Validation of Self-Supervised Classification Framework

5.1.1 Introduction

Traditional methods for sensing non-geometric hazards, such as wheel sinkage measurement and wheel slip detection, are typically dependent on proprioceptive sensing of wheel-terrain interaction, and thus are limited to characterizing terrain patches in physical contact with the rover. This implies that a rover could not recognize a potentially hazardous situation until it has at least one wheel in contact with the hazard. To allow for predictive non-geometric hazard *avoidance*, remote detection of non-geometric hazards is needed. The self-supervised classification framework presented here provides a method for generalizing information gained from proprioceptive sensors to yield information about distant terrain.

Here, "self-supervised" refers to automatic training of the remote terrain classifier. Whereas in a traditional (i.e. manually) supervised classifier a human provides labeled training examples for each class of interest, in a self-supervised framework another classification algorithm identifies these training examples. In the context of this thesis, proprioceptive sensors are used to identify terrain patches associated with the terrain classes of interest, and visual features associated with these terrain patches are

used to train a visual classifier. This visual classifier then identifies instances of these terrain classes in a distant scene.

In the self-supervised framework presented in this section, local terrain patches are classified based on the vibration signature in the rover structure caused by wheel terrain interaction, and distant terrain patches are classified based on stereo imagery as belonging to one of the terrain classes of interest. Note that visual data used for training can be gathered either 1) from a camera with a view of the terrain under the rover wheels, or 2) from stored imagery from a camera with a view of the terrain in front of the rover. In the latter scenario, odometry-based position estimation is used to identify where the currently sensed terrain patch appears in the stored images.

To assess the performance of self-supervised classification in these two scenarios, experiments were performed using the four-wheeled TORTOISE rover in an outdoor beach environment. The accuracy of the self-supervised approach in classifying terrain was compared to that of the traditional "manually supervised" classifier presented in 1.1. Results demonstrate the viability of the self-supervised classification framework.

Section 5.1.2 describes the self-supervised classification approaches. Section 5.1.3 presents detailed information about the experiments, and Section 5.1.4 presents the results of the experiments. Section 5.1.5 presents the conclusions drawn from these results and suggests directions for future research.

5.1.2 Self-Supervised Classification Approaches

5.1.2.1 Overview

The self-supervised learning process has two stages: the training stage and the classification stage. In the training stage, the proprioceptive terrain classifier—in this instantiation a supervised vibration-based terrain classifier—identifies terrain class labels for proprioceptively sensed terrain patches, as illustrated in Figure 5-1(a). These labels, along with visual features associated with the labeled terrain patches, are used to train the visual terrain classifier. In the classification stage, illustrated in Figure 5-1(b), the visual terrain classifier is used to predict terrain classes associated with distant terrain patches.

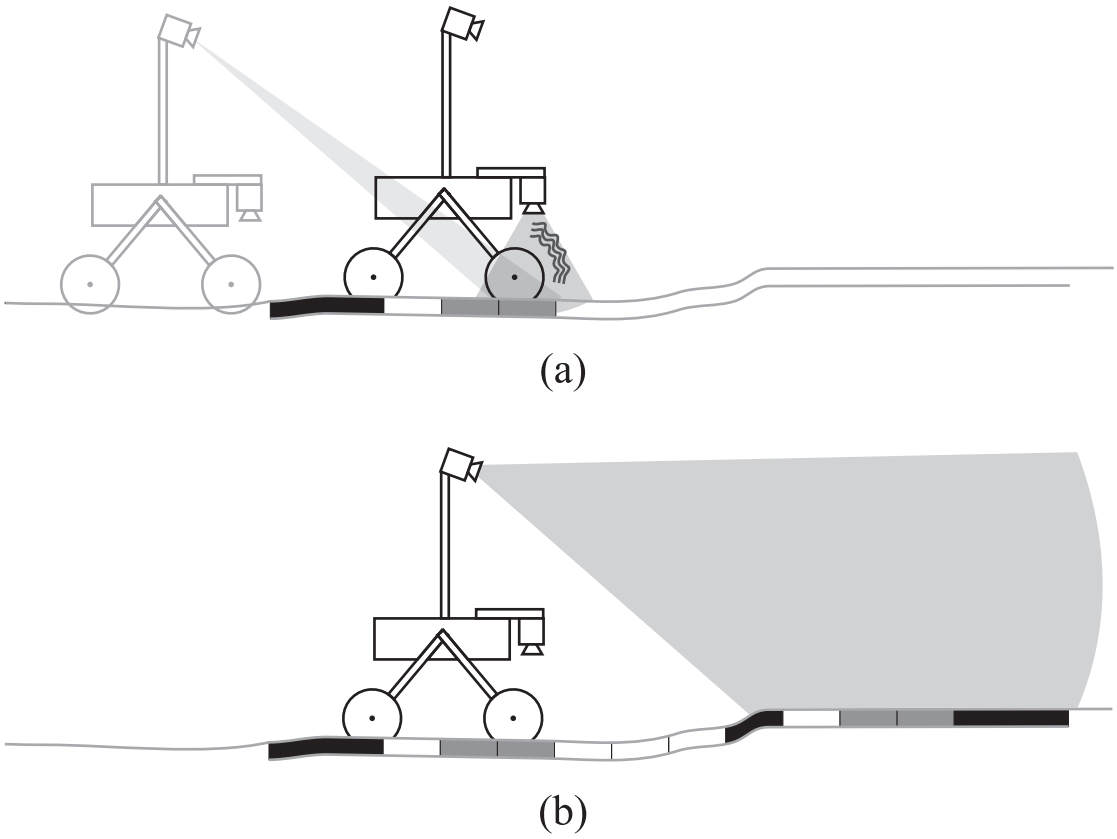

Figure 5-1. Schematic of self-supervised classification, (a) vibration-supervised training of visual classifier, (b) prediction using visual classifier

A block diagram showing the inputs and outputs of the visual classifier is presented in Figure 5-2. In the training stage, shown in Figure 5-2(a), the visual classifier takes as inputs (1) terrain class labels identified by the vibration-based terrain classifier, and (2) visual features associated with the labeled terrain patches. In the classification stage, shown in Figure 5-2(b) the visual classifier takes visual features as inputs, and outputs the terrain class associated with the observed terrain patches.

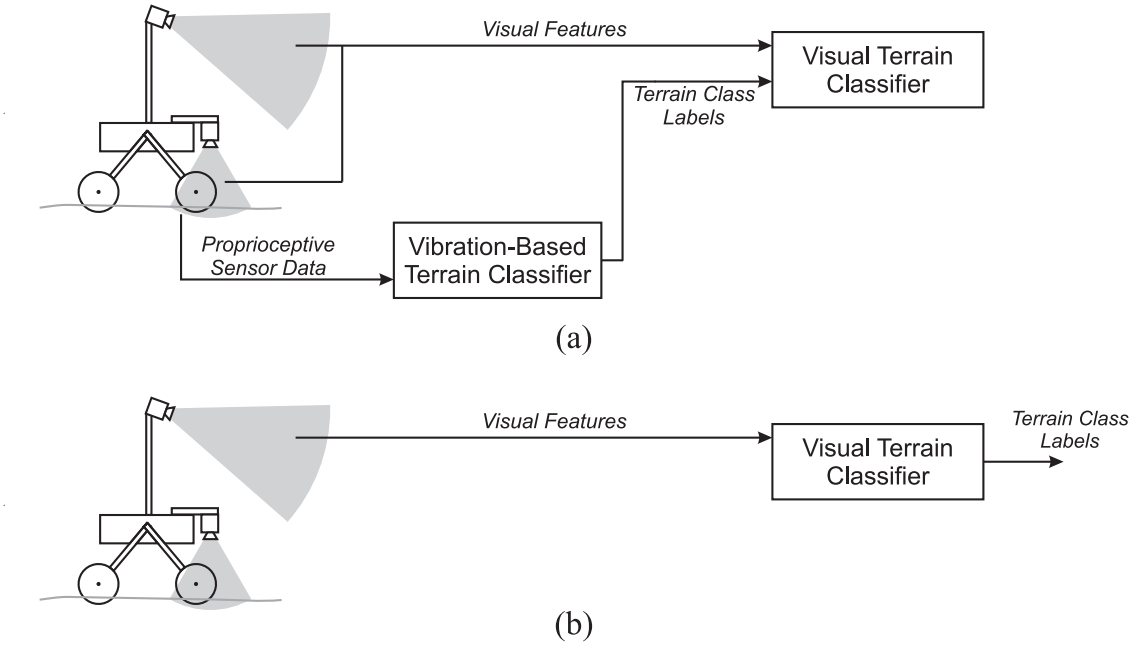

Figure 5-2. Information flow in self-supervised classification framework during (a) training and (b) classification

5.1.2.2 Vibration-Based Terrain Classification

In the self-supervised classifier framework studied in this section, a vibration-based terrain classifier (described in 2.1) provides labeled examples for training a visual classifier (described in 1.1). The vibration classifier labels terrain patches based on vibrations recorded by a contact microphone fixed to the rover suspension near its right

front wheel. Here it fills the role of the "supervisory" classifier, because it supervises the labeling of training data.

The vibration-based terrain classifier represents vibrations as log-scaled power spectral densities computed over a 1-second window. The 558-element representation is classified using a support vector machine (SVM) that has been trained using human-labeled vibration data. Full details on this classifier are presented in 2.1.

It should be noted that in the self-supervised classification framework, care must be taken to ensure the accuracy of the supervisory classifier. This is necessary to prevent incorrect labels from corrupting the training of the visual classifier. In this work, accuracy is guaranteed by combining multiple separate vibration-based class predictions for each terrain patch. Thus, the vibration-based terrain classifier identifies a terrain class based on each 1-second segment of vibration data. Since the rover travels at a slow speed, multiple vibration segments correspond to the same terrain patch, and each of them is classified independently. If any of these terrain class assignments disagree, no training data from that terrain patch is used for training the visual classifier.

5.1.2.3 Vision-Based Terrain Classification

The vision-based classifier in this self-supervised framework has been presented in 1.1. This classifier is intended to classify distant terrain patches based on visual features derived from color stereo images. As described in 1.1, color stereo cameras yield color, visual texture, and geometry classification features. Features associated with each of these sensing modes are classified using separate support vector machines, and the resulting class likelihoods are combined using naïve Bayes fusion. It should be noted that

no novel terrain detection stage is employed here, because all of the terrain patches are expected to correspond with one of the known terrain classes.

5.1.2.4 Self-Supervised Training Framework

Two different approaches for obtaining the visual data necessary for training a vision-based classifier are considered here: 1) the visual data can be captured using a belly-mounted camera, termed "local training," or 2) the visual data can be captured using stereo cameras, termed "remote training." Each of these approaches has advantages and disadvantages, and these two approaches are compared based on their experimental performance in 5.1.4.

5.1.2.4.1 Local Training

The first approach, termed "local training," trains the visual terrain classifier using images from a belly-mounted camera captured simultaneously with the vibration data collection. The information flow for the this approach is shown in Figure 5-3, and a sample image from a belly-mounted camera is shown in Figure 5-4. Thus, as soon as the vibration-based classifier returns a terrain class label, the belly-mounted camera captures an image of the terrain. Image data from all proprioceptively classified terrain patches are used to train the visual classifier, which is then used to classify terrain based on visual features derived from the forward-looking stereo cameras.

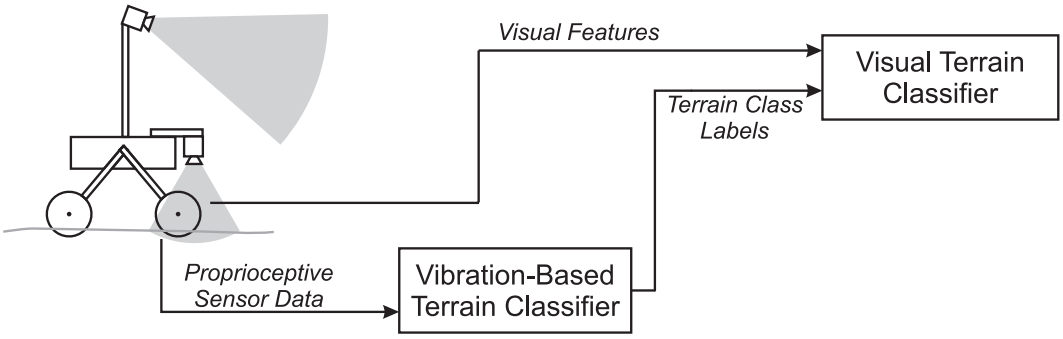

Figure 5-3. Information during training phase using local training approach

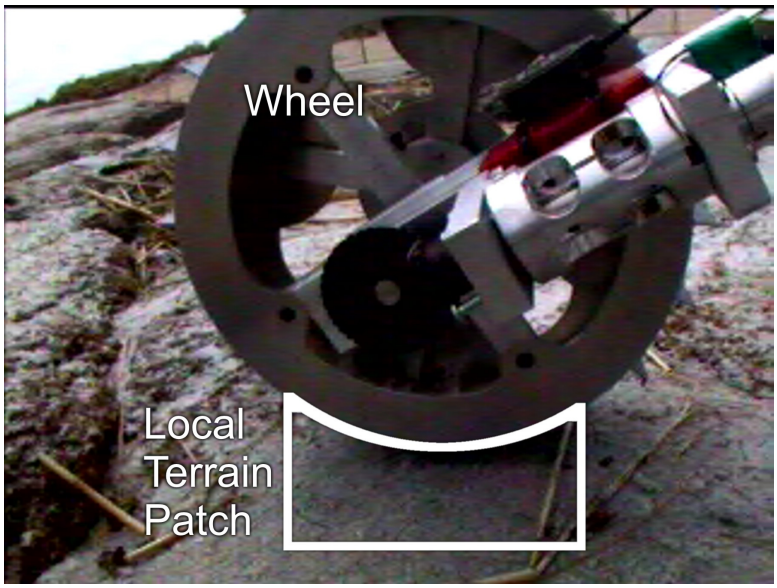

Figure 5-4. Sample image from belly-mounted camera

This approach is easy to implement but has several drawbacks. First, terrain geometry is not available in images captured by the monocular belly-mounted camera on our rover, so no geometry data is available to train the visual classifier. Second, texture data calculated from a belly-mounted camera image is not easily comparable to texture data from a forward-looking stereo camera image because the scales at which the terrain is viewed are different.[25] Thus, visual texture training data is not available to train the visual classifier. Because of these limitations, the visual classifier is restricted to

[25] Scaling of the texture features from one camera to another may be possible, but it was not explored in this thesis.

classifying terrain based on color features, and consistency of color data between the belly-mounted camera and forward-looking stereo cameras depends on careful control of the color calibration between the cameras.

5.1.2.4.2 Remote Training

In the second approach, termed "remote training," forward-looking stereo images are stored in memory and recalled when the rover classifies a previously observed terrain patch using proprioceptive sensors, as illustrated in Figure 5-5. Thus, color, visual texture, and geometry features (F_{color}, $F_{texture}$, and $F_{geometry}$) associated with a given terrain patch, located at position (x,y) are stored in memory after being observed by the forward-looking stereo cameras at time t_0. When, at a later time t_1, the rover reaches position (x,y), it uses proprioceptive sensors to identify the terrain class C associated with terrain patch P. The proprioceptively identified terrain class C, and the remotely sensed visual features F_{color}, $F_{texture}$, and $F_{geometry}$ are then used to train the visual terrain classifier.

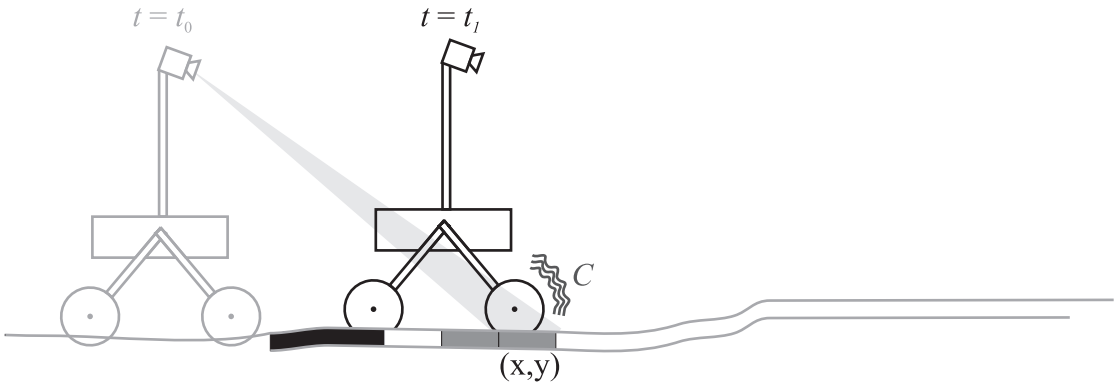

Figure 5-5. Illustration of visual information being recalled in remote training approach

This second approach relies on stereo processing to correlate image pixels with their corresponding terrain patch and on accurate position estimation to identify the location of the terrain patch the rover's proprioceptive sensors are measuring. However,

this approach does not depend on accurate color calibration between multiple cameras, and texture and geometric data are readily available for use in training the visual classifier.

5.1.2.4.3 Local and Remote Training

In both self-supervised classification approaches, training data is accumulated as the rover travels, and the training data for each terrain class is stored in memory. To limit the training time for the visual classifier, each terrain class is limited to a maximum of 400 sets of features[26]—some of the older data is discarded if new data arrives that would exceed that maximum.[27] Visual terrain classification is implemented on a patch level; each terrain patch is classified via naïve Bayes fusion of the color, visual texture, and geometric features sensed for pixels corresponding to that patch.

It should be noted that the decision to use a support vector machine for the self-supervised visual classifier is particularly important, because there is a non-negligible chance that some of the training data may be incorrectly labeled. A boosting algorithm such as AdaBoost (Freund & Schapire, 1997) would be particularly inappropriate, because it would tend to assign excessively high importance to misclassified training data.

[26] It was observed in experimental analysis that 400 sets of features per terrain class represented a good balance between computation cost and classification accuracy.

[27] The number of new feature sets added to the training data is the number of new feature sets sensed, up to the maximum of (1) 400 minus the number of old sets of features, (2) 400 divided by the number of terrain patches represented in the training data, and (3) four (representing 1% of 400). If adding this many new feature sets would increase the training data beyond the 400 sets of features, older feature sets are discarded randomly to decrease the number to 400 feature sets. Randomly discarding older features has the effect of providing an exponentially decreasing likelihood that a feature from an older data set will be maintained, thus allowing the visual terrain classifier to adapt to slow changes in illumination, while not being excessively sensitive to the appearance of the most recently added terrain patches.

5.1.3 Experiment Details

The two self-supervised classification approaches were compared to a traditional manually trained classifier—presented in 1.1—using experimental data collected on TORTOISE, a four-wheeled mobile robot developed at MIT, in an outdoor beach environment.

5.1.3.1 Robot Configuration

TORTOISE, shown in Figure 5-6, is an 80-cm-long, 50-cm-wide, 90-cm-tall robot with 20-cm-diameter rigid aluminum wheels with grousers. The wheels on either side are connected to the main body and mast via a differential. Full details on this robot are presented in Appendix A.

Figure 5-6. TORTOISE, showing location of stereo camera pair

For validation of the self-supervised classification framework, many of TORTOISE's sensors were used, including the forward-looking mast-mounted stereo

camera pair, the belly-mounted monocular camera, the vibration sensor, and a body-mounted two-axis tilt sensor. The stereo camera pair captured 640×480 resolution RGB color image pairs of the terrain in front of the rover. Range data were extracted from these images using SVS (Small Vision System), Videre Design's commercial stereo processing software. The belly-mounted monocular camera captured 320x240 resolution RGB color images of the right-front wheel and its immediate surroundings. Vibrations were sensed using the contact microphone mounted on the suspension near the rover's right front wheel. The two-axis tilt sensor measured body pitch and roll for proper registration of the stereo camera images.

During experiments the rover traveled at an average speed of 3 cm/sec. Vibrations were recorded at 44.1 kHz, body pitch and roll were captured at 26.7 Hz, images from the belly-mounted camera were captured at 2 Hz, and forward-looking stereo image pairs were captured at 0.66 Hz.[28] These data were stored during experiments and processed offline.

5.1.3.2 Experiment Environment

Wingaersheek Beach was used as the environment for validating the self-supervised classification framework. Here, the three distinct terrain classes were sand, rock, and beach grass. These classes are shown in Figure 5-7. A full description of Wingaersheek Beach is presented in Appendix B.

[28] The belly-mounted camera rate of 2 Hz was chosen to be able to sense the slow changes of wheel sinkage and capture multiple images of each terrain patch contacted by the rover wheel. The forward-looking stereo image rate was limited by available storage on the rover computer.

Figure 5-7. TORTOISE on Wingaersheek Beach, showing terrain classes

Six experimental data sets were used in this analysis. Each data set was collected during a single rover traverse of 10 to 35 meters along a straight-line path containing a combination of two or three terrains. No two paths were identical. These experiments were conducted over the course of three days. During experiments the lighting varied from uniform diffuse light from an overcast sky to harsh direct light from the sun low in the sky.

5.1.3.3 Data Processing

After the experiments were complete, stored data was processed offline. Range data were calculated for every fifth stereo image pair.[29] Every 20th stereo image pair[30] was labeled by hand to identify the ground-truth terrain class corresponding to each pixel. By combining the labels with the range data, ground truth terrain classes were identified

[29] Every fifth image pair was chosen to reduce the computation time for range data calculation and to reduce repeated training and testing on the same image patches viewed from nearly identical positions.
[30] Every 20th image pair was chosen to provide at least 10 labeled stereo image pairs in each data set.

for each 20-cm by 20-cm terrain patch. For each of the six data sets, between 10 and 28 stereo image pairs were labeled. Additionally, every image from the belly-mounted camera was labeled to identify the ground truth terrain class under the rover's right-front wheel.

For the baseline manually supervised classifier, the first two stereo image pairs with ground truth labels were used to train a visual classifier for each data set. Four hundred data features for each sensing mode from each class were used for training the classifier. The remaining hand-labeled images from that data set were used for testing. Across all six data sets, 93 image pairs were used for assessing the accuracy of the visual classifiers.

For self-supervised classification, a separate vibration-based classifier was trained for each data set, using hand-labeled vibration data from the other data sets. This vibration-based classifier was then used to provide labels for the entire rover traverse. At the end of the traverse, the self-supervised visual classifier was trained using 400 features from each sensing mode for each class. The accuracy of the self-supervised classifier was tested using the same stereo test images as were used for testing the baseline manually supervised classifier.

5.1.4 Results

5.1.4.1 Approach 1: Local Training

The first approach for self-supervised training of a visual terrain classifier uses images from a monocular belly-mounted camera as training data, with labels provided by a vibration-based classifier. Since geometry information is not available from the belly-

mounted camera and visual texture is not easily comparable between the belly-mounted camera and the stereo cameras (due to the difference in observation distance), color information is used exclusively.

Figure 5-8 shows the receiver operating characteristic (ROC) curves for the locally trained self-supervised visual classifier. This plot shows classification accuracy as measured using the 26 test images from one data set. Here, the horizontal axis indicates the percentage of false positives (%FP) and the vertical axis indicates the percentage of true positives (%TP). Note that the scale of the horizontal axis is much larger than that of the vertical axis, to allow the curves to be seen more easily. Each curve on the plot represents a single terrain, since both %TP and %FP are functions of the threshold for leaving terrain unclassified. The end point of each curve represents the point at which none of the terrain is left unclassified. Random assignment of terrain patches to classes would tend to yield a diagonal line along which the true positive percentage equals the false positive percentage.

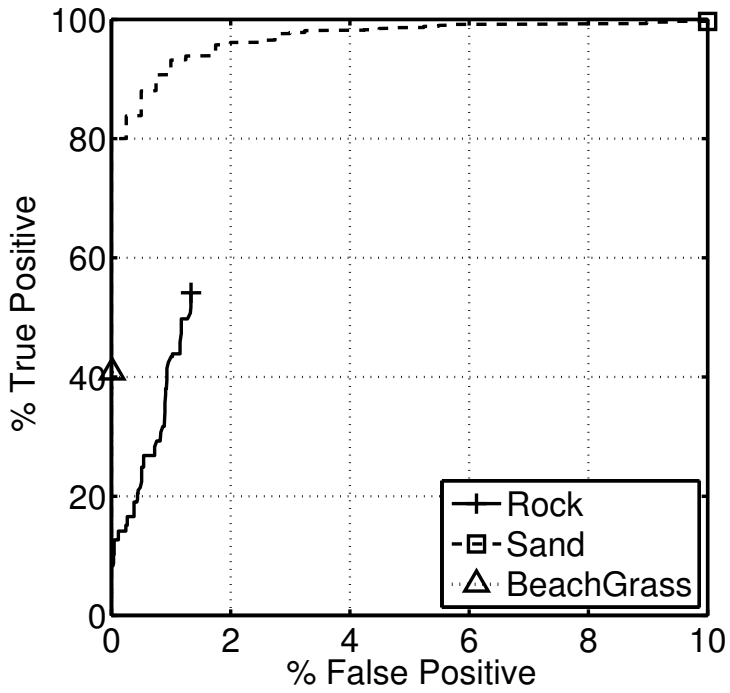

Figure 5-8. ROC curves for self-supervised classifier using local training

It can be seen that more than 90% of the sand is correctly classified before 1% of the other terrains are falsely identified as sand. Classification of rock is also very accurate, though less sensitive, with more than 50% of the rock correctly classified before 1.5% of the other terrains are falsely identified as rock. Here the curve for beach grass is only barely visible, since it lies along the vertical axis. With no terrain left unclassified, 41% of the beach grass was correctly classified, with less than 0.1% of the other terrains being falsely identified as beach grass. High accuracy was also observed for several of the other data sets, but a few data sets showed significantly worse performance—some even worse than random—suggesting potential fragility of this local training approach in real world environments.

For comparison, a manually trained visual classifier was implemented. This classifier was trained using color, texture, and geometry data from the first two images in

the data set. For each terrain, 400 feature vectors for each sensing mode were randomly selected and used for training. Figure 5-9 shows ROC curves for this classifier applied to the same 26 test images used for the self-supervised classifier. Note that there is no overlap between the images used for training and those used for testing.

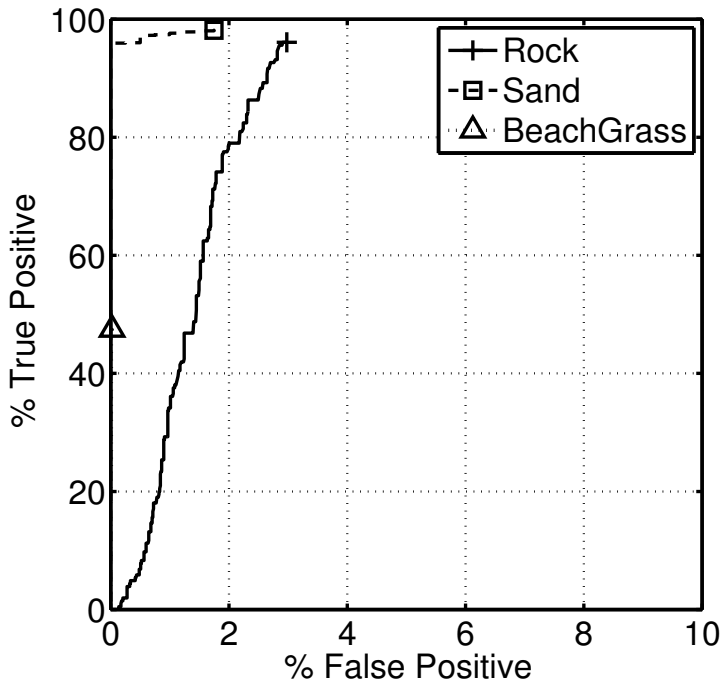

Figure 5-9. ROC curves for manually trained classifier

It can be seen that, the manually trained classifier performed very well for this data set. The highest classification accuracy is again observed for the sand class, with more than 95% of the sand correctly classified before any of the other terrain is falsely identified as sand. The correct classification rates of both beach grass and rock are improved over the self-supervised approach—at 66% and 81%, respectively—but at a cost of slightly higher rates of false positives.

Self-supervised classifiers and manually trained classifiers were implemented for each of the six data sets, and the results are shown in Table 5-1. Here, ROC curves were

generated showing the combined true positive and false positive rates across all three terrain classes. The performance of each classifier on a data set was summarized by a single point on the ROC curves—the point at which the difference between the true positive percentage and the false positive percentage is at a maximum. The first two rows of the table show statistics of the true positive percentage of the classifiers, corresponding to the vertical coordinate of the optimal point along the ROC curves. The third and fourth rows show statistics of the false positive percentage, corresponding to the horizontal coordinate of the optimal point. The last two rows show statistics related to the ratio between the true positive percentage and the false positive percentage. This metric, %TP/(%TP + %FP), is the fraction of labeled patches which are labeled correctly. Note that the numbers in brackets indicate a 95% confidence interval for each metric.

TABLE 5-1. COMPARISON OF SELF-SUPERVISED CLASSIFICATION USING LOCAL TRAINING TO MANUALLY SUPERVISED CLASSIFICATION

	Self-Supervised Classifier using Local Training (Color only)	Manually Supervised Classifier	Manually Supervised Classifier (Color only)
Mean % True Positive	42.7% [0% - 92.4%]	94.2% [91.1% - 97.3%]	96.6% [95.2% - 97.9%]
St. Dev. of % True Positive	47.4% [26.9% - 100%]	2.9% [1.8% - 7.2%]	1.3% [0.8% - 3.1%]
Mean % False Positive	7.3% [0% - 18.9%]	4.7% [1.5% - 8.0%]	3.3% [1.9% - 4.8%]
St. Dev. of % False Positive	7.3% [4.1% - 27.2%]	3.1% [1.9% - 7.6%]	1.4% [0.9% - 3.4%]
Mean %TP/(%TP + %FP)	0.76 [0.30 – 1.0]	0.96 [0.94 – 0.98]	0.97 [0.95 – 0.98]
St. Dev. of %TP/(%TP + %FP)	0.29 [0.16 – 1.0]	0.02 [0.01 – 0.04]	0.01 [0.01 – 0.03]

It can be seen that the self-supervised classifier using local training (Table 5-1, first column) demonstrates a poor true positive rate, as denoted by the 42.7% mean value.

The false positive rate is low—7.4% on average—but the other classifiers demonstrated significantly lower false positive rates, especially as compared to their true positive rates as indicated by the %TP/(%TP + %FP) metric. The manually supervised classifier demonstrates better performance than the self-supervised classifier using local training in each of the metrics. Most of these differences were statistically significant. It should be noted that there were several runs for which the self-supervised classifier using local training performed nearly as well as the manually supervised classifier, but its average performance was degraded by runs in which it performed significantly worse, suggesting that the self-supervised classification approach using local training suffers from poor robustness, possibly due to shadows on the terrain observed by the belly-mounted camera.

To analyze whether the difference between these classifiers was due to the use of texture and geometric features[31], an additional manually trained classifier was implemented using only color data. Results from that classifier are shown in the third column of Table 5-1. These results show that the manually supervised classifier using only the color feature is significantly more robust than the self-supervised classifier. Thus, other factors, such as miscalibration between cameras used for training and cameras used for testing, are likely to be the cause of the poor performance of the locally trained self-supervised classifier.

It should be noted that while the manually supervised classifier based solely on color seems to perform slightly better for these data sets, this difference does not appear

[31] Recall that the self-supervised classifier using local training employed only color features, whereas the manually supervised classifier employed color, visual texture, and geometry features.

to be significant. In previous work this difference has favored the manually supervised classifier using color, texture, and range data (Halatci et al., 2008).

5.1.4.2 Approach 2: Remote Training

The second approach to self-supervised training of a visual classifier is to store in memory the appearance of a terrain patch (as measured by the forward-looking stereo pair) and recall the appearance when the rover comes into contact with that terrain patch. Stereo-derived range estimation is used to associate pixels with terrain patches, and wheel odometry-based position estimation associates the rover's position at a later time with the terrain patch. Since this approach uses the same cameras for collecting both training data and test data, color, texture, and geometry data are all available for training, and the potential for color miscalibration is eliminated.

Figure 5-10 shows ROC curves for the self-supervised terrain classifier based on remote training for the same 26 images used for the results shown in Figure 5-8 and Figure 5-9. The remotely trained self-supervised visual classifier demonstrates accurate terrain classification on this data set. More than 80% of both sand and beach grass are correctly classified before 1% of the other terrains are misclassified as either. While the classification of rock has a low false positive rate—less than 1.5%—the classifier is less successful at detecting rock than the other terrains. Just under 25% of the rock was correctly classified for this data set.

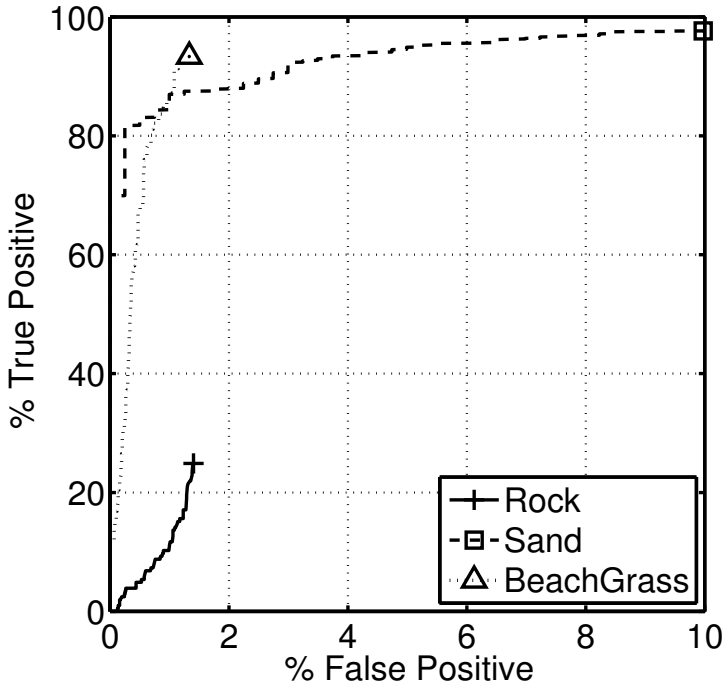

Figure 5-10. ROC curves for self-supervised classifier using remote training

A remotely trained self-supervised classifier and a manually trained classifier were implemented for each of the six data sets, and the results are shown in the first two columns of Table 5-2. The metrics shown are the same as in Table 5-1. Here it can be seen that the self-supervised classifier using remote training performs almost as well as the manually supervised classifier for each of the metrics. In fact, the difference in performance between the two classifiers is not statistically significant. The low values for the standard deviations suggest that this remote training approach to the self-supervised classification is significantly more robust than the local training approach.

TABLE 5-2. COMPARISON OF SELF-SUPERVISED CLASSIFICATION USING REMOTE TRAINING TO MANUALLY SUPERVISED CLASSIFICATION

	Self-Supervised Classifier using Remote Training	Manually Supervised Classifier	Manually Supervised Classifier (Prior Data Set)
Mean % True Positive	94.7% [91.0% - 98.3%]	94.2% [91.1% - 97.3%]	69.1% [29.7% - 100%]
St. Dev. of % True Positive	3.5% [2.2% - 8.5%]	2.9% [1.8% - 7.2%]	37.6% [23.4% - 92.1%]
Mean % False Positive	5.3% [1.5% - 9.1%]	3.8% [2.0% - 5.5%]	11.3% [0% - 24.6%]
St. Dev. of % False Positive	3.6% [2.2% - 8.8%]	1.7% [1.0% - 4.1%]	12.6% [7.9% - 31.0%]
Mean %TP/(%TP + %FP)	0.95 [0.92 - 0.99]	0.96 [0.94 - 0.98]	0.85 [0.66 - 1.0]
St. Dev. of %TP/(%TP + %FP)	0.03 [0.02 - 0.08]	0.02 [0.01 - 0.04]	0.16 [0.09 - 0.45]

The self-supervised approach is intended for situations when a manually trained classifier is not a viable option, due to the necessity of human labeling of terrain. In a planetary exploration setting, manual training would impose a significant delay between the time that training images were collected and the time that the trained classifier could be implemented. Thus, the accuracy of a self-supervised classifier is more fairly compared to a manually trained classifier trained on a previously collected data set. In this scenario, the training images for the manually supervised classifier are hand-labeled images drawn from one data set, and the performance of the classifier is tested using images from the following data set, captured minutes or days later. This results in variation in illumination for some data sets. For example, one of the data sets was captured with overcast skies, and the next was captured with low-angle, direct sunlight.

The accuracy of such a classifier is presented in the third column of Table 5-2. Here the difference in performance between the self-supervised classification approach and the manually supervised classification approach is clear. The self-supervised

classification approach yields better true positive classification, a lower false positive rate, and higher overall classification accuracy, as compared to the manually supervised classifier when training delay is added.

5.1.4.3 Computation time

To enable real time operation, an effort was made to limit the computational complexity of training and testing of these classifiers, so the most computationally intensive tasks were stereo data extraction and texture feature computation. Extraction of geometric features from a 3-D point cloud takes an average of 5 seconds per image using a Matlab script on a Pentium 4 1.8 GHz desktop computer. Texture feature extraction takes 17.3 sec, using an unoptimized Matlab script. A C-code implementation would be expected to run much faster.

Because it doesn't rely on stereo data or texture feature extraction, the locally trained classifier can be trained very quickly. Training takes 1.7 seconds on a Pentium 4 1.8 GHz desktop using the LIBSVM library. Color-based classification takes only 0.7 seconds for a full 640×480 image. Classifying terrain patches requires that stereo data be computed to identify which pixel belongs to which patch; once that data is computed, each patch took an average of 0.01 seconds to classify in Matlab, with an average of 400 patches per image.

The remotely trained classifier took slightly less time to train, at 1.5 seconds on average, because some of the terrains had fewer than 400 training data points. Classification was slower for the remotely trained classifier, at 4.1 seconds per image, due to the use of texture and geometry data.

5.1.5 Conclusions

In this section, two self-supervised classification approaches were presented. Both approaches train a visual classifier using terrain class labels identified locally using a vibration-based terrain classifier. The first approach uses images from a belly-mounted camera as training data. It was shown to have excellent performance in classifying terrain for some data sets, but experimentally observed results were inconsistent. The second approach uses the recalled appearance of a terrain patch to provide training data for a visual classifier. This approach was shown to perform as well as a manually supervised classifier trained using the same data set, and was shown to perform significantly better than the manually supervised classifier when a delay due to manual training is considered.

While these results support the use of autonomous labeling to train a visual classifier, the vibration-based terrain classifier used to perform the labeling requires its own manually supervised training. Thus it is not a truly unsupervised approach suitable for application to novel environments where no a priori knowledge is available.

5.2 Self-Supervised Terrain Learning System for Novel Environments

5.2.1 Introduction

For scenarios in which no a priori information about the terrain is available, a completely unsupervised terrain learning system can be assembled using the self-supervised classification framework and component algorithms developed and validated earlier in this thesis. As with the self-supervised learning system validated in 1.1, this terrain learning system learns to identify instances of a terrain class in the distance based

on the appearance of proprioceptively sensed terrain patches. However, the terrain learning system presented in this section uses terrain classes defined based on an explicitly calculated traversability metric, eliminating the need for human supervision during the training of the proprioceptive terrain classifier. This unsupervised terrain learning system was applied to experimental data from a four-wheeled rover in natural outdoor terrain.

5.2.2 Terrain Learning System Framework and Algorithmic Components

The proposed framework for self-supervised terrain learning is shown in Figure 5-11. Within this framework the various individual components—the proprioceptive terrain classifier, the exteroceptive terrain classifier, and the terrain characterization algorithm—can be modified depending on the scenario in which the system is operating. These components all work together to produce a terrain property map, which is a representation of the topography and predicted mechanical terrain characteristics of the terrain patches in front of the rover. The components assembled for the results presented in 5.2.4 are presented below.

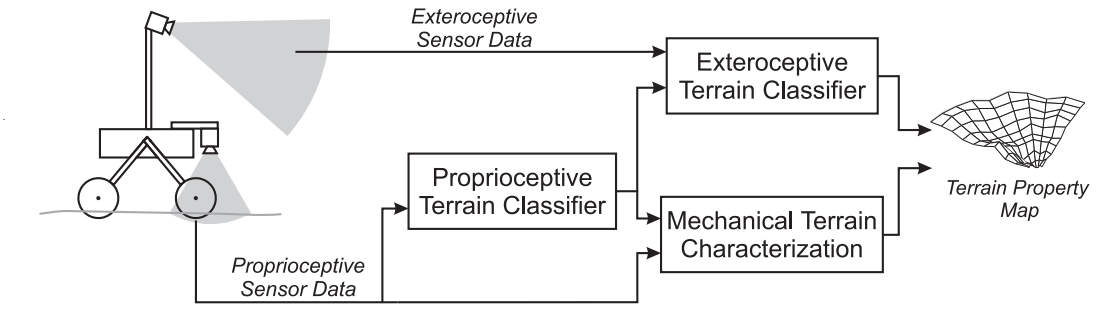

Figure 5-11. Information flow for self-supervised classification framework

5.2.2.1 Self-Supervised Learning Approach

As described in 1.1, there are multiple potential approaches to self-supervised learning. Based on the experimental results, the "remote training" approach was chosen for implementation in this terrain learning system. In this approach, images from forward-looking stereo cameras are stored in memory. When the proprioceptive terrain classifier identifies the class associated with a terrain patch, the terrain patch's appearance is recalled to use in training the exteroceptive terrain classifier. This approach relies heavily on the accuracy of stereo processing and rover position estimation to properly associate the image data with the class labels, but it was shown using experimental data to yield more robust classification than the "local training" approach.

5.2.2.2 Proprioceptive Terrain Classifier

The proprioceptive terrain classification component for the terrain learning system is derived from the mechanical terrain characterization work presented in Chapter 4. In this algorithm the local terrain is divided into classes based on the minimum bound for the net traction force, sensed during the 67% slip stage of the "Incremental Slip" behavior described in 2.2.2. (Vibration-based terrain classification, presented in 2.1, was not used because it requires use of a priori knowledge of the terrain classes and human-supervised labeling of vibration data. Torque-based terrain clustering, presented in 1.1, was not used because it didn't perform well in the experiments with the "Incremental Slip" behavior, and experiments with moderate values of slip are required for the mechanical terrain characterization algorithm.)

Here, for every local terrain patch with associated slip data, DP/W bounds were calculated using the Bekker model with absolute sinkage described in 4.2.4.3. Five terrain

classes were defined based on the lower bound of DP/W. These classes, labeled *A* through *E*, are shown in Table 5-3. Class *A* corresponds to terrain which can be easily traversed, such as rock with a rough surface that a rover's grousers can grip. Class *E* corresponds to terrain which is untraversable for any slope, such as a highly compressible slippery powder into which a rover's wheels would sink. Classes *B* through *D* correspond to terrains which lie between those two extremes. These class labels are passed on to the mechanical terrain characterization and remote terrain classification algorithms.

TABLE 5-3. CLASS LABELS AND ASSOCIATED *DP*/*W* RANGES

Class Label	Range for DP/W lower bound
A	0.5 to ∞
B	0.25 to 0.5
C	0.1 to 0.25
D	0 to 0.1
E	-∞ to 0

5.2.2.3 Exteroceptive Terrain Classifier

In the terrain learning system, exteroceptive terrain classification was implemented using the two-stage visual classifier presented in Chapter 3. This approach uses a two-class SVM classifier to identify whether a terrain patch contains novel terrain, and a separate SVM classifier to identify which of the known classes is associated with the terrain. Both stages use the same color, texture, and geometry features to represent the terrain.

Since the two stages both output probabilities, it is straightforward to identify the probability of a distant terrain patch being associated with each of the five known classes (*A, B, C, D,* and *E*), or the unknown class, *Unknown*:

$$P(A) = P(A \mid Known)\ P(Known) \tag{5-1}$$

and

$$P(Unknown) = P(Novel)\,, \tag{5-2}$$

where $P(Known)$ and $P(Novel)$ are outputs of the novel terrain detector, and $P(A|Known)$ is one of the outputs of the known terrain classifier. Thus, the remote terrain classifier calculates the probability of each terrain cell belonging to each terrain class: [$P(A)$, $P(B)$, $P(C)$, $P(D)$, $P(E)$, $P(Unknown)$].

5.2.2.4 Terrain Characterization

In the instantiation of the terrain learning system described here, the terrain classes identified by the proprioceptive terrain classifier are defined by their mechanical characteristics, so a separate terrain characterization stage is redundant.

5.2.2.5 Class/Property Fusion

The last important step in producing the terrain property map is to combine the outputs of the remote terrain classifier with the output of the terrain characterization algorithm. To make the terrain property map easier to interpret, it is desirable to have only a single number represent the terrain traversability in each patch. For this terrain learning system, that number is a conservative estimate for the net traction force, DP/W.

Here that conservative estimate of DP/W is defined as the highest value for which there is at least an 80% probability that the true value would be higher. This can be calculated from the ranges of lower DP/W bounds associated with the classes (Table 5-3) and the class probabilities from the remote terrain classifier. For example, given the probabilities $P(A) = 50\%$, $P(B) = 25\%$, $P(C) = 6\%$, $P(D) = 10\%$, $P(E) = 4\%$, $P(Unknown) = 5\%$, a conservative estimate of DP/W for the associated terrain cell would be 0.1 (i.e.

the lower end of the range for class C), because $P(A) + P(B) + P(C) \geq 80\%$. The value of 80% was chosen because it provides a reasonable balance between being too cautious (since the ranges are already estimates of the lower bound of DP/W) and being too optimistic (which could endanger the safety of a rover).

5.2.3 Experiment Details

The terrain learning system was applied to data from a traverse of the four-wheeled rover, TORTOISE, on Wingaersheek Beach. This is the same platform and environment on which all of the algorithms in this thesis have been tested. A description of TORTOISE is presented in Appendix A. A description of Wingaersheek Beach is presented in Appendix B.

Several of the sensors on TORTOISE were used during testing of the terrain learning system. Rover wheel torque was sensed using the torque sensor attached to the right front wheel. The appearance of distant terrain was sensed using the mast-mounted stereo cameras. Rover wheel velocity was sensed using encoders mounted to each wheel motor, and this velocity was integrated to estimate the rover's position. Pitch and roll of the main body were sensed using a two-axis tilt sensor mounted on the rover body. Images from the belly-mounted camera were used to measure absolute wheel sinkage. For the results presented here wheel sinkage measurement was implemented in post-processing using a human to manually identify the wheel-terrain interface, but this process could be automated using the visual wheel sinkage measurement approach presented in (Brooks, 2004).

The terrain learning system was applied to a single 10-meter traverse of the rover across the beach that included all three terrain classes: sand, beach grass, and rock.

During the traverse, the rover performed the "Incremental Slip" behavior described in 2.2.2, and all data was stored so that it could be passed to an offline implementation of the sensing system.

5.2.4 Results

The output of the terrain learning system is a prediction of a lower bound of net drawbar pull for each terrain patch as predicted using each stereo image. This is most easily viewed as a video, but still frames are shown in Figure 5-12, Figure 5-13, and Figure 5-14.

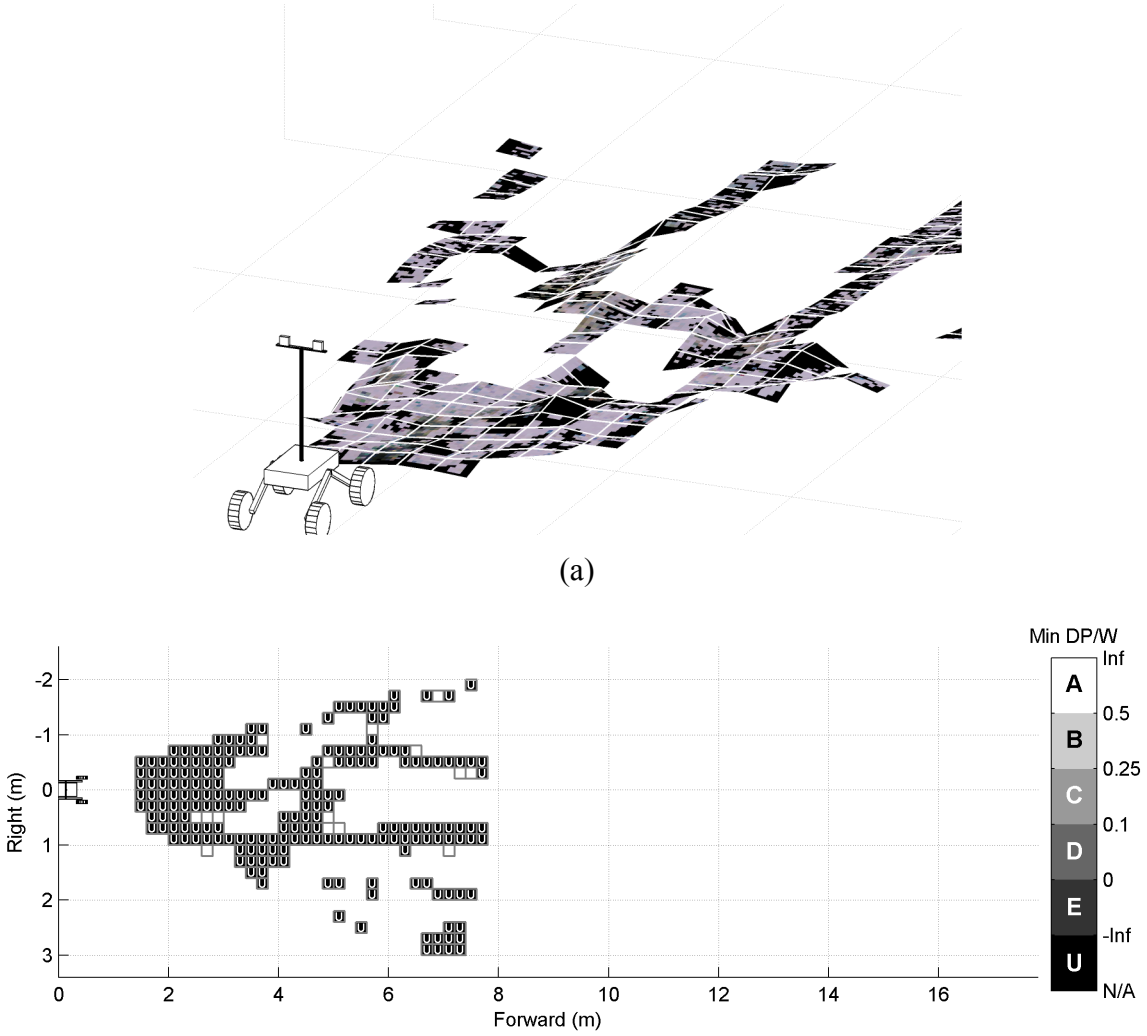

Figure 5-12. Terrain learning system results, at t = 5.0 sec, distance traveled = 0.13 m, (a) 3-D view, (b) plan view showing terrain classes

Figure 5-12 shows the rover's internal map of the terrain, just after it has started its traverse. Figure 5-12(a) shows a 3-D view illustrating the topography of the terrain as sensed by the rover (which is shown in the lower left corner of the image). At this instant, the range data calculated from the first two images from the stereo pair is sparse, as shown by the large gaps in the terrain map. Figure 5-12(b) shows a plan view of the terrain, with the terrain patches labeled based on the predicted lower bound of the drawbar pull. Since the rover hasn't completed mechanical characterization of any of the

terrain patches for which it has stereo data, there is no "known" terrain in the distance. All observed terrain is considered to be novel, and the terrain patches are labeled "U" (*Unknown*), signifying that it doesn't have sufficient experience to assess the traversability.

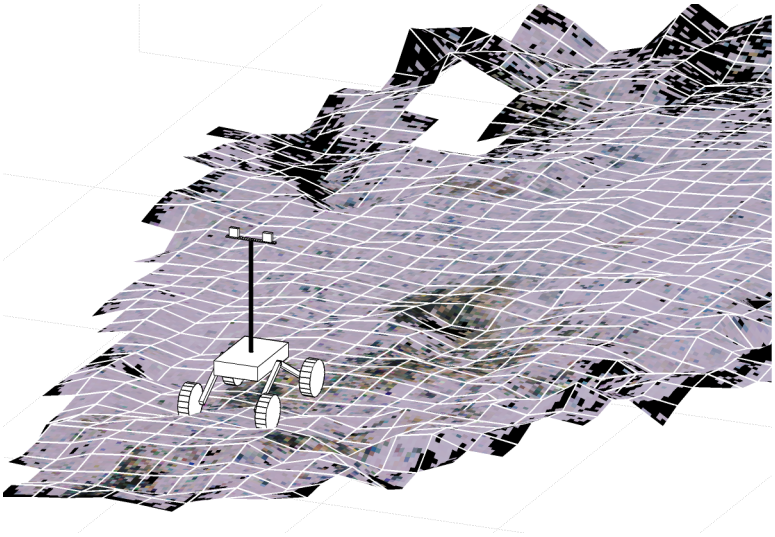

(a)

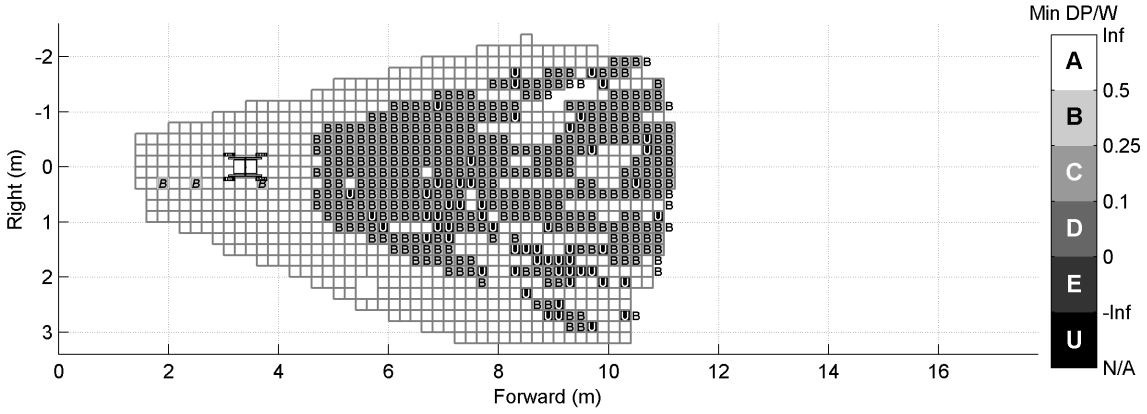

(b)

Figure 5-13. Terrain learning system results, at t = 129.0 sec, distance traveled = 3.4 m, (a) 3-D view, (b) plan view showing terrain classes

Figure 5-13 shows the rover's internal terrain map after 129 seconds, when the rover has traveled 3.4 meters. Figure 5-13(a) shows that the rover's knowledge of the terrain topography has increased, as illustrated by the reduced number of gaps in its

internal representation of the terrain. Figure 5-13(b) shows that the rover has identified the minimum net traction force for three terrain patches with associated stereo data. These are illustrated in the figure by the three labeled terrain patches at 1.9m, 2.5m, and 3.7m. (Here, terrain patches which have been characterized through physical interaction are labeled with italicized letters.) Since these three patches all fall into class *B* (representing a lower bound of DP/W between 0.25 and 0.5 from Table 5-3), all of the recognized (i.e. not novel) terrain in the distance is predicted to fall into that range. Terrain that is sufficiently different from the terrain the rover has driven over is still labeled "U," with unknown traversability properties.

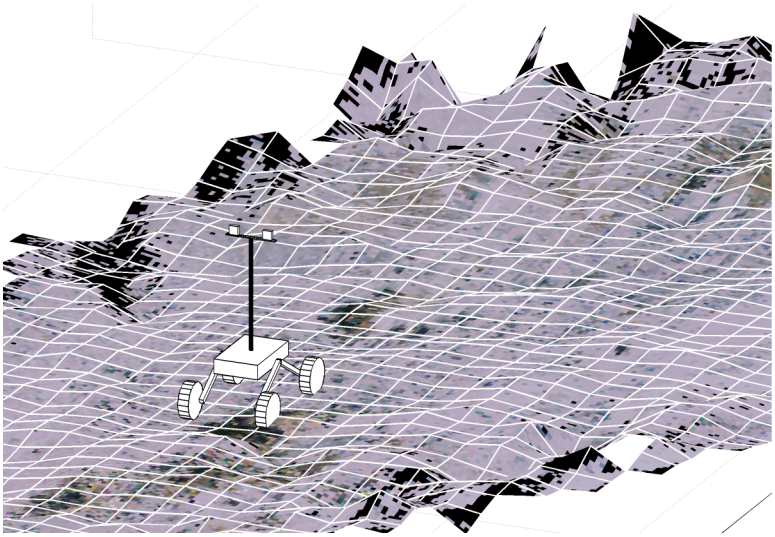

(a)

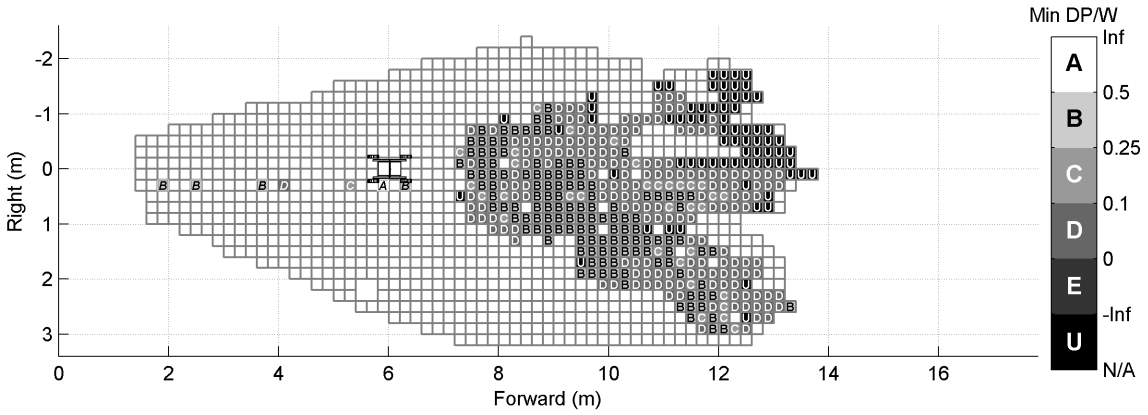

(b)

Figure 5-14. Terrain learning system results, at t = 226.5 sec, distance traveled = 6.02 m, (a) 3-D view, (b) plan view showing classes

Finally, Figure 5-14 shows the rover's internal terrain map after 226.5 seconds. At this point the rover has tactile data from terrain with a range of net traction forces, and it has associated visual data with several locally identified classes. Thus, when the terrain is observed in the distance, a variety of net traction forces are predicted. Some sections show high traction forces (labeled "B"), while others show lower traction forces (labeled "C" or "D"). In the distance, terrain is still observed to be novel, suggesting that the

terrain in the distance may have a significantly different appearance than the terrains previously traversed.

5.2.5 Conclusions

This section has presented a terrain learning system for novel environments that is capable of learning from experience to visually recognize terrain and predict a lower bound on the net traction force. This system employs a self-supervised learning approach that uses the recalled appearance of terrain from stored images to train a visual classifier. Proprioceptive terrain classification is accomplished by grouping terrain patches based on the mechanically sensed lower bound on the net traction force. Exteroceptive classification is accomplished using a two-stage visual classifier capable of recognizing novel terrain.

Results from the application of this complete terrain sensing system to an experimental data set yields reasonable results, however no ground truth is available to confirm the accuracy of the net traction force predictions. It is expected that the capabilities for visual recognition of the traction forces would continue to improve over significantly longer traverses. Future work is needed to establish how the tightness of the predicted traversability bounds will change over longer traverses.

Chapter

6

Conclusions and Suggestions for Future Work

6.1 Contributions of this Thesis

This thesis has presented a framework of algorithms to enable a planetary rover to accurately predict mechanical properties of terrain at a distance by learning from experiences gained during traverses of similar terrain. This has been accomplished through the use of a self-supervised learning framework, which provides a coherent architecture in which local terrain classification, remote terrain classification, and mechanical terrain characterization can be combined.

In Chapter 2, two distinct approaches were presented for classification of terrain based on proprioceptive sensor data. The first section presented a method for vibration-based terrain classification using a support vector machine (SVM). It is suitable for a supervised scenario, i.e. when labeled vibration training data is available. The second section presented a novel method for segmenting terrain based on the wheel torque sensed during high wheel slip ratio conditions. This approach is suitable for an unsupervised scenario, i.e. when the terrain classes are not known a priori. A comparison of experimental results using this approach showed that higher induced wheel slip ratios improve segmentation accuracy. Both local classification approaches were validated

using experimental data from a four-wheeled rover in a beach environment. These local terrain characterization approaches are viable methods for distinguishing terrain using features from proprioceptive sensors, making them inherently insensitive to changes in illumination.

Chapter 3 addressed exteroceptive classification of terrain. The first section described a SVM-based visual classifier, modeled on the approach of Halatci (Halatci, 2006; Halatci et al., 2008). It presented new experimental results for this classification approach. The second section addressed a specific shortcoming of a supervised classifier: recognizing when new observations are not associated with any of the trained classes. This section introduced a new approach to detection of novel terrain. This approach was specifically targeted to the self-supervised classification scenario in which a large quantity of unclassified training data is available. Data from rover experiments in a beach environment were used to validate this novelty detection approach. A two-stage visual classification system combining these two algorithms can both accurately classify terrain and detect terrain not belonging to the set of trained classes.

Chapter 4 addressed the issue of how to characterize terrain. It presented a method to calculate bounds on the net traction force based on observed wheel torque and sinkage under induced wheel slip conditions. Three different approaches were explored using data from laboratory experiments with a wheel-terrain interaction test platform, and the most promising approach was applied to experimental data from a four-wheeled rover on Wingaersheek Beach. This approach yields a physically meaningful metric for representing the traversability of terrain that is appropriate for situations when caution is required.

In Chapter 5, the self-supervised classification framework itself was studied. The first section compared two sources for training data for the visual classifier, based on classification performance on experimental data from Wingaersheek Beach. The second section presented a terrain learning system for novel environments, which combined proprioceptive classification, exteroceptive classification, and mechanical terrain sensing in a single system and applied it to experiment data from the TORTOISE rover on Wingaersheek Beach. Thus, the terrain learning system, in which each component was independently validated, was demonstrated.

6.2 Suggestions for Future Work

There are several areas in which this work could be extended. Where a suggestion applies only to a particular component, the suggestion has been included in the section in which the component is described. The suggestions described here can be divided into experimental extensions, computational extensions, and algorithmic extensions.

Experimental extensions are additional experiments that could be implemented without changing the terrain sensing algorithms. The easiest extension to accomplish would be to use the same robot platform and demonstrate that this terrain learning system (and each of its subcomponents) will work in a variety of unique environments. This should be straightforward in any environment that can be modeled as a height field; changes in the terrain representation would be required for it to operate in a fully 3-D environment. Applying this terrain sensing algorithm to a different platform, such as a high-speed UGV or a human-driven automobile, might also be promising.

Computational extensions would include changes in some of the underlying code which should reduce computation time without affecting the algorithm accuracy. For

example, all of the classification in this work is done using support vector machines. In situations when a linear or low-order polynomial kernel is used, the standard classification code can be significantly streamlined, which would enable faster classification. The overall approach for these optimizations are presented in Appendix D. There are likely to be optimizations along the same lines for reducing the time necessary for training the SVM classifier.

Algorithmic extensions would include changing some of the larger components of this sensing system. For example, computing the texture feature of the visual classifier is currently one of the slowest steps. If some other texture feature is easier to compute or yields better discrimination, it might be worthwhile to implement. Other changes which might be made include replacing the SVM with another classifier; Bayesian logistic regression is currently in favor. Another classification replacement to consider is the regularized least squares (RLS), which is likely to have a closed form solution for incremental training.

References

Angelova, A., Matthies, L., Helmick, D., & Perona, P. (2007a). Learning and prediction of slip from visual information. *Journal of Field Robotics*, *24*(3), 205-231. doi: 10.1002/rob.20179.

Angelova, A., Matthies, L., Helmick, D., & Perona, P. (2007b). Learning slip behavior using automatic mechanical supervision. In *Proceedings of the 2007 IEEE International Conference on Robotics and Automation (ICRA '07)* (pp. 1741-1748). Rome, Italy. doi: 10.1109/ROBOT.2007.363574.

Angelova, A., Matthies, L., Helmick, D., Sibley, G., & Perona, P. (2006). Learning to predict slip for ground robots. In *Proceedings of the 2006 IEEE International Conference on Robotics and Automation (ICRA '06)* (pp. 3324-3331). Orlando, FL.

Arvidson, R. E., Anderson, R. C., Bartlett, P., Bell, J. F., Blaney, D., Christensen, P. R., et al. (2004). Localization and Physical Properties Experiments Conducted by Spirit at Gusev Crater. *Science*, *305*(5685), 821-824. doi: 10.1126/science.1099922.

Bajracharya, M., Maimone, M. W., & Helmick, D. (2008). Autonomy for Mars Rovers: Past, Present, and Future. *Computer*, *41*(12), 44-50. doi: 10.1109/MC.2008.479.

Balas, B. J. (2006). Texture synthesis and perception: Using computational models to study texture representations in the human visual system. *Vision Research*, *46*(3), 299-309. doi: 10.1016/j.visres.2005.04.013 .

Bekker, M. G. (1969). *Introduction to Terrain-Vehicle Systems*. Ann Arbor: University of Michigan Press.

Bellutta, P., Manduchi, R., Matthies, L., Owens, K., & Rankin, A. (2000). Terrain perception for DEMO III. In *Proceedings of the 2000 IEEE Intelligent Vehicles Symposium (IV 2000)* (pp. 326-331). Dearborn, MI. doi: 10.1109/IVS.2000.898363.

Berni, J. A. J., Zarco-Tejada, P. J., Suarez, L., & Fereres, E. (2009). Thermal and Narrowband Multispectral Remote Sensing for Vegetation Monitoring From an Unmanned Aerial Vehicle. *IEEE Transactions on Geoscience and Remote Sensing*, *47*(3), 722-738. doi: 10.1109/TGRS.2008.2010457.

Bilmes, J. (1998). *A Gentle Tutorial of the EM Algorithm and its Application to Parameter Estimation for Gaussian Mixture and Hidden Markov Models*. Technical Report, Berkeley, CA: International Computer Science Institute. Retrieved November 21, 2008, from http://ssli.ee.washington.edu/people/bilmes/mypapers/em.pdf.

Bishop, C. M. (1995). *Neural Networks for Pattern Recognition*. Oxford, England: Clarendon Press.

Bouman, C., & Liu, B. (1991). Multiple resolution segmentation of textured images. *IEEE Transactions on Pattern Analysis and Machine Intelligence*, *13*(2), 99-113. doi: 10.1109/34.67641.

Brandes, U., Gaertler, M., & Wagner, D. (2003). Experiments on Graph Clustering Algorithms. In *Algorithms - ESA 2003*, Lecture Notes in Computer Science (Vol. 2832, pp. 568-579). Springer Berlin / Heidelberg. Retrieved November 12, 2008, from http://www.springerlink.com/content/cv8tbjmrhdflau3r.

Brooks, C. (2004). *Terrain Identification Methods for Planetary Exploration Rovers*. Thesis (S.M.), Massachusetts Institute of Technology. Retrieved from http://dspace.mit.edu/handle/1721.1/30303.

Brooks, C., & Iagnemma, K. (2005). Vibration-based terrain classification for planetary exploration rovers. *IEEE Transactions on Robotics*, *21*(6), 1185-1191. doi: 10.1109/TRO.2005.855994.

Brooks, C., Iagnemma, K., & Dubowsky, S. (2006). Visual wheel sinkage measurement for planetary rover mobility characterization. *Autonomous Robots*, *21*(1), 55-64. doi: 10.1007/s10514-006-7230-9.

Chang, C., & Lin, C. (2005). *LIBSVM: a library for support vector machines (Version 2.81) [Computer software]*. Retrieved from http://www.csie.ntu.edu.tw/~cjlin/libsvm.

Chang, C., & Lin, C. (2008, October 29). LIBSVM: a Library for Support Vector Machines. Retrieved November 20, 2008, from http://www.csie.ntu.edu.tw/~cjlin/papers/libsvm.pdf.

Cowen, R. (2005). Opportunity Rolls out of Purgatory. *Science News*, *167*(26), 413.

Denes, L. J., Gottlieb, M. S., Kaminsky, B., & Huber, D. F. (1998). Spectropolarimetric imaging for object recognition. In *26th AIPR Workshop: Exploiting New Image Sources and Sensors* (Vol. 3240, pp. 8-18). Washington, DC: SPIE. doi: 10.1117/12.300052.

DuPont, E., Roberts, R., Selekwa, M., Moore, C., & Collins, E. (2005). Online Terrain Classification for Mobile Robots. In *Proceedings of the 2005 ASME International Mechanical Engineering Congress and Exposition (IMECE2005)* (p. 81659). Orlando, FL.

El-Yaniv, R., & Nisenson, M. (2007). Optimal Single-Class Classification Strategies. In B. Schölkopf, J. Platt, & T. Hoffman (Eds.), *Advances in Neural Information Processing Systems (NIPS) 19* (p. 377—384). Cambridge, MA: MIT Press. Retrieved from http://eprints.pascal-network.org/archive/00002663/.

Espinal, F., Huntsberger, T. L., Jawerth, B. D., & Kubota, T. (1998). Wavelet-based fractal signature analysis for automatic target recognition. *Optical Engineering*, *37*(1), 166-174. doi: 10.1117/1.601844.

Freund, Y., & Schapire, R. E. (1997). A Decision-Theoretic Generalization of On-Line Learning and an Application to Boosting. *Journal of Computer and System Sciences*, *55*(1), 119-139. doi: 10.1006/jcss.1997.1504.

Goldberg, S., Maimone, M. W., & Matthies, L. (2002). Stereo vision and rover navigation software for planetary exploration. In *Proceedings of the 2002 IEEE Aerospace Conference* (Vol. 5, pp. 2025-2036). Big Sky, Montana.

Halatci, I. (2006). *Vision-Based Terrain Classification and Classifier Fusion for Planetary Exploration Rovers*. Thesis (S.M.), Massachusetts Institute of Technology. Retrieved from http://dspace.mit.edu/handle/1721.1/38271.

Halatci, I., Brooks, C., & Iagnemma, K. (2008). A Study of Visual and Tactile Terrain Classification and Classifier Fusion for Planetary Exploration Rovers. *Robotica*, *26*(6), 767-779. doi: 10.1017/S0263574708004360.

Hegedus, E. (1963). *Pressure Distribution and Slip-Sinkage Relationship Under Driven Rigid Wheels*. Technical Report, Warren, MI: Army Tank-Automotive Center, Land Locomotion Lab.

Henriksen, L., & Krotkov, E. (1997). Natural Terrain Hazard Detection with a Laser Rangefinder. In *Proceedings of the 1997 IEEE International Conference on Robotics and Automation (ICRA '97)* (Vol. 2, pp. 968-973). Albuquerque, NM. doi: 10.1109/ROBOT.1997.614260.

Iagnemma, K., & Dubowsky, S. (2002). Terrain estimation for high-speed rough-terrain autonomous vehicle navigation. In *Proceedings of SPIE Conference on Unmanned Ground Vehicle Technology IV* (Vol. 4715, pp. 256-266). Orlando, FL: SPIE. doi: 10.1117/12.474457.

Iagnemma, K., Kang, S., Brooks, C., & Dubowsky, S. (2003). Multi-Sensor Terrain Estimation for Planetary Rovers. In *Proceedings of the 7th International Symposium on Artificial Intelligence, Robotics and Automation in Space, i-SAIRAS*. Nara, Japan. Retrieved November 17, 2008, from http://citeseerx.ist.psu.edu/viewdoc/summary?doi=10.1.1.8.3791.

Iagnemma, K., Kang, S., Shibly, H., & Dubowsky, S. (2004). Online terrain parameter estimation for wheeled mobile robots with application to planetary rovers. *IEEE Transactions on Robotics*, *20*(5), 921-927. doi: 10.1109/TRO.2004.829462.

Iagnemma, K., Shibly, H., & Dubowsky, S. (2002). On-line terrain parameter estimation for planetary rovers. In *Proceedings of the 2002 IEEE International Conference on Robotics and Automation (ICRA '02)* (Vol. 3, pp. 3142-3147). Washington, DC. doi: 10.1109/ROBOT.2002.1013710.

Johnson, J. (2008, December 5). NASA delays Mars rover launch to 2011. *The Los Angeles Times*. Retrieved December 5, 2008, from http://www.latimes.com/news/printedition/asection/la-sci-mars5-2008dec05,0,5658120.story.

Kang, S. (2003). *Terrain Parameter Estimation and Traversability Assessment for Mobile Robots*. Thesis (S.M.), Massachusetts Institute of Technology.

Kim, D., Sun, J., Oh, S. M., Rehg, J. M., & Bobick, A. F. (2006). Traversability classification using unsupervised on-line visual learning for outdoor robot navigation. In *Proceedings of the 2006 IEEE International Conference on Robotics and Automation (ICRA '06)* (pp. 518-525). Orlando, FL.

Kivinen, J., Smola, A. J., & Williamson, R. C. (2004). Online learning with kernels. *IEEE Transactions on Signal Processing*, *52*(8), 2165-2176. doi: 10.1109/TSP.2004.830991.

Kohavi, R. (1995). A study of cross-validation and bootstrap for accuracy estimation and model selection. In *Proceedings of the International Joint Conference on Artificial Intelligence (IJCAI-95)* (pp. 1137-1143). Montreal, Canada: Morgan Kaufmann. Retrieved February 11, 2009, from http://robotics.stanford.edu/%7Eronnyk/accEst.pdf.

Konolige, K. (2007). *SVS: Small Vision System (Version 4.4d) [Computer software]*. Menlo Park, CA: SRI International. Retrieved November 20, 2008, from http://www.videredesign.com/vision/svs.htm.

Maimone, M. W., Johnson, A., Cheng, Y., Willson, R., & Matthies, L. (2006). Autonomous Navigation Results from the Mars Exploration Rover (MER) Mission. In *Experimental Robotics IX*, Springer Tracts in Advanced Robotics (Vol. 21, pp. 3-13). Springer Berlin / Heidelberg. Retrieved April 16, 2009, from http://dx.doi.org/10.1007/11552246_1.

Malik, J., & Perona, P. (1990). Preattentive texture discrimination with early vision mechanisms. *Journal of the Optical Society of America A*, *7*(5), 923-932. doi: 10.1364/JOSAA.7.000923.

Manduchi, R. (1999). Bayesian fusion of color and texture segmentations. In *Proceedings of the Seventh IEEE International Conference on Computer Vision, 1999.* (Vol. 2, pp. 956-962). Kerkyra, Greece. doi: 10.1109/ICCV.1999.790351.

Mathworks. (2005). *Matlab (Version 7.1) with Optimization Toolbox (Version 3.0.3) [Computer software]*. Natick, MA.

Mishkin, A., & Laubach, S. (2006). From Prime to Extended Mission: Evolution of the MER Tactical Uplink Process. In *Proceedings of SpaceOps 2006 Conference* (pp. AIAA-2006-5689). Rome, Italy: American Institute of Aeronautics and Astronautics.

Moore, H. J., Hutton, R. E., Scott, R. F., Spitzer, C. R., & Shorthill, R. W. (1977). Surface materials of the Viking landing sites. *Journal of Geophysical Research*, *82*(28), 4497-4523. doi: 10.1029/JS082i028p04497.

NASA/JPL. (2005, July 12). JPL.NASA.GOV: Pushing Away from Purgatory, Mars Exploration Rover Image Release. *NASA Jet Propulsion Laboratory*. Retrieved March 6, 2009, from http://www.jpl.nasa.gov/missions/mer/images-print.cfm?id=1709.

NASA/JPL. (2007). *MSL Landing Site Selection - User's Guide to Engineering Constraints. Version 4.5*. The Mars Science Laboratory Project. Jet Propulsion Laboratory, California Institute of Technology. Retrieved March 5, 2009, from http://webgis.wr.usgs.gov/msl/docs/MSL_Eng_User_Guide_v4.5.1.pdf.

NASA/JPL. (2008a, October). Mars Exploration Rover Mission: Where Are the Rovers Now? Retrieved November 7, 2008, from http://marsrovers.jpl.nasa.gov/mission/traverse_maps.html.

NASA/JPL. (2008b, December 4). Next NASA Mars Mission Rescheduled for 2011. *NASA Jet Propulsion Laboratory*. Retrieved December 5, 2008, from http://www.jpl.nasa.gov/news/news.cfm?release=2008-226.

Nilsson, N. J. (1982). *Principles of Artificial Intelligence* (p. 476). New York, N.Y.: Springer-Verlag.

Ojeda, L., & Borenstein, J. (2002). FLEXnav: fuzzy logic expert rule-based position estimation for mobile robots on rugged terrain. In *Proceedings of the 2002 IEEE International Conference on Robotics and Automation (ICRA '02)* (Vol. 1, pp. 317-322). Washington, DC. doi: 10.1109/ROBOT.2002.1013380.

Ojeda, L., Cruz, D., Reina, G., & Borenstein, J. (2006). Current-Based Slippage Detection and Odometry Correction for Mobile Robots and Planetary Rovers. *IEEE Transactions on Robotics*, *22*(2), 366-378. doi: 10.1109/TRO.2005.862480.

Olsen, R., Garner, J., & Van Dyke, E. (2002). Terrain classification in urban wetlands with high-spatial-resolution multispectral imagery. In *Proceedings of SPIE Conference on Sensors, Systems, and Next-Generation Satellites VI* (Vol. 4881, pp. 686-691). Agia Pelagia, Crete, Greece: SPIE. doi: 10.1117/12.465161.

Rakhlin, A., Mukherjee, S., & Poggio, T. (2006). Stability Results in Learning Theory. *Analysis and Applications*, *3*(4), 397-419.

Rasmussen, C. (2002). Combining laser range, color, and texture cues for autonomous road following. In *Proceedings of the 2002 IEEE International Conference on Robotics and Automation (ICRA '02)* (Vol. 4, pp. 4320-4325). Washington, DC. doi: 10.1109/ROBOT.2002.1014439.

Reed, T. R., & du Buf, J. M. H. (1993). A review of recent texture segmentation and feature extraction techniques. *CVGIP: Image Understanding*, *57*(3), 359-372. doi: 10.1006/ciun.1993.1024 .

Reina, G., Ojeda, L., Milella, A., & Borenstein, J. (2006). Wheel slippage and sinkage detection for planetary rovers. *IEEE/ASME Transactions on Mechatronics*, *11*(2), 185-195. doi: 10.1109/TMECH.2006.871095.

Rover Team. (1997). Characterization of the Martian Surface Deposits by the Mars Pathfinder Rover, Sojourner. *Science*, *278*(5344), 1765-1768. doi: 10.1126/science.278.5344.1765.

Sadhukhan, D. (2004). *Autonomous Ground Vehicle Terrain Classification Using Internal Sensors*. Thesis (M.S.), Florida State University. Retrieved from http://etd.lib.fsu.edu/theses/available/etd-04092004-171647.

Schölkopf, B. (2000). *Statistical Learning and Kernel Methods*. Technical Report, Microsoft Research. Retrieved November 12, 2008, from ftp://ftp.research.microsoft.com/pub/tr/tr-2000-23.pdf.

Schölkopf, B., Platt, J., Shawe-Taylor, J., Smola, A. J., & Williamson, R. C. (2001). Estimating the Support of a High-Dimensional Distribution. *Neural Computation*, *13*(7), 1443-1471. doi: 10.1162/089976601750264965.

Seraji, H. (1999). Traversability index: a new concept for planetary rovers. In *Proceedings of the 1999 IEEE International Conference on Robotics and Automation (ICRA '99)* (Vol. 3, pp. 2006-2013). Detroit, MI. doi: 10.1109/ROBOT.1999.770402.

Shi, X., & Manduchi, R. (2003). A Study on Bayes Feature Fusion for Image Classification. In *Proceedings of the Conference on Computer Vision and Pattern Recognition Workshop, 2003 (CVPRW '03)* (Vol. 8, p. 95). Madison, WI. doi: 10.1109/CVPRW.2003.10090.

Simpson, A. J., & Fitter, M. J. (1973). What is the best index of detectability? *Psychological Bulletin*, *80*(6), 481-488. doi: 10.1037/h0035203.

Sofman, B., Lin, E., Bagnell, J. A., Cole, J., Vandapel, N., & Stentz, A. (2006). Improving robot navigation through self-supervised online learning. *Journal of Field Robotics*, *23*(11-12), 1059-1075. doi: 10.1002/rob.20169.

Steiner, M. (1978). Analyse Der Triebkraft-Schlupfkurve Von Feifen Berechnung Aus Den Verlustanteilen Und Den Spannungsverteilungen (An Analysis of the Traction Slip Curve of Tires Calculated from the Loss Factors and the Stress Distribution). In *Proceedings of the 6th International Conference of the Society for Terrain Vehicle Systems* (Vol. 2, pp. 555-586). Vienna, Austria: University of Toronto Press.

Stentz, A. (1994). *The D* Algorithm for Real-Time Planning of Optimal Traverses* (p. 34). Technical Report, Pittsburgh, PA: The Robotics Institute, Carnegie Mellon University. Retrieved November 5, 2008, from http://www.ri.cmu.edu/pubs/pub_356.html.

Strang, G. (1993). Wavelet Transforms Versus Fourier Transforms. *Bulletin of the American Mathematical Society*, *28*(2), 288-305. doi: 10.1090/S0273-0979-1993-00390-2.

Talukder, A., Manduchi, R., Castano, R., Owens, K., Matthies, L., Castano, A., et al. (2002). Autonomous terrain characterisation and modelling for dynamic control of unmanned vehicles. In *Proceedings of the 2002 IEEE/RSJ International Conference on Intelligent Robots and System* (Vol. 1, pp. 708-713). Lausanne, Switzerland. doi: 10.1109/IRDS.2002.1041474.

Talukder, A., Manduchi, R., Rankin, A., & Matthies, L. (2002). Fast and reliable obstacle detection and segmentation for cross-country navigation. In *Proceedings of the 2002 IEEE Intelligent Vehicle Symposium* (Vol. 2, pp. 610-618). France.

Vapnik, V. (2000). *The Nature of Statistical Learning Theory*. Statistics for engineering and information science (2nd ed., p. 314). New York: Springer.

Videre Design. (2001). STH-DCAM Stereo Head User's Manual, Rev. 2. Retrieved February 13, 2009, from http://www.videredesign.com/docs/sthdcam.pdf.

Ward, C., & Iagnemma, K. (2007). Classification-Based Wheel Slip Detection and Detector Fusion for Outdoor Mobile Robots. In *Proceedings of the 2007 IEEE International Conference on Robotics and Automation (ICRA '07)* (pp. 2730-2735). Rome, Italy. doi: 10.1109/ROBOT.2007.363878.

Weiss, C., Frohlich, H., & Zell, A. (2006). Vibration-based Terrain Classification Using Support Vector Machines. In *Proceedings of the 2006 IEEE/RSJ International Conference on Intelligent Robots and Systems* (pp. 4429-4434). Beijing, China. doi: 10.1109/IROS.2006.282076.

Welch, P. D. (1967). The use of fast Fourier transform for the estimation of power spectra: A method based on time averaging over short, modified periodograms. *IEEE Transactions on Audio and Electroacoustics*, *15*(2), 70-73.

Weldon, T. P., Higgins, W. E., & Dunn, D. F. (1996). Efficient Gabor filter design for texture segmentation. *Pattern Recognition*, *29*(12), 2005-2015. doi: 10.1016/S0031-3203(96)00047-7 .

Wellington, C., Courville, A., & Stentz, A. (2005). Interacting Markov Random Fields for Simultaneous Terrain Modeling and Obstacle Detection. In *Proceedings of Robotics: Science and Systems* (pp. 1-8). Cambridge, MA: MIT Press.

Wilcox, B. H. (1994). Non-geometric hazard detection for a Mars microrover. In *Proceedings of the Conference on Intelligent Robotics in Field, Factory, Service, and Space (CIRFFSS '94)*, NASA Conference Publication (Vol. 2, p. 675). Houston, TX, USA: Publ by NASA, Washington, DC, USA.

Wong, J. (2001). *Theory of Ground Vehicles* (3rd ed.). New York: John Wiley.

Wong, J., & Reece, A. R. (1967). Prediction of rigid wheel performance based on the analysis of soil-wheel stresses part I. Performance of driven rigid wheels. *Journal of Terramechanics*, *4*(1), 81-98. doi: 10.1016/0022-4898(67)90105-X.

Ye, C., & Borenstein, J. (2004). T-transformation: traversability analysis for navigation on rugged terrain. In *Proceedings of the SPIE Defense and Security Symposium, Unmanned Ground Vehicle Technology VI* (Vol. 5422, pp. 473-483). Orlando, FL: SPIE. doi: 10.1117/12.542576.

Appendix

A

TORTOISE Rover Description

TORTOISE is the four-wheeled rover on which each of the algorithms developed in this thesis was tested. Shown in Figure A-1, this rover was designed and built for the purpose of studying terrain interaction and sensing issues affecting planetary rovers. Since it was first described in (Brooks, 2004), TORTOISE has been upgraded in both sensors and computing power. This appendix presents an updated version of the description originally presented in (Brooks, 2004).

Figure A-1. Photo of TORTOISE, showing location of stereo camera pair

TORTOISE is a four-wheeled rover with an actively reconfigurable suspension. It is 80 cm long in its longest configuration and is 50 cm wide at its widest point. The angles between the two suspension struts on each side can be controlled independently. The two shoulders are connected to the main body via a differential, so that they can rotate independently. The main body pitches at an angle midway between the two sides. The direction of the rover is controlled using skid steering. Rover dimensions are summarized in Table A-1.

TABLE A-1. TORTOISE DIMENSIONS

Length	80 cm[32]
Width	50 cm
Wheel Diameter	20 cm
Wheel Width	5.1 cm
Grouser Height	1.0 cm

The four wheels are made of 2.3-mm-thick round aluminum tubing. Each wheel is 20 cm in diameter and 5.1 cm wide, with 20 stainless steel grousers extending 1.0 cm perpendicular to the surface of the wheel. The wheels are powered by 12-watt DC brush-type motors with 246:1 planetary gearboxes and an additional 2:1 reduction with spiral bevel gears. The shoulder joints are powered by 10.5-watt DC brush-type motors, with 134:1 planetary gearboxes and a 10:1 worm/worm-gear pair. The motion of each of the six motors is sensed using a magnetic encoder. Motor and transmission details are presented in Table A-2.

[32] Length measured with TORTOISE in longest configuration.

TABLE A-2. TORTOISE MOTORS AND TRANSMISSIONS

Wheel Motor	12-watt DC brush-type	Faulhaber 2342S012CR
Wheel Transmission	492:1	Faulhaber 30/1 246:1 2:1 spiral bevel gear pair
Shoulder Motor	10.5-watt DC brush-type	Faulhaber 2824S012C
Shoulder Transmission	2680:1	Faulhaber 38/1 134:1 20:1 worm/worm gear

The front right wheel of the rover is equipped with several sensors to study wheel-terrain interaction. A 5.6 N-m torque sensor measures the torque applied by the motor to the wheel, as shown in Figure A-2. A contact microphone, used to sense vibrations, is mounted to a suspension strut near the front right wheel, as shown in Figure A-3. Additionally, a color CCD camera with a 3.5mm-8.0mm varifocal lens is mounted to the rover body where it can maintain a view of the front right wheel, as shown in Figure A-4. Detailed information and model numbers for these sensors are presented in Table A-3.

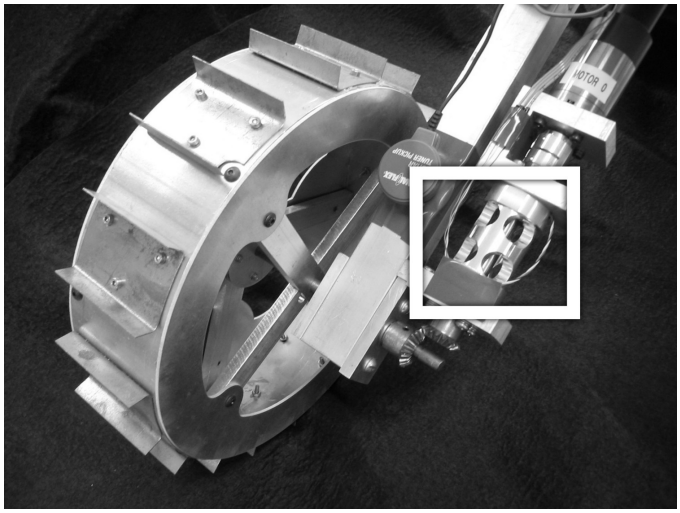

Figure A-2. Torque sensor mounted on TORTOISE

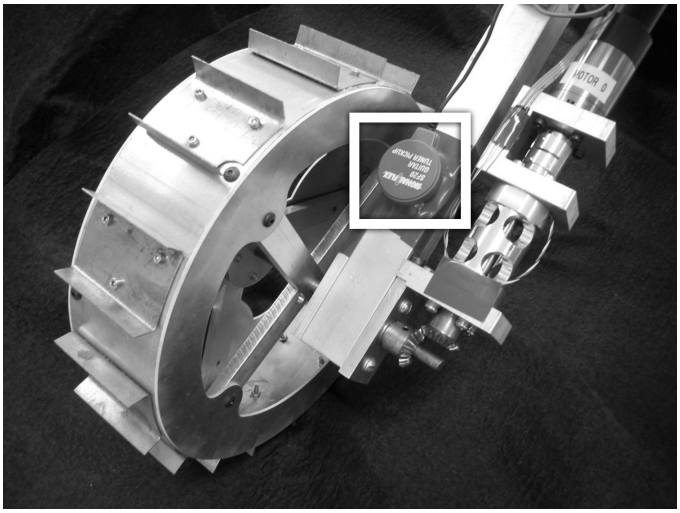

Figure A-3. Vibration sensor mounted on TORTOISE

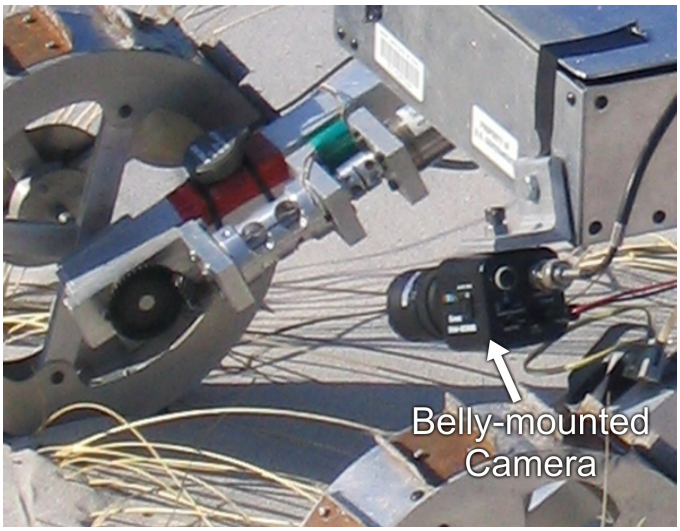

Figure A-4. Belly-mounted camera on TORTOISE

TABLE A-3. TORTOISE SENSORS

Motor Rotation	Magnetic encoders	Faulhaber HEM2342S16
Torque	5.6 N-m Torque sensor	Futek T5160
Vibration	Contact microphone	Signal Flex SF-20
Belly-Mounted Vision	1/3” CCD camera 3.5mm-8.0mm lens	Genwac GW-202B Edmund Optics NT55-255
Stereo Vision	19-cm baseline color stereo camera pair	Videre Design Dual DCAM
Configuration	2-axis Tilt sensor Potentiometers	Crossbow CXTA02 Vishay/Spectrol 65700103

To sense terrain from a distance, TORTOISE is equipped with a stereo camera pair mounted on a mast 90 cm above the terrain. The stereo camera pair is a 19-cm-

baseline Videre Design "dual DCAM" capable of capturing color images at 640×480 resolution. Range data were extracted from the stereo images using SVS (Small Vision System), Videre Design's commercial stereo processing software. The accuracy of the range estimation is sufficient to assign pixels to 20-cm by 20-cm terrain cells up to a distance of 8 meters.

The rover is also outfitted with sensors to estimate its attitude and suspension configuration. A two-axis tilt sensor measures the pitch and roll of the rover body. The angles of the two shoulder joints are measured with potentiometers, as is the angle between the right shoulder and the body. Model numbers for all sensors are shown in Table A-3.

All feedback control and data sampling is done on computers attached to the rover via a tether. Motor power is sent to the rover via this tether and sensory signals are returned the same way. Motor control is implemented on an off-board PC104 computer. Sampling of wheel torque and rover configuration is done by the same PC104 system, and images from the stereo camera pair are captured via a FireWire (IEEE 1394) connection to the PC104 system. Image capture from the belly-mounted camera and vibration signal recording is done on a tethered laptop computer. Figure A-5 shows a schematic of the rover communications.

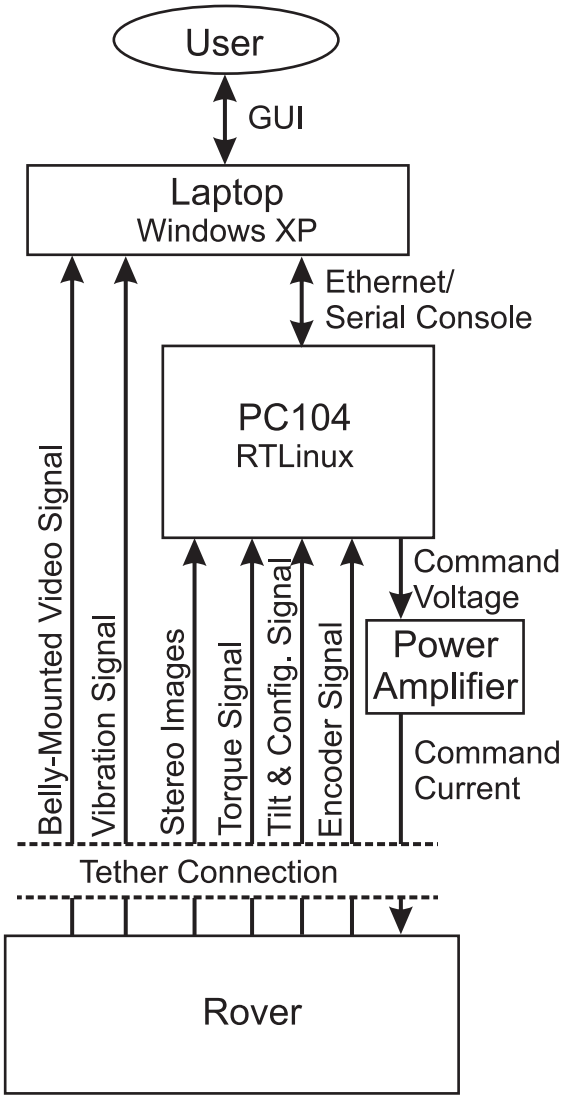

Figure A-5. Rover communications schematic

The PC104 system uses a VersaLogic Jaguar system board, with a Pentium III 850 MHz processor and 256 MB of RAM. Analog signals, including signals from the tilt sensor, torque sensor, and potentiometers, are sensed using an analog input card. Encoder signals are received by a quadrature decoder card. Control signals for the motors are sent as voltage outputs from an analog output card, which are translated into current signals using a custom power amplifier board, based on the National Semiconductor LMD18245

full-bridge motor driver. The current signals are sent to the motor via the tether. Stereo camera images are received on a FireWire (IEEE 1394) card. The PC104 is also equipped with a sound card to receive vibration signals and a frame grabber to receive imagery from the belly-mounted camera, but use of these cards was never implemented. Model numbers for the components of the PC104 system are presented in Table A-4.

TABLE A-4. TORTOISE PC104 SYSTEM COMPONENTS

CPU Board (PC104+)	VersaLogic Jaguar (Pentium III 850 MHz)
RAM	Crucial 256MB PC133 SDRAM
Hard Drive	6 GB 2.5" Internal Hard Drive
Analog Input, Digital I/O	Diamond Systems Diamond MM-AT
Quadrature Decoder	Microcomputer Systems MSI-P400
Analog Output	Diamond Systems Ruby MM-4XT
FireWire	Advanced Digital Logic MSMW104+
Sound Card	Diamond Systems Crystal-MM-HP-5
Video Frame Grabber (NTSC)	Parvus FG104

The PC104 system runs Linux with an RTLinux microkernel for real-time control and data sampling. The control and sampling software was developed specifically for this rover. Stereo image capture was implemented using the libraries provided with the SVS software. User interaction with the PC104 system is done over a connection to the laptop computer, either using a 100BASE-TX Ethernet connection using SSH (preferentially) or using a serial console connection.

The laptop computer, a PC running Windows XP, interacts with the PC104 system, the belly-mounted camera, and the vibration sensor. It connects to the PC104 system using either an Ethernet crossover cable or a null modem serial cable. It connects to the belly-mounted camera with a USB video capture box (ProVideo model PV321CE). The connection to the vibration sensor is via a standard audio cable which plugs into the laptop's microphone port.

The entire system is run using battery power so that it can be taken to remote locations where electrical outlets are unavailable. Power to the PC104 is provided by a 12V motorcycle battery, regulated to 5V and 3.3V with a DC/DC converter. Power to the motors is provided by two 12V motorcycle batteries and passed on to the motors by the power amplifier board. Power for the laptop is provided by onboard batteries.

Appendix

B

Wingaersheek Beach Description

Each of the algorithms developed in this thesis was applied to experiment data collected at Wingaersheek Beach, in Gloucester, MA. Overview pictures of the beach are shown in Figure B-1, Figure B-2, Figure B-3, and Figure B-4. This is a public beach located on Cape Anne just north of Gloucester, at the northern end of Atlantic Street. It is located roughly at 42.651 degrees North, and 70.686 degrees West.

Figure B-1. TORTOISE on Wingaersheek Beach, looking northeast towards Annisquam lighthouse. Mats of beach grass lie between TORTOISE and the rock outcrops.

Figure B-2. TORTOISE on Wingaersheek Beach, looking southeast towards Goose Cove. A long stretch of sand with occasional mats of beach grass lies between the rover and the distant rock outcrop.

Figure B-3. TORTOISE (distant) on Wingaersheek Beach, looking northwest. A band of small, loose stones divides sections of washboard-textured sand between the camera and TORTOISE.

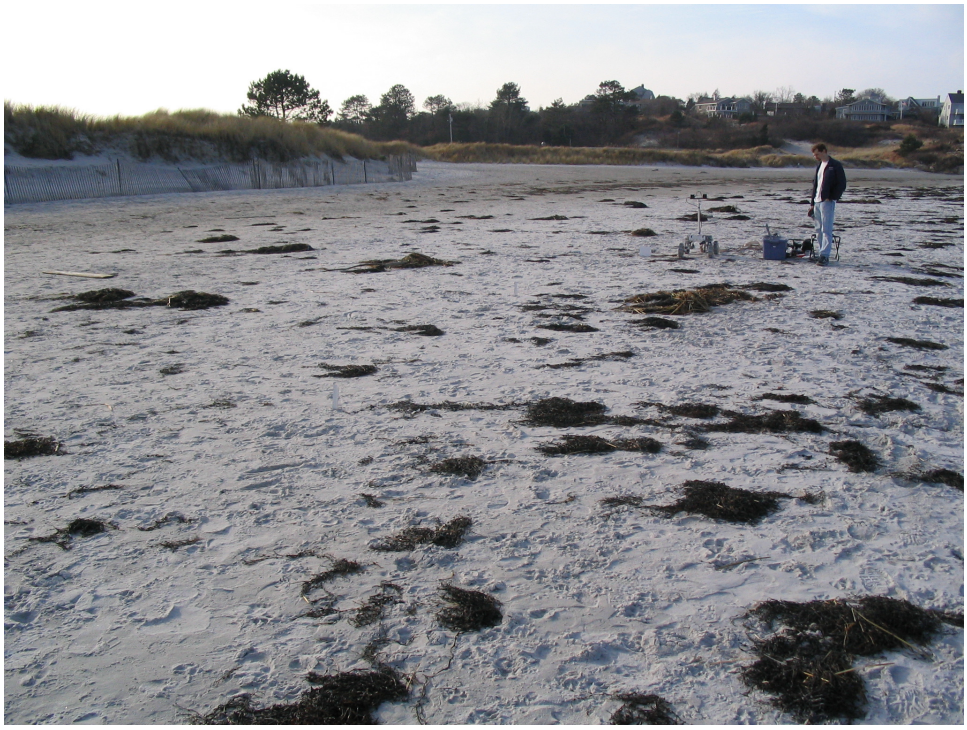

Figure B-4. Chris Ward and TORTOISE on Wingaersheek Beach, looking southwest. Large mats of dark beach grass lie over the sand between the camera and TORTOISE.

Wingaersheek Beach is a sandy beach with a mix of small and large rock outcrops relative to the size of the rover, and was chosen as a test site due to its similarity in appearance to the MER landing sites on Mars. For the experiments described in this thesis, the beach was considered to be composed of three distinct terrain classes: sand, rock, and beach grass. Figure B-5 shows a sample scene from the beach. As seen by the rover, sand appears as a uniform gray flat surface, rock appears tan and orange with some steep slopes and fine uniform texture, and beach grass appears highly textured with mixed browns and shadows.

Figure B-5. TORTOISE on Wingaersheek Beach, showing terrain classes

B.1 Sample Stereo Camera Images

Six experimental data sets were used to assess the performance of the visual classifier in 1.1, the novel terrain detector in 1.1, and the self-supervised classification framework in 1.1. Sample images from the left camera of the TORTOISE's mast-mounted stereo camera pair are shown in Figure B-6 through Figure B-11.

Figure B-6. Sample image from Image Set 1 (Nov 30, 2006, Run 2)

Figure B-7. Sample image from Image Set 2 (Dec 7, 2006, Run 4)

Figure B-8. Sample image from Image Set 3 (Dec 7, 2006, Run 5)

Figure B-9. Sample image from Image Set 4 (Dec 7, 2006, Run 6)

Figure B-10. Sample image from Image Set 5 (Dec 14, 2006, Run 1)

Figure B-11. Sample image from Image Set 6 (Dec 14, 2006, Run 2)

The terrain learning system for novel environments in 1.1 was applied to an additional data set. A sample image from that data set is shown in Figure B-12.

Figure B-12. Sample image from terrain learning system for novel environments image set (Oct 30, 2007, Run 5)

Appendix

C

Wheel-Terrain Interaction Testbed Description

The FSRL wheel-terrain interaction testbed, shown in Figure C-1, is an experimental platform in the Field and Space Robotics Laboratory. It was designed by Sharon Lin for the purpose of studying the behavior of a rigid wheel driving in deformable terrain and has been used in the past to characterize terrain properties (Kang, 2003). This appendix is largely drawn from (Brooks, 2004) and is included here for reference.

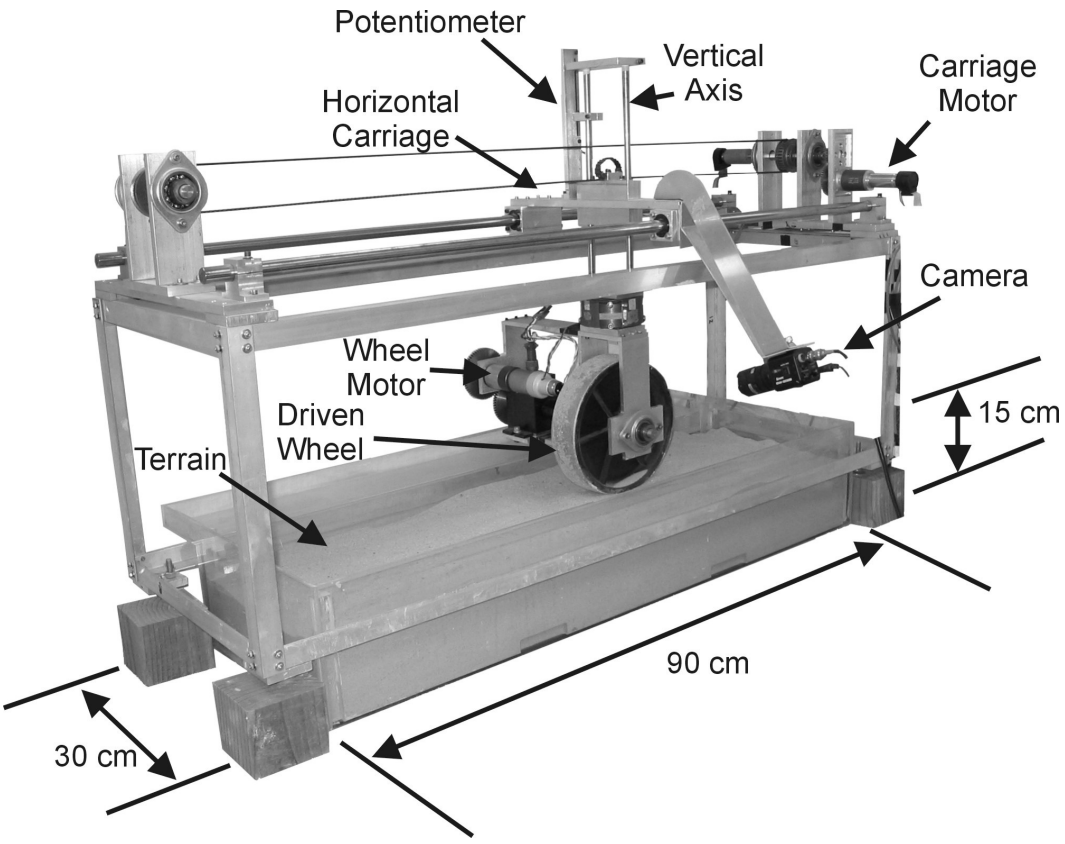

Figure C-1. Wheel-terrain interaction testbed, with dimensions

The testbed consists of a driven wheel mounted on an undriven vertical axis. The wheel-axis assembly is mounted on a frame such that the wheel's forward velocity and angular velocity can be controlled independently. The testbed can be fitted with a number of different wheel assemblies, each assembly containing both a motor and a wheel. For the results presented in this thesis, tests were conducted using the black plastic wheel assembly.

The black plastic wheel assembly, shown in Figure C-2, consists of a wheel, a motor, and a torque sensor. The wheel is 4.8 cm wide and 20 cm in diameter. Sand is bonded to the outside of the wheel to improve traction. The motor applying torque to the wheel is a 14.5-watt DC brush-type motor. It is mounted with a 246:1 transmission, and has a tachometer to measure angular velocity. The maximum linear velocity of the outside of the wheel is 15 cm/sec. Motor torque is measured using a rotating torque sensor with a working range of 7 N-m, mounted between the motor and the wheel. A six-axis force-torque sensor is mounted between this wheel assembly and the frame, so that all of the forces and torques applied by the wheel on the terrain can be sensed. Table C-1 provides detailed information about this wheel assembly including component model numbers.

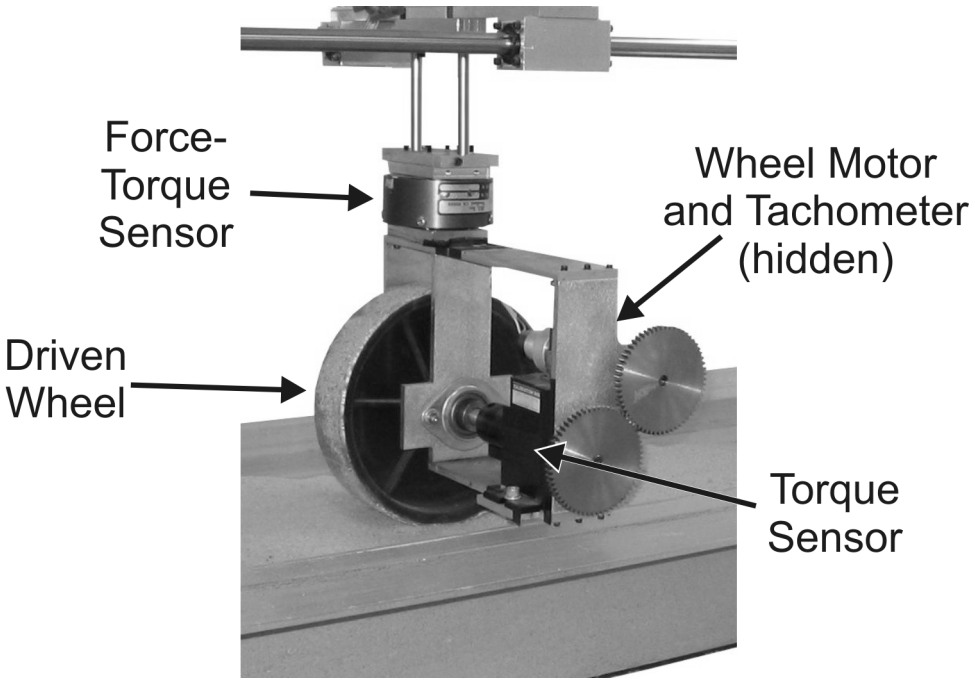

Figure C-2. Black wheel assembly on wheel-terrain interaction testbed

TABLE C-1. SPECIFICATIONS FOR BLACK PLASTIC WHEEL ASSEMBLY

Wheel Diameter	20 cm	
Wheel Width	4.8 cm	
Motor	14.5-watt DC brush-type	Faulhaber 3557K006C
Transmission	246:1	Faulhaber 38/2
Sensors	Tachometer Torque Sensor Force-Torque Sensor	 Cooper LXT 982 JR3 UFS-3515A100

This wheel assembly is mounted to the carriage, which allows it to move freely in the vertical direction while constraining its forward and lateral movement. The vertical position of the wheel is measured using a linear potentiometer mounted on the carriage. The horizontal position of the carriage is controlled with an 8.5-watt brush-type DC motor, with an overall 1936:5 transmission ratio mounted to a 5-cm-diameter pulley. The pulley position is sensed with a 2048-PPR encoder. The maximum carriage forward velocity is 5 cm/sec. This information is summarized in Table C-2.

TABLE C-2. WHEEL-TERRAIN INTERACTION TESTBED CARRIAGE DRIVE SPECIFICATIONS

Motor	8.5-watt DC brush-type	Escap 23DT
Transmission	1936:5 overall	
Pulley Diameter	5 cm	
Pulley Position Sensor	Encoder	2048 PPR

The wheel rests in a bin of terrain 90 cm long by 30 cm wide by 15 cm deep. A large number of terrains have been used in experiments, including washed beach sand, dry bentonite, JSC Mars-1 soil stimulant, gravel, moist clay, and topsoil.

Signals from the testbed are sent to an AMD K6-2 500 MHz desktop computer running Windows XP. All signals from the tachometer, torque sensor, and force-torque sensor are sent to an 8-axis 12-bit I/O board (ServoToGo STGII-8). Control signals from the computer to the testbed are output as voltage signals using the same 8-axis I/O board. These voltage signals are inputs to a custom power amplifier card. The power amplifier card sends a high-power voltage signal (15V, 3A max) to the wheel motor, and a high-power PWM signal (25V, 3A max) to the carriage motor. The data sampling and control software was written specifically for this testbed.

Appendix

D

Support Vector Machine Background and Optimizations

The support vector machine (SVM) classifiers presented in this thesis were implemented using the open-source library LIBSVM (Chang & C. Lin, 2005, 2008). This appendix is intended to define the mathematical formulations used in this library. C-support vector classification is the more traditional formulation of an SVM, and is presented in D.1. This is the formulation used for vibration-based terrain classification in 2.1 and visual classification in 1.1. The one-class SVM, presented in D.2, is an extension to the SVM framework which can distinguish "similar" features from "different." It is used as one of the baseline approaches to novelty detection in 1.1. Both of these classifiers use kernel functions for regularization, and the formulations of these kernel functions are presented in D.3. Finally, as mentioned in the main body of this thesis, there are some optimizations which can improve the speed of classification. These optimizations are presented in D.4.

D.1 C-Support Vector Classification

The C-support vector classifier is used for most of the two-class classification presented in this thesis. Here, it is assumed that labeled training data is available in the form of vectors $\mathbf{x}_i \in \Re^n, i = 1,\ldots,l$ and labels $y_i \in \{1,-1\}$. Note that *n* is the dimension of

the feature space, and l is the number of training examples. Given this training data, the SVM software solves the following problem:

$$\begin{aligned} \min_{\mathbf{w},b,\xi} \quad & \frac{1}{2}\mathbf{w}^T\mathbf{w} + C\sum_{i=1}^{l}\xi_i \\ \text{subject to} \quad & y_i\left(\mathbf{w}^T\boldsymbol{\varphi}(\mathbf{x}_i)+b\right) \geq 1-\xi_i \\ & \xi_i \geq 0,\ i=1,\ldots,l, \end{aligned} \tag{D-1}$$

where $\boldsymbol{\varphi}$ is a mapping implicitly defined by the kernel function. The reason a support vector machine classifier can be trained quickly is that (D-1) can be written in a dual form. Here the dual form is

$$\begin{aligned} \min_{\boldsymbol{\alpha}} \quad & \frac{1}{2}\boldsymbol{\alpha}^T\mathbf{Q}\boldsymbol{\alpha} - \mathbf{e}^T\boldsymbol{\alpha} \\ \text{subject to} \quad & \mathbf{y}^T\boldsymbol{\alpha} = 0, \\ & 0 \leq \alpha_i \leq C, \quad i=1,\ldots,l, \end{aligned} \tag{D-2}$$

where $\mathbf{e}$ is a vector of length l composed of all ones, C is the factor regulating the complexity of the classification boundary, $\mathbf{Q}$ is an l-by-l matrix with elements $Q_{i,j} \equiv y_i y_j K(x_i, x_j)$, and $K(x_i, x_j) \equiv \boldsymbol{\varphi}(x_i)\boldsymbol{\varphi}(x_j)$ is the kernel. Using various techniques, the support vector machine software finds the vector $\boldsymbol{\alpha}$ and scalar b.

After the training process is finished, a new vector $\mathbf{x}$ is classified using the decision function

$$y_{pred} = \operatorname{sgn}\left(\sum_{i=1}^{l} y_i \alpha_i K(\mathbf{x}_i, \mathbf{x}) + b\right). \tag{D-3}$$

D.2 One-Class Support Vector Machine

The one-class SVM is one approach for using a support vector machine to identify whether a new vector is similar to or different from a set of training data. Here,

training vectors $\mathbf{x}_i \in \Re^n, i = 1,\ldots,l$ are provided without labels, and the problem solved by the SVM is

$$\begin{aligned} \min_{\mathbf{w},\xi,\rho} \quad & \frac{1}{2}\mathbf{w}^T\mathbf{w} - \rho + \frac{1}{\nu l}\sum_{i=1}^{l}\xi_i \\ \text{subject to} \quad & \mathbf{w}^T\boldsymbol{\varphi}(\mathbf{x}_i) \geq \rho - \xi_i \\ & \xi_i \geq 0,\ i = 1,\ldots,l, \end{aligned} \tag{D-4}$$

where $\nu \in (0,1]$ is the factor regulating the complexity of the classifier, and $\boldsymbol{\varphi}$ is a mapping implicitly defined by the kernel function. For this problem, the dual formulation solved by LIBSVM is

$$\begin{aligned} \min_{\boldsymbol{\alpha}} \quad & \frac{1}{2}\boldsymbol{\alpha}^T\mathbf{Q}\boldsymbol{\alpha} \\ \text{subject to} \quad & 0 \leq \alpha_i \leq C, \quad i = 1,\ldots,l, \\ & \mathbf{e}^T\boldsymbol{\alpha} = \nu l, \end{aligned} \tag{D-5}$$

where $\mathbf{e}$ is a vector of length l composed of all ones, $\mathbf{Q}$ is an l-by-l matrix with elements $Q_{i,j} \equiv y_i y_j K(x_i, x_j)$, and $K(x_i, x_j) \equiv \boldsymbol{\varphi}(x_i)\boldsymbol{\varphi}(x_j)$ is the kernel. LIBSVM thus solves for the vector $\boldsymbol{\alpha}$ and the scalar ρ.

After training, a new vector $\mathbf{x}$ is considered to be similar to the training data if $y_{pred} > 0$ in the decision function

$$y_{pred} = \operatorname{sgn}\left(\sum_{i=1}^{l}\alpha_i K(\mathbf{x}_i, \mathbf{x}) - \rho\right). \tag{D-6}$$

D.3 Kernel Functions

One of the main choices to be made when using a SVM is which kernel function to use. LIBSVM provides the option to choose between four different kernels: linear, polynomial, radial basis function (RBF) and sigmoid. The formulations for these kernels are presented in Table D-1. In this table, γ, r, and d are kernel parameters.

TABLE D-1. KERNEL TYPES AND CORRESPONDING EQUATIONS

Kernel Type	Equation	
Linear	$K(\mathbf{x}_i, \mathbf{x}_j) = \mathbf{x}_i{}^T \mathbf{x}_j$	(D-7)
Polynomial	$K(\mathbf{x}_i, \mathbf{x}_j) = (\gamma \mathbf{x}_i{}^T \mathbf{x}_j + r)^d, \gamma > 0$	(D-8)
Radial Basis Function (RBF)	$K(\mathbf{x}_i, \mathbf{x}_j) = \exp(-\gamma \lVert \mathbf{x}_i - \mathbf{x}_j \rVert^2), \gamma > 0$	(D-9)
Sigmoid	$K(\mathbf{x}_i, \mathbf{x}_j) = \tanh(\gamma \mathbf{x}_i{}^T \mathbf{x}_j + r)$	(D-10)

D.4 Optimizations for Linear and Polynomial Kernels

In situations where there are many training points (i.e. l is large), calculation of the summation in the decision function—either $\sum y_i \alpha_i K(\mathbf{x}_i, \mathbf{x})$ in Equation (D-3) or $\sum \alpha_i K(\mathbf{x}_i, \mathbf{x})$ in Equation (D-6)—can take a long time. This is mitigated by the fact that $\boldsymbol{\alpha}$ is typically sparse, but $\boldsymbol{\alpha}$ still contains $O(l)$ nonzero elements. Thus, evaluating the decision function requires evaluating $O(ln)$ multiplications, where n is the number of elements in $\mathbf{x}$. When using a linear or polynomial kernel, the cost of evaluating the decision function may be reduced by changing the order of summation and precomputing some intermediate terms.

When using a linear kernel, the approach to changing the order of multiplications is straightforward:

$$\sum_{i=1}^{l} y_i \alpha_i K(\mathbf{x}_i, \mathbf{x}) = \sum_{i=1}^{l} y_i \alpha_i (\mathbf{x}_i{}^T \mathbf{x}). \tag{D-11}$$

The multiplication is then regrouped:

$$\sum_{i=1}^{l} y_i \alpha_i K(\mathbf{x}_i, \mathbf{x}) = \left(\sum_{i=1}^{l} y_i \alpha_i \mathbf{x}_i{}^T \right) \mathbf{x}. \tag{D-12}$$

This yields

$$\sum_{i=1}^{l} y_i \alpha_i K(\mathbf{x}_i, \mathbf{x}) = \mathbf{w}^T \mathbf{x} \tag{D-13}$$

with

$$\mathbf{w} = \sum_{i=1}^{l} y_i \alpha_i \mathbf{x}_i \,. \tag{D-14}$$

Here, **w** can be evaluated only once for each set of training data. Thus, using Equation (D-13), the decision function (D-3) can be evaluated using only $O(n)$ multiplications. This is a savings of $O(l)$ in classification time.

A similar approach can be used to reduce the classification time when a polynomial kernel is used. For the sake of simplicity, the approach is presented assuming **x** has 3 elements (i.e. the feature space has 3 dimensions), but the extension to higher dimensions should be clear. First the polynomial kernel is substituted for K:

$$\sum_{i=1}^{l} y_i \alpha_i K(\mathbf{x}_i, \mathbf{x}) = \sum_{i=1}^{l} y_i \alpha_i \left(\gamma \mathbf{x}_i{}^T \mathbf{x} + r\right)^d \,. \tag{D-15}$$

Then the terms of the polynomial are written as a summation:

$$\sum_{i=1}^{l} y_i \alpha_i K(\mathbf{x}_i, \mathbf{x}) = \sum_{i=1}^{l} \left(y_i \alpha_i \sum_{a_0, a_1, a_2, a_3} d! \frac{r^{a_0}}{a_0!} \frac{\left(\gamma x_{i,1} x_1\right)^{a_1}}{a_1!} \frac{\left(\gamma x_{i,2} x_2\right)^{a_2}}{a_2!} \frac{\left(\gamma x_{i,3} x_3\right)^{a_3}}{a_3!} \right) \cdot \tag{D-16}$$

$$\text{where } a_j \in \aleph_0, \; j = 0, \ldots, n$$

$$\text{and } a_0 + a_1 + a_2 + a_3 = d$$

This second summation with indices a_0, a_1, a_2, and a_3 has $(n+d)!/(n!d!)$ terms. Note that the x with two subscripts indicates an element of the training data, while the x with a single subscript is an element of the vector being classified. The order of summation can be changed:

$$\sum_{i=1}^{l} y_i \alpha_i K(\mathbf{x}_i, \mathbf{x}) = \sum_{a_0, a_1, a_2, a_3} x_1^{a_1} x_2^{a_2} x_3^{a_3} \left(\sum_{i=1}^{l} y_i \alpha_i d! \frac{r^{a_0}}{a_0!} \frac{\left(\gamma x_{i,1}\right)^{a_1}}{a_1!} \frac{\left(\gamma x_{i,2}\right)^{a_2}}{a_2!} \frac{\left(\gamma x_{i,3}\right)^{a_3}}{a_3!} \right) \cdot \tag{D-17}$$

$$\text{where } a_j \in \aleph_0, \; j = 0, \ldots, n$$

$$\text{and } a_0 + a_1 + a_2 + a_3 = d$$

Note that the inner summation does not depend on any features of the vector being evaluated, so it can be computed once for each set of training data:

$$w_{a_0,a_1,a_2,a_3} = \sum_{\substack{i=1 \\ \text{for all } a_0+a_1+a_2+a_3=d}}^{l} y_i \alpha_i d! \frac{r^{a_0}}{a_0!} \frac{(\gamma x_{i,1})^{a_1}}{a_1!} \frac{(\gamma x_{i,2})^{a_2}}{a_2!} \frac{(\gamma x_{i,3})^{a_3}}{a_3!} . \quad \text{(D-18)}$$

Using these coefficients, Equation (D-17) becomes simply

$$\sum_{i=1}^{l} y_i \alpha_i K(\mathbf{x}_i, \mathbf{x}) = \sum_{\substack{a_0,a_1,a_2,a_3 \\ \text{where } a_j \in \aleph_0,\ j=0,\ldots,n \cdot \\ \text{and } a_0+a_1+a_2+a_3=d}} w_{a_0,a_1,a_2,a_3} x_1^{a_1} x_2^{a_2} x_3^{a_3} \quad \text{(D-19)}$$

Thus, using Equation (D-19), the decision function (D-3) can be evaluated with $O((n+d)!/(n!d!))$ multiplications. This approach can be a significant improvement over the $O(ln)$ cost of the standard equation when both n and d are small. For example, with n=5 dimensions, polynomial degree d=3, and l=1000 training examples, $(n+d)!/(n!d!)$=56 while ln=3000. This would result in classification time being reduced by a factor of approximately 50.

Appendix

E

MATLAB Feature Extraction Code

The algorithms developed in this thesis were implemented as Matlab scripts (Mathworks, 2005). This appendix presents short Matlab functions which can be used to extract classification features from raw sensor data.

E.1 Vibration Feature Extraction

Table E-1 presents Matlab code for the feature extraction used in the vibration-based terrain classifier in 2.1. This function takes as an input the time series of accelerometer values, and returns the log-scaled power spectral density features as its output.

TABLE E-1. VIBRATION FEATURE EXTRACTION CODE

```
function VibFeatures = CalculateVibFeatures(VibTimeSeries)
% Calculate Vibration Features

% Input:
%   VibTimeSeries: Row vector of accelerometer values captured in
%     1 second (44100 samples)
% Output:
%   VibFeatures: Vibration features in row vector

NFFT = 2048; % Use 2048 samples for each FFT in Welch's method
VibPSD = pwelch(VibTimeSeries,[],[],NFFT); % Use Welch's method to
   % calculate PSD

VibLogPSD = log(abs(VibPSD)); % Calculate log-scaled magnitudes

MinFreq = 0; % Minimum frequency of interest (Hz)
MaxFreq = 12000; % Maximum frequency of interest (Hz)
SampFreq = 1/length(VibTimeSeries); % Sampling Frequency (Hz)

MinFreqIdx = ceil(NFFT*MinFreq/SampFreq)+1; % Index of minimum freq
MaxFreqIdx = floor(NFFT*MaxFreq/SampFreq)+1; % Index of maximum freq

VibFeatures = VibLogPSD(MinFreqIdx:MaxFreqIdx); % Return features
   % corresponding to frequencies of interest

return
```

E.2 Terrain Geometry Feature Extraction

Table E-2 presents Matlab code for the geometry feature extraction used in the visual terrain classifier in 1.1, the novel terrain detector in 1.1, and the self-supervised classifiers in Chapter 5. This function takes as an input the 3-D coordinates of all of the points associated with a terrain patch, and returns the 4-element geometry feature vector for that terrain patch.

TABLE E-2. TERRAIN GEOMETRY FEATURE EXTRACTION CODE

```
function GeomFeatures = CalculateGeomFeatures(PointsInPatch)
% Calculate Terrain Geometry Features
% Input:
%   PointsInPatch: n x 3 matrix containing positions of points on the
%     surface of a terrain patch. Each row represents a distinct point.
%     Column 1 is the position in the forward direction. Column 2 is
%     the position in the right direction. Column 3 is the vertical
%     position. The origin is the starting position of the rover.
% Output:
%   GeomFeatures: Geometry features in 1x4 row vector
```

```
UpVector = [0,0,1]'; % Specify vertical direction

% Calculate the covariance matrix of the points
CovMat = cov(PointsInPatch);

% Select behavior based on rank of covariance matrix
if (rank(CovMat) > 2)  % If points do not lie on a plane
    % Find the vector with the lowest eigenvalue (i.e. normal to least-
    % squares plane fit to points)
    [U,S,V] = svds(CovMat,1,0); % Singular value decomposition,
       % returning U as 3x1 eigenvector with eigenvalue closest to zero
       % and S is the 1x1 eigenvalue closest to zero

elseif (rank(CovMat) == 2) % If points lie on a plane
    % Find the vector normal to the plane
    U = null(CovMat); % Normal vector (3x1) is the null space of matrix
    S = 0; % Zero variance in normal direction

else % Points lie on a line
    % Find the vector perpendicular to the line closest to the vertical
    A = null(CovMat); % Two normal vectors (3x2) form null space of
       % matrix
    U = A * A' * UpVector; % Project vertical axis into null space
    S = 0; % Zero variance in normal direction
end

U = U ./ sqrt(U' * U); % Normalize U

% First feature: Slope
Slope = acos(abs(U' * UpVector));

% Second feature: Smallest Singular Value (i.e. plane fit error)
SmSingVal = S;

% Third feature: variance in vertical direction
VertVar = UpVector' * CovMat * UpVector;

% Fourth feature: range of heights of points
HeightRange=max(UpVector'*PointsInPatch)-min(UpVector'*PointsInPatch);

GeomFeatures = [Slope, SmSingVal, VertVar, HeightRange];

return
```